Damage Tolerance of Metallic Structures

Analysis Methods and Applications

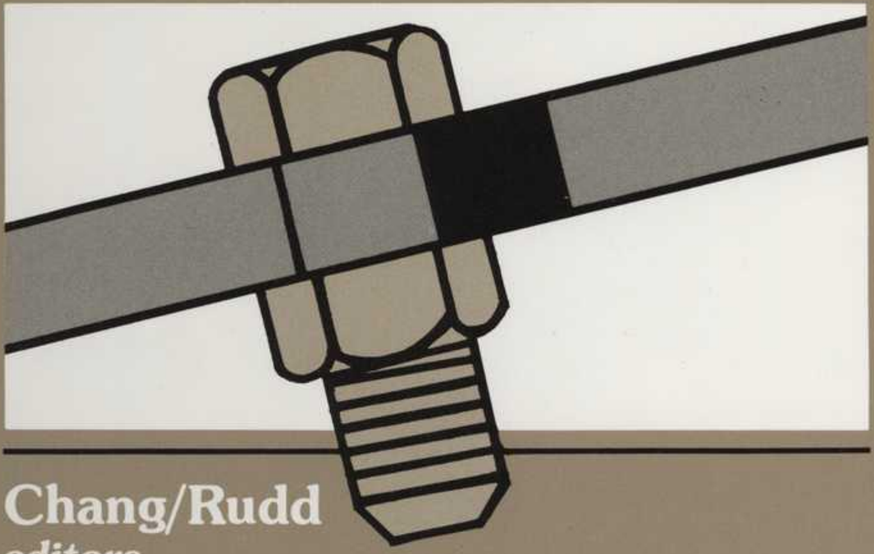

Chang/Rudd
editors

ASTM STP 842

DAMAGE TOLERANCE OF METALLIC STRUCTURES: ANALYSIS METHODS AND APPLICATIONS

A symposium sponsored by
ASTM Committee E-24 on
Fracture Testing
Los Angeles, CA, 29 June 1981

ASTM SPECIAL TECHNICAL PUBLICATION 842
James B. Chang, The Aerospace Corp., and
James L. Rudd, Air Force Wright
Aeronautical Laboratories, editors

ASTM Publication Code Number (PCN)
04-842000-30

1916 Race Street, Philadelphia, PA 19103

Library of Congress Catalog Card Number: 83-73440

NOTE

The Society is not responsible, as a body,
for the statements and opinions
advanced in this publication.

Printed in Ann Arbor, MI
July 1984

Foreword

The symposium on Damage Tolerance Analysis was presented at Los Angeles, CA, 29 June 1981. The symposium was sponsored by ASTM Committee E-24 on Fracture Testing. James B. Chang, The Aerospace Corp., presided as chairman of the symposium and is coeditor of the publication; James L. Rudd, Wright Aeronautical Laboratories is coeditor of the publication.

Related ASTM Publications

Fatigue Mechanics: Advances in Quantitative Measurement of Physical Damage, STP 811 (1983), 04-811000-30

Probabilistic Fatigue Mechanics and Fatigue Methods: Applications for Structural Design and Maintenance, STP 798 (1983), 04-798000-30

Design of Fatigue and Fracture Resistant Structures, STP 761 (1982), 04-761000-30

Methods and Models for Predicting Fatigue Crack Growth Under Random Loading, STP 748 (1981), 04-748000-30

Effect of Load Variables on Fatigue Crack Initiation and Propagation, STP 714 (1980), 04-714000-30

Fatigue of Composite Materials, STP 569 (1975), 04-568000-33

A Note of Appreciation to Reviewers

The quality of the papers that appear in this publication reflects not only the obvious efforts of the authors but also the unheralded, though essential, work of the reviewers. On behalf of ASTM we acknowledge with appreciation their dedication to high professional standards and their sacrifice of time and effort.

ASTM Committee on Publications

ASTM Editorial Staff

Contents

Introduction

In the late 1960s and early 1970s, a number of aircraft structural failures occurred both during testing and in-service. Some of these failures were attributed to flaws, defects, or discrepancies that were either inherent or introduced during the manufacturing and assembly of the structure. The presence of these flaws was not accounted for in design. The design was based on a "safe-life" fatigue analysis. Mean life predictions were made that were based upon materials' unflawed fatigue test data and a conventional fatigue analysis. A scatter factor of four was used to account for initial quality, environment, variation in material properties, and so forth. However, this conventional fatigue (safe-life) analysis approach did not adequately account for the presence and the growth of these flaws.

In order to ensure the safety of the aircraft structure, the U.S. Air Force adopted the damage tolerance design approach to replace the conventional fatigue design approach starting from the mid 1970s. In recent years, a number of different industries have also adopted the damage tolerance approach, only calling it fracture control. The ability of a structure to maintain adequate residual strength in a damaged condition is called damage tolerance. The damage tolerance (or fracture control) approach assumes that flaws are initially present in the structure. The structure must be designed such that these flaws do not grow to a critical size and cause catastrophic failure of the structure within a specified period of time. In order to accomplish this, an accurate damage tolerance analysis must exist.

A Forum on Damage Tolerance Analysis sponsored by ASTM Task Group E24.06.01 on Application of Fracture Data to Life Predictions was held at the University of California, Los Angeles, CA, on 29 June 1981. The purpose of this Forum was to present the state-of-the-art capability for performing damage tolerance analysis. Damage tolerance design requirements, analysis procedures, and applications were presented. The results of the Forum are presented in this volume.

Many people contributed their time and energy to make the Forum on Damage Tolerance Analysis a success. Special thanks are due to (1) the speakers, for their time spent in preparing their presentations and manuscripts; (2) the session Chairmen, Alan Liu and Gerry Vroman, for their efforts and time; (3) the Chairman

of ASTM Subcommittee E24.06 on Fracture Mechanics Applications, Mike Hudson, for his guidance and support; (4) the reviewers, for their constructive comments; and (5) the ASTM staff, for their support in arranging the meeting and careful editing of the manuscript.

James B. Chang
The Aerospace Corporation,
Los Angeles, CA 90009,
coeditor

James L. Rudd
Air Force Wright Aeronautical Laboratories,
Wright-Patterson Air Force Base, OH 45433,
coeditor

Alten F. Grandt, Jr.[1]

Introduction to Damage Tolerance Analysis Methodology

REFERENCE: Grandt, A. F., Jr., "**Introduction to Damage Tolerance Analysis Methodology,**" *Damage Tolerance of Metallic Structures: Analysis Methods and Applications, ASTM STP 842*, J. B. Chang and J. L. Rudd, Eds., American Society for Testing and Materials, 1984, pp. 3–24.

ABSTRACT: The objective of this paper is to introduce analysis methods for evaluating the impact of preexistent cracks on structural performance. Linear elastic fracture-mechanics concepts are briefly described and used to compute the critical crack size for a given component and loading (specify fracture conditions) and to determine the time required for a smaller, subcritical crack to grow to critical size by fatigue or stress corrosion cracking or both. Limitations of linear elastic fracture mechanics are discussed in order to define problems that can be confidently analyzed by the method and to identify areas that require more sophisticated approaches. A particular goal is to establish the background for more specialized topics considered by other papers in the present volume.

KEY WORDS: cracks, fatigue (materials), stress corrosion, fracture (materials), fracture mechanics, damage tolerance, residual strength

The objective of this paper is to briefly introduce damage tolerance analysis methodology by overviewing linear elastic fracture-mechanics (LEFM) concepts used to determine the influence of preexistent cracks on structural performance. The origin of the initial crack, whether it be a material flaw, induced by manufacturing, service, or assumed by decree, is not of concern here.

The scope of this paper is limited to a simplified overview of basic terminology and concepts, and is intended primarily as an introduction to the specialized discussions included elsewhere in this volume. Those desiring a more detailed development are referred to the several available fracture-mechanics textbooks [*1–7*]. In addition, a recent list of key references compiled by ASTM Subcommittee E24.06 on Fracture-Mechanics Applications [*8*] may be of interest.

A damage tolerance analysis addresses two points concerning an initially cracked structure. First, residual strength considerations determine the fracture

[1]Professor, School of Aeronautics and Astronautics, Purdue University, West Lafayette, IN 47907.

stress for a specified crack size. Second, it is necessary to predict the length of time (days, number of load cycles, missions, and so forth) required for a "subcritical" defect to grow to the size that causes fracture at the given load. It is assumed here that the crack can extend in a subcritical manner either by fatigue, stress corrosion cracking, or by combination of fatigue and corrosion.

The linear elastic fracture mechanics approach outlined here assumes that the stress intensity factor K controls crack growth. Attention is limited to nominally elastic behavior, although "small" amounts of crack-tip plasticity are allowed.

Stress Intensity Factor

The stress intensity factor K is the linear elastic fracture mechanics parameter that relates remote load, crack size, and structural geometry. The stress intensity factor may be expressed in the following form

$$K = \sigma\sqrt{\pi a}\beta \tag{1}$$

Here σ is the applied stress, a is the crack length, and β is a dimensionless factor that depends on crack length and component geometry. Stress intensity factor solutions have been obtained for many crack geometries, and several handbook compilations are available [*9–11*]. Some typical results are given in Fig. 1.

Examining the solutions in Fig. 1, note that the stress intensity factor K is an entirely different parameter than the familiar stress concentration factor K_t. The stress intensity factor has units of stress times the square root of length (conventional units are MPa·m$^{1/2}$ equal to 0.9102 ksi·in$^{1/2}$) and is a crack parameter. The stress concentration factor K_t, on the other hand, is a dimensionless term that describes the behavior of a notch (K_t = local stress/remote stress).

The formal definition of the stress intensity factor lies in the behavior of the linear elastic crack-tip stress field. Although a detailed crack-tip stress analysis is beyond the scope of this paper, the nature of crack-tip stresses for linear elastic behavior may be indicated by examining the limiting behavior of an elliptical notch located in a large plate loaded in remote tension as shown in Fig. 2. The tensile stress at the root of the major axis is given by

$$\sigma_{\text{tip}} = (1 + 2\sqrt{a/\rho})\sigma \tag{2}$$

Here a and c are the major and minor axes of the elliptical notch, σ is the remotely applied tensile stress, and ρ is the notch radius of curvature (recall that $\rho = c^2/a$ for an elliptical notch). Now, defining a crack as the limiting case when the elliptical notch radius $\rho \rightarrow 0$, the normal stress at the crack tip is given by

$$\begin{aligned} \sigma_{\text{crack tip}} &= \lim_{\rho \to 0} \sigma(1 + 2\sqrt{a/\rho}) \\ &= \lim_{\rho \to 0} 2\sigma\sqrt{a/\rho} \end{aligned} \tag{3}$$

Note that this simple estimate for the crack-tip stress indicates that the crack-tip stress is "square root singular," that is, the stress approaches infinity in the special manner $\lim_{\rho \to 0} \rho^{-1/2}$. The fact that all elastic crack problems have this characteristic

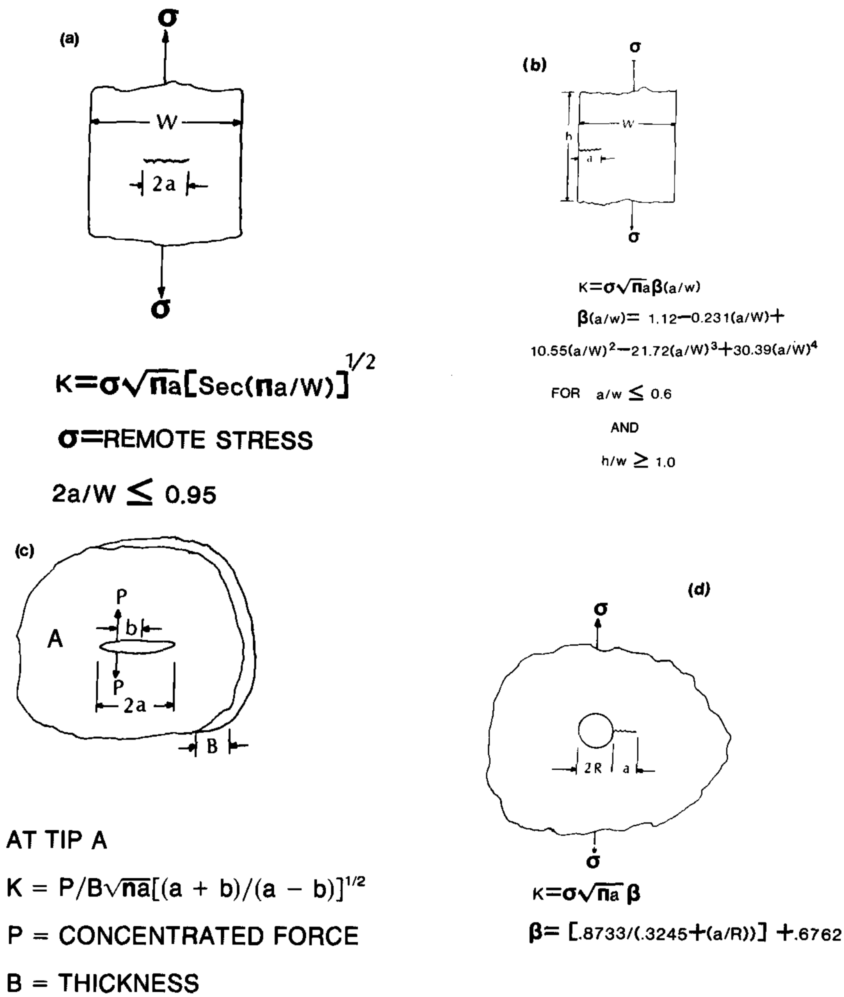

FIG. 1—*Typical stress intensity factor solutions for cracked members:* (a) *center-cracked strip,* (b) *edge-cracked strip,* (c) *point-loaded center cracks, and* (d) *radially cracked hole.*

square root singularity (see Refs *12* and *13* for mathematical proof) leads to the formal definition of the stress intensity factor.

Consider, for example, the three modes of crack opening shown schematically in Fig. 3. Mode I loading (opening mode) results when the crack faces move apart in the y-direction as shown in Fig. 3. The shearing Modes II and III result from loading components that cause relative sliding of the crack faces in either the x-direction (sliding Mode II) or the z-direction (tearing Mode III). The elastic stress fields ahead of the crack tips provide the following stress intensity factor definitions.

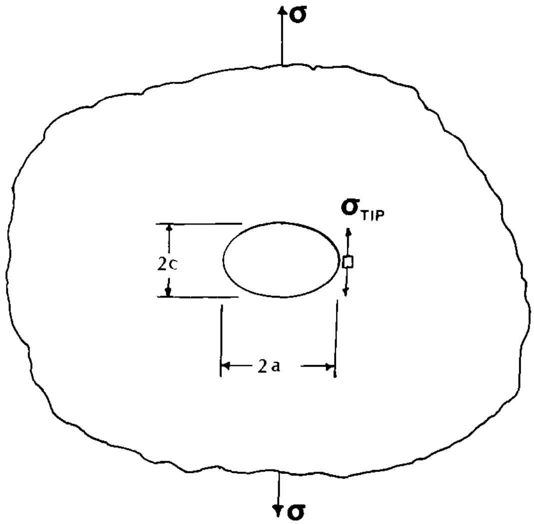

FIG. 2—*Schematic view of elliptical hole in a large plate loaded with remote tensile stress* σ.

$$
\begin{aligned}
K_{\mathrm{I}} &= \lim_{r\to 0} \sqrt{2\pi r}\,\sigma_y \\
K_{\mathrm{II}} &= \lim_{r\to 0} \sqrt{2\pi r}\,\sigma_{xy} \\
K_{\mathrm{III}} &= \lim_{r\to 0} \sqrt{2\pi r}\,\sigma_{yz}
\end{aligned}
\tag{4}
$$

Here K_{I}, K_{II}, and K_{III} are the Modes I, II, and III stress intensity factors, r is the distance from the crack tip, and σ_y, σ_{xy}, and σ_{xz} are the tensile, in-plane shear,

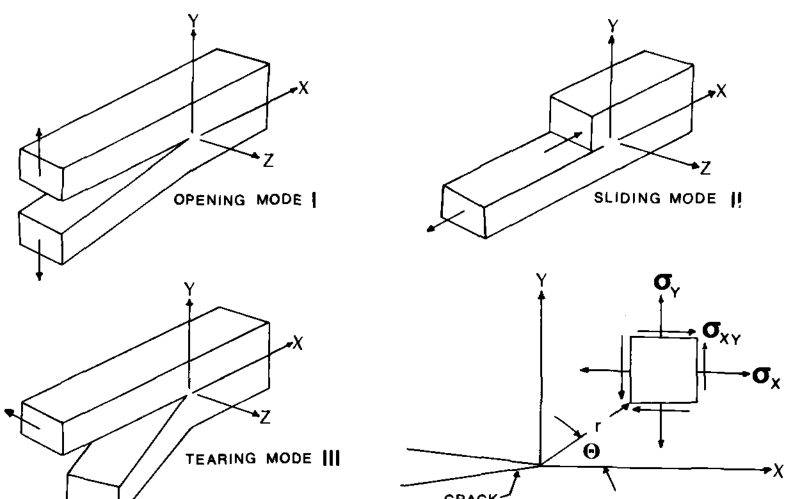

FIG. 3—*Three modes of crack opening and definition of* x-y *plane stresses for element located by polar coordinates* (r, θ) *near the crack tip.*

and out of plane shear stresses determined along the line $\theta = 0$ ahead of the crack tip (see Fig. 3).

Note that the stress intensity factor definitions given by Eq 4 only yield useful results if the crack-tip stresses have the "square root r" singularity ($\lim_{r\to 0} r^{1/2}$). If the stresses are proportional to r^{-1}, for example, Eq 4 would give infinite values for K_{I}, K_{II}, and K_{III}. If, on the other hand, the stresses were proportional to $r^{1/2}$ instead of $r^{-1/2}$, the three stress intensity factors $K_{\mathrm{I}} = K_{\mathrm{II}} = K_{\mathrm{III}} = 0$ by Eq 4. Thus, the definitions for the stress intensity factors are based on the fact that all elastic crack problems yield crack-tip stresses that are dominated by a term that behaves as $\lim_{r\to 0} r^{1/2}$.

Description and discussion of methods for computing stress intensity factors are beyond the scope of this paper. Details on solution techniques may be obtained by consulting Refs *3, 6, 8–11, 14, 15*. Reference *14* describes simple K calibration methods for engineering applications, while Ref *15* discusses solutions and techniques applicable to surface crack geometries.

Based on the stress intensity factor definitions given by Eq 4, the elastic stresses ($\sigma_x, \sigma_y, \sigma_z, \sigma_{xy}, \sigma_{xz}, \sigma_{yz}$) and the x, y, and z direction displacement (u, v, w) distributions in the vicinity of a crack tip are given below for the three modes of loading.

Mode I (Opening Mode)

Crack-tip stresses

$$
\begin{aligned}
\sigma_x &= (K_{\mathrm{I}}/\sqrt{2\pi r}) \cos(\theta/2)[1 - \sin(\theta/2)\sin(3\theta/2)] \\
\sigma_y &= (K_{\mathrm{I}}/\sqrt{2\pi r}) \cos(\theta/2)[1 + \sin(\theta/2)\sin(3\theta/2)] \\
\sigma_{xy} &= (K_{\mathrm{I}}/\sqrt{2\pi r}) \sin(\theta/2)\cos(\theta/2)\cos(3\theta/2) \\
\sigma_{xz} &= \sigma_{yz} = 0 \\
&\text{plane stress} \rightarrow \sigma_z = 0 \\
&\text{plane strain} \rightarrow \sigma_z = \nu(\sigma_x + \sigma_y)
\end{aligned}
\tag{5}
$$

Displacements

Plane strain

$$
\begin{aligned}
u &= (K_{\mathrm{I}}/G)(r/2\pi)^{1/2} \cos(\theta/2)[1 - 2\nu + \sin^2(\theta/2)] \\
v &= (K_{\mathrm{I}}/G)(r/2\pi)^{1/2}\{\sin(\theta/2)[2 - 2\nu - \cos^2(\theta/2)]\}
\end{aligned}
\tag{6}
$$

Plane stress

$$
\begin{aligned}
u &= (K_{\mathrm{I}}/G)(r/2\pi)^{1/2}\{\cos(\theta/2)[(1 - \nu)/(1 + \nu) + \sin^2(\theta/2)]\} \\
v &= (K_{\mathrm{I}}/G)(r/2\pi)^{1/2} \sin(\theta/2)[2/(1 + \nu) - \cos^2(\theta/2)]
\end{aligned}
\tag{7}
$$

Mode II (Sliding Mode)

Stresses

$$\begin{aligned}
\sigma_x &= (-K_{\mathrm{II}}/\sqrt{2\pi r})\ \sin(\theta/2)\,[2 + \cos(\theta/2)\ \cos(3\theta/2)] \\
\sigma_y &= (K_{\mathrm{II}}/\sqrt{2\pi r})\ \sin(\theta/2)\ \cos(\theta/2)\ \cos(3\theta/2) \\
\sigma_{xy} &= (K_{\mathrm{II}}/\sqrt{2\pi r})\ \cos(\theta/2)\,[1 - \sin(\theta/2)\ \sin(3\theta/2)] \\
\sigma_{xz} &= \sigma_{yz} = 0
\end{aligned} \tag{8}$$

$$\text{for plane stress} \rightarrow \sigma_z = 0$$

$$\text{plain strain} \rightarrow \sigma_z = \nu(\sigma_x + \sigma_y)$$

Displacements (plane strain $w = 0$)

$$\begin{aligned}
u &= (K_{\mathrm{II}}/G)\,(r/2\pi)^{1/2}\ \sin(\theta/2)\,[2 - 2\nu + \cos^2(\theta/2)] \\
v &= (K_{\mathrm{II}}/G)\,(r/2\pi)^{1/2}\ \cos(\theta/2)\,[-1 + 2\nu + \sin^2(\theta/2)]
\end{aligned} \tag{9}$$

Mode III (Tearing Mode)

Stresses

$$\begin{aligned}
\sigma_{xz} &= (-K_{\mathrm{III}}/\sqrt{2\pi r})\ \sin(\theta/2) \\
\sigma_{yz} &= (K_{\mathrm{III}}/\sqrt{2\pi r})\ \cos(\theta/2) \\
\sigma_x &= \sigma_y = \sigma_z = \sigma_{xy} = 0
\end{aligned} \tag{10}$$

Displacements

$$\begin{aligned}
u &= v = 0 \\
w &= (K_{\mathrm{III}}/G)\,(2r/\pi)^{1/2}\ \sin(\theta/2)
\end{aligned} \tag{11}$$

In Eqs 5 through 11, G is the elastic shear modulus, ν is poisson's ratio, and (r, θ) are the polar coordinates for the particular point where the stresses or displacements are evaluated. Note that Eqs 5 through 11 are limited to points "near" the crack tip (for example, for $r <$ 10% of the crack length). The manner in which stress intensity factors are used to characterize crack growth is described in later sections. The next section, however, deals with estimates of crack-tip plastic zone sizes and is intended to provide guidelines for when one can reasonably expect the stress intensity factor to be a valid crack-growth parameter.

Crack-Tip Plasticity

As discussed in the preceeding section, the formal stress intensity factor definition is based on the fact that all elastic crack problems theoretically yield square root singular stresses. It is obvious that no real material can withstand infinite stresses, however, and plastic deformation will occur at actual crack tips. Since subsequent sections will demonstrate how stress intensity factor relationships are

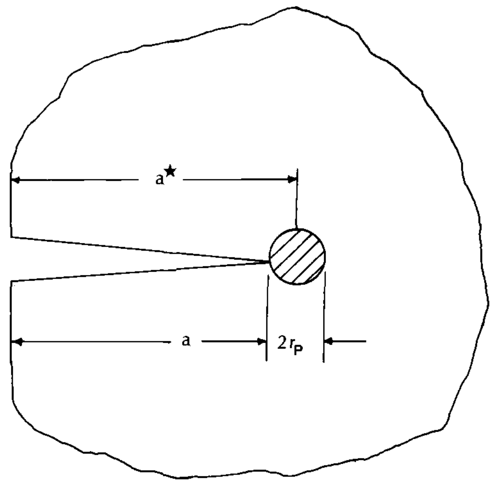

FIG. 4—*Schematic view of circular plastic zone ahead of crack with length* a, *showing definition of effective crack length* a*.

used to analyze fracture, fatigue crack growth, and stress corrosion cracking, it is important here to estimate the extent of crack-tip plasticity in order to assess the validity of K as a crack characterization parameter. Two plastic zone models are described below. Both are limited to small scale yielding; a rigorous plasticity analysis is not attempted. The result of these plastic zone estimates will be used in subsequent sections to explain limitations to the linear elastic fracture mechanics approach.

Circular Plastic Zone

Consider the y component of normal stress along the line $\theta = 0$ ahead of a crack tip loaded in Mode I. The dependence of this normal stress on the stress intensity factor and the distance from the crack tip is obtained from Eq 5

$$\sigma_y = (K_I/\sqrt{2\pi r}) \tag{12}$$

At the crack tip ($r = 0$) the stress is infinite. Solving Eq 12 for the distance r_p when the normal stress σ_y equals the tensile yield stress σ_{YS} gives

$$r_p = (1/2\pi)(K_I/\sigma_{YS})^2 \tag{13}$$

Irwin [*16*] suggested that for "small scale" yielding, crack-tip plasticity is confined to a circular zone of radius r_p ahead of the crack front as shown schematically in Fig. 4. He also proposed an "effective" crack length a^* whose tip acts at the center of the plastic zone

$$a^* = a + r_p \tag{14}$$

Within the plastic zone, stresses equal the yield strength σ_{YS}. Outside the plastic zone, stresses are given by Eq 5, evaluated for the effective crack length a^*.

Note that the circular plastic zone model given by Eq 13 is limited to small plastic zones relative to the crack length a (that is, $r_p < a/10$). The model is applicable to any Mode I flaw since geometry effects are contained in the stress intensity factor term K_I.

Von Mises Plastic Zone

A more sophisticated estimate for the extent of crack-tip plasticity uses the von Mises yield criterion. By this criterion, yielding occurs for a particular state of stress (σ_x, σ_y, σ_z, σ_{xy}, σ_{yz}, σ_{xz}) when

$$2\sigma_{YS}{}^2 = (\sigma_x - \sigma_y)^2 + (\sigma_x - \sigma_z)^2 + (\sigma_y - \sigma_x)^2 + 6(\sigma_{xy}{}^2 + \sigma_{xz}{}^2 + \sigma_{yz}{}^2) \qquad (15)$$

Since the stresses are known in the vicinity of the crack tip, Eq 15 can be used to determine the region where crack-tip yielding begins.

In Mode I loading, for example, the stresses near the crack tip are given by Eq 5. Combining Eqs 5 and 15 gives the polar coordinates (r, θ) for the boundary where yielding begins. For plane stress conditions (defined as the state of stress for which $\sigma_z = 0$), the resulting elastic-plastic boundary is given by

$$r_p{}^* = (1/2\pi)(K_I/\sigma_{ys})^2 \cos^2(\theta/2)[1 + 3\sin^2(\theta/2)] \qquad (16)$$

For plane strain, specified by $\varepsilon_z = 0$, combining Eqs 5 and 15 gives

$$r_p{}^* = (1/2\pi)(K_I/\sigma_{ys})^2 \cos^2(\theta/2)[(1 - 2\nu)^2 + 3\sin^2(\theta/2)] \qquad (17)$$

Comparing plots of Eqs 16 and 17 in Fig. 5, note that the plane stress plastic zone is considerably larger than the zone that occurs for plane strain. The fact that crack-tip yielding depends on the state of stress is a significant result, which will be useful later for explaining thickness effects in fracture. In addition, note that at $\theta = 0$, Eq 16 reduces to the circular plastic zone radius given by Eq 13.

Fracture

Residual strength calculations determine the fracture stress as a function of crack size for a given component. Simply stated, the LEFM fracture criterion uses the experimentally observed fact that many "brittle" materials fracture when the stress intensity factor reaches a "critical" value

$$K = K_c = \text{constant at fracture} \qquad (18)$$

Here K_c is a material property called the "fracture toughness" of the material and is the limiting stress intensity factor that causes catastrophic fracture in all components made from the same material. Note that since K relates load, crack length, and structural geometry (recall Eq 1 and Fig. 1), this simple fracture criterion allows one to relate fracture measurements from laboratory specimens with failure of a different structural component. (It is assumed in Eq 18 that all components are subjected to the same mode of crack opening. In general,

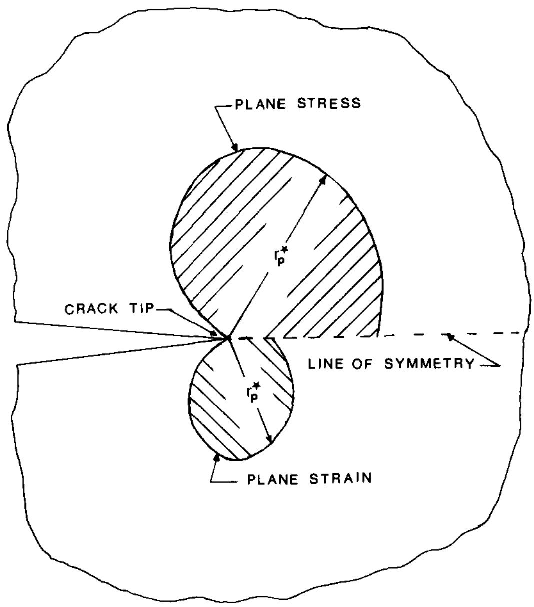

FIG. 5—*Comparison of Mode I plastic zone sizes for plane stress and plane strain as computed by Eqs 16 and 17 (plastic zones are symmetric).*

Modes I, II, and III loadings are not expected to give the same fracture toughness value.) Fracture toughness values for many structural materials are reported in material handbooks [*17*, *18*].

Example

Assume that a large panel contains a 2.5-cm (1.0-in.) diameter hole with a radial crack located perpendicular to the applied tensile load. It is known that 1.5-cm (0.6-in.) long cracks can occur at the hole. A 10.2-cm (4.0-in.) wide edge-cracked laboratory specimen made from an identical sheet of material fractures at a stress of 34.7 MPa (5 ksi) when the crack length is 5.1 cm (2.0 in.). Both sheets are 2.5-cm (1.0-in.) thick, and the material has a 450 MPa (65 ksi) yield strength. Determine the residual strength of the panel with the cracked hole.

In order to apply the fracture criterion given by Eq 18, the fracture toughness K_c must be computed for the structural material. Using the stress intensity factor solution from Fig. 1*b* for the edge-cracked strip gives

$$K = \sigma\sqrt{\pi a}[1.12 - 0.231(a/w) + 10.55(a/w)^2 - 21.72(a/w)^3 + 30.39(a/w)^4] \tag{19}$$

Letting σ = 34.7 MPa, a = 5.1 cm, and w = 10.2 cm, the fracture toughness is found to be K_c = 39.3 MPa$\cdot$m$^{1/2}$ = 35.8 ksi$\cdot$in.$^{1/2}$. Now, since all components made from this sheet of material fracture when the stress intensity factor achieves the limiting fracture toughness value, the residual strength for the member with the cracked hole can be computed. Combining Eq 18 and the stress intensity factor solution [*19*] for the cracked hole (see Fig. 1*d*) gives

$$K = K_c = \sigma\sqrt{\pi a}\{0.8733/[0.3245 + (a/R)] + 0.6762\} \tag{20}$$

Now, $K_c = 39.3$ MPa·m$^{1/2}$ from before, $a = 1.5$ cm, and $R = 1.25$ cm. Solving Eq 20 gives $\sigma = 145$ MPa (21.0 ksi) as the residual strength of the cracked hole.

Additional Considerations

Although the previous example has been greatly simplified, it does describe the general procedure for computing the residual strength of a given component. Note the critical crack size could also have been calculated had the stress been fixed, or other geometries considered provided the appropriate stress intensity factors are known. The remainder of this section briefly describes several other points that should be considered when calculating fracture loads.

The LEFM fracture criterion (Eq 18) assumes that the stress intensity factor is a valid crack parameter and that the material behaves in a "brittle" manner. For purposes here, one can define a brittle material as one where the crack length is large in comparison to the plastic zone size

$$a > 10r_p \tag{21}$$

Thus, Eq 21 represents a general rule of thumb for determining fracture problems that can be confidentially analyzed by the critical stress intensity factor criterion. Since the tensile yield strength was 450 MPa (65 ksi) in the previous example, the plastic zone size at fracture computed by Eq 11 is

$$\begin{aligned} r_p &= (1/2\pi)(K_c/\sigma_{YS})^2 \\ &= (1/2\pi)(39.3/450)^2 = 0.0012 \text{ m} \end{aligned}$$

Thus, one could expect fracture of all cracks larger than $10\ r_p = 1.2$ cm to be governed by the K_c criterion given by Eq 18. Cracks smaller than this size would most likely withstand larger fracture stresses, since plasticity causes the material to behave in a more ductile manner. Development of elastic-plastic fracture criteria is a significant area of current research beyond the scope of the present paper [*20*].

The fracture toughness K_c can be a thickness dependent material property. As shown schematically in Fig. 6, tests from specimens made from the same material, but with different thicknesses, indicate that K_c decreases as the thickness B increases until a minimum value designated K_{Ic} is achieved. This initial reduction in toughness with thicker specimens is also accompanied by a change in mode of crack growth as shown in Fig. 7. The "slanted" fracture surface for "thin" specimens indicates that the crack grew along a shear plane inclined at 45° to the

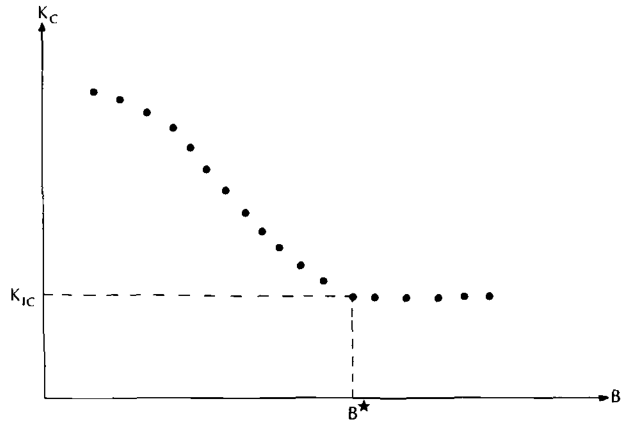

FIG. 6—*Effect of specimen thickness* B *on fracture toughness* K_c.

load axis, in a combination of Modes I and II. The thick specimens fracture along a plane perpendicular to the load axis in a pure Mode I manner, except for small "shear lips" near the specimen edge, where the crack plane is again angled at 45°.

The change in fracture appearance and K_c for different thicknesses can be explained by the fact that the crack-tip plastic zone depends on the state of stress. Recall that the plane stress plastic zone (Eq 16) is larger than that for plane strain (Eq 17). Since plane strain occurs at the center of a thick sheet, while plane stress exists at free surfaces, the crack-tip plastic zone would be expected to vary through the specimen thickness and have the characteristic "dumbbell" shape shown in Fig. 8. The thin sheet is under plane stress, has a larger plastic zone (on a volume basis), and exhibits greater "toughness" than the thicker plane strain sheet. Moreover, the crack propagates through the small plane strain plastic zone in a "flat" Mode I manner, while the larger plane stress plastic zone causes a shear type failure resulting in the slanted fracture surface in the thin sheet. The shear lips at the edge of the thick specimen are a result of the plane stress conditions at the free surfaces.

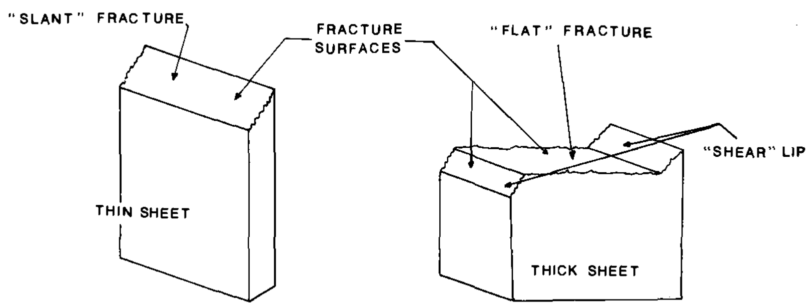

FIG. 7—*Effect of specimen thickness on fracture surface appearance for thin and thick sheets.*

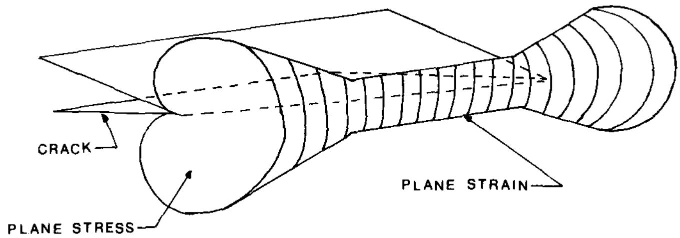

FIG. 8—*Effect of specimen thickness on crack-tip plastic zone showing three-dimensional "dumbbell" shaped crack-tip plastic zone.*

Since the fracture toughness varies with specimen thickness, considerable emphasis has been placed on developing methods to measure the minimum "plane strain fracture toughness K_{Ic}." (Note that the subscript I emphasizes that the "critical" stress intensity factor has been determined for the pure Mode I "flat fracture" that occurs under plane strain conditions.) Standard procedures for measuring K_{Ic} are given in ASTM Test for Plane-Strain Fracture Toughness of Metallic Materials (E 399).

An empirical observation sometimes used to estimate the minimum plate thickness B^* required to exhibit the plane strain K_{Ic} fracture is given by

$$B^* \geq 2.5(K_c/\sigma_{ys})^2 \tag{22}$$

The fracture toughness K_c is measured for a particular sheet, and B^* computed by Eq 22. If the actual sheet thickness exceeds B^* then the K_c value can be expected to equal the minimum K_{Ic} value.

Considering the earlier example with the edge-cracked sheet, the yield stress was 450 MPa (65 ksi), the sheet thickness was 2.5 cm (1.0 in.), and K_c was computed to be 39.3 MPa·m$^{1/2}$ (35.8 ksi·in.$^{1/2}$). Now, by Eq 22

$$B^* = 2.5(39.3/450)^2 = 0.019 \text{ m}$$

Since the actual plate thickness was 2.5 cm, we would expect the measured value of 39.3 MPa·m$^{1/2}$ to be the plane strain fracture toughness K_{Ic}. All components greater than 1.9 cm thick would be expected to fracture at the same fracture toughness value. Components thinner than 1.9 cm could be expected to have larger toughness values (K_c) and, thus, be more resistant to fracture. It should be emphasized that Eq 22 is only used for estimation purposes and that the more rigorous requirements given in ASTM E 399 are needed to ensure that the K_{Ic} is actually measured.

Fatigue Crack Growth

This section introduces the LEFM approach for predicting fatigue crack growth lives for members subjected to cyclic loading. It is assumed the component of interest contains a preexistent crack of length a_0, and it is desired to determine the number of load cycles N_f required to grow the initial flaw to some final size

a_f. The final crack length could be the fracture size computed by the procedure discussed in the preceeding section or could be a smaller flaw specified by some other criterion (for example, ease of repair, inclusion of a safety factor, and so forth).

The fracture mechanics approach to fatigue is based on work by Paris et al [*21*] and Paris [*22*], who showed that the cyclic range in stress intensity factor ΔK controls the fatigue-crack-growth rate da/dN. Here ΔK is the difference between the maximum and minimum stress intensity factors for a particular cycle of loading

$$\begin{aligned} \Delta K &= K_{\max} - K_{\min} \\ &= (\sigma_{\max} - \sigma_{\min})\sqrt{\pi a}\,\beta \\ &= \Delta\sigma\sqrt{\pi a}\,\beta \end{aligned} \tag{23}$$

In Eq 23 $\Delta\sigma$ is the cyclic stress, a is the crack length, and β is a dimensionless function of crack size as before.

The fact that ΔK controls the rate of fatigue crack growth, and thus cyclic life, can be demonstrated in several ways. Anderson and James [*23*], for example, describe a series of fatigue-crack-growth tests with large center cracked panels. As shown schematically in Fig. 9, one group of specimens were loaded remotely with a constant cyclic stress $\Delta\sigma$, while the remaining panels were symmetrically loaded along the crack faces with a cyclic force ΔP (point loading).

The specimens were placed in a fatigue machine and tested so that the cyclically applied load amplitude was fixed at either $\Delta\sigma$ or ΔP. Crack lengths were measured at periodic cyclic intervals and plotted as a function of elapsed cycles N. Schematic crack length versus cycle curves are shown in Fig. 9.

Note the different crack-growth behavior for the two types of loadings. The remotely stressed cracks grew at an increasing rate as the crack length increased. (The slope da/dN of crack length versus cycle curve increased as the test progressed.) The crack face loading gave entirely different results, however, as the growth rate da/dN decreased with longer crack lengths. Although this difference in crack-growth rate may seem surprising at first, one group of cracks grew faster while the other cracks slowed down as the test progressed, the results can be explained in terms of the cyclic stress intensity factor ΔK.

Stress intensity factors for the two specimens are given in Figs. 1*a* and 1*c*. Assuming that the plate width is large in comparison to the crack size ($a/w \rightarrow 0$), those results simplify to

$$\Delta K = \Delta\sigma\sqrt{\pi a} \tag{24}$$

for the remotely stressed plate, and to

$$\Delta K = \Delta P/(B\sqrt{\pi a}) \tag{25}$$

for the crack face loading (the distance $b = 0$ in Fig. 1*c*). Comparing Eqs 24 and 25, note the significant difference in dependence of ΔK on crack length. The

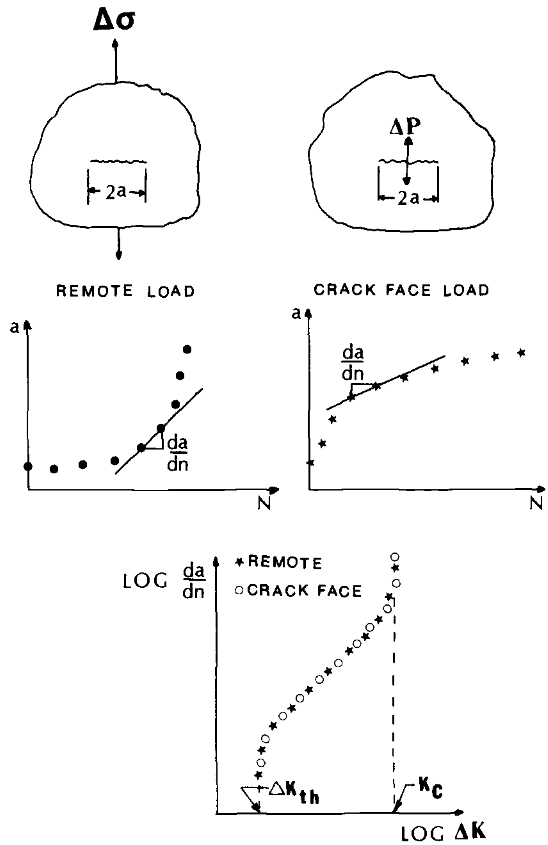

FIG. 9—*Comparison of crack length* a *versus elapsed cycles* N *data for remote and crack face loaded specimens and combined plot of fatigue crack growth rate* da/dN *versus cyclic stress intensity factor* ΔK.

stress intensity factor range increases as the crack grows for the remotely stressed plate (Eq 24) while ΔK decreases with increasing crack size for the crack face loading (Eq 25).

The results from the two sets of experiments agree well when the fatigue crack growth rate is plotted versus the cyclic stress intensity factor (see schematic log da/dN versus log ΔK curve in Fig. 9). Here da/dN is measured from the crack length a versus elapsed cycles N curve for a particular crack size, and ΔK is computed for that crack length. Note that the data from the two different crack geometries lie on the same da/dN versus ΔK curve, indicating that the cyclic stress intensity factor ΔK is the parameter that controls fatigue-crack-growth rate.

Actual test data for an annealed 304 stainless steel [*24*] and 7075-T6 aluminum [*18*] are given in Figs. 10 and 11. The different symbols in Fig. 10 indicate results for different shaped specimens machined from the same piece of material. The

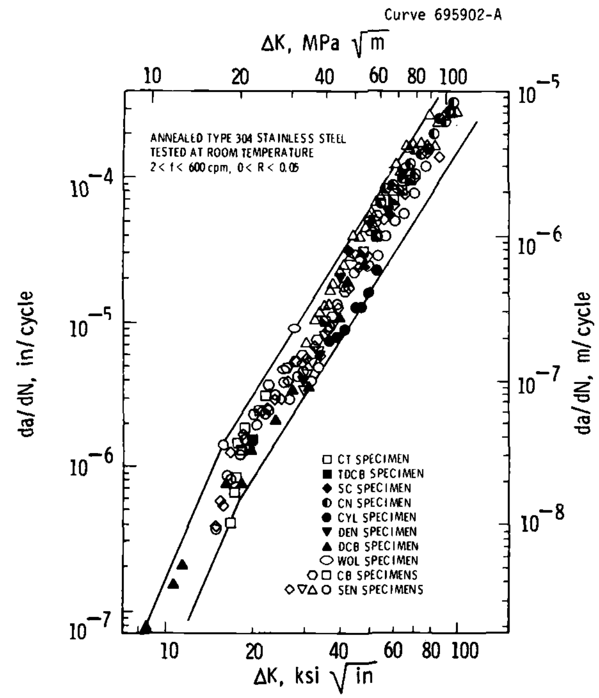

FIG. 10—*Fatigue crack growth data for annealed 304 stainless steel illustrating geometry independence* [24].

various specimen types were subjected to constant amplitude loading and the crack length measured as a function of elapsed cycles N. The fatigue crack growth rate da/dN was computed at various crack lengths as before, and plotted versus the corresponding range in cyclic stress intensity factor (using the appropriate K equation for that particular specimen geometry). Again, note that fatigue crack growth rates for different crack configurations lie on a single da/dN versus ΔK curve. The curves can be a function of mean stress, however, as shown in Fig. 11, where different results are obtained for different stress ratios R. (Stress ratio R = minimum/maximum stress in load cycle.)

The LEFM approach to fatigue is based on the fact that the experimentally determined da/dN versus ΔK curve can be effectively treated as a property of the particular material of interest. Standard procedure for obtaining the da/dN versus ΔK curve are recommended by ASTM Test for Constant-Load-Amplitude Fatigue Crack Growth Rates Above 10^{-8} m/Cycle (E 647), and handbook data are available for common structural materials [*17, 18*].

When collected over a wide range of crack growth rates, da/dN versus ΔK curves for many materials have the characteristic sigmoidal shape shown schematically in Fig. 9. A vertical asymptote is observed at $\Delta K = K_c$, since fracture occurs at that point. There may also be an asymptote at low ΔK levels, designated

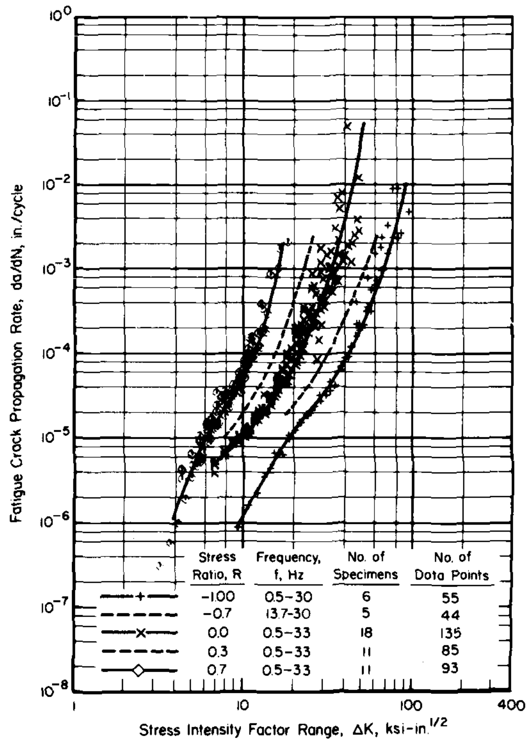

FIG. 11—*Fatigue crack growth data for 2.286-mm* (0.090-in.) *thick 7075-T6 aluminum sheet showing effect of stress ratio* R *(reproduced from Ref* 18*).*

as the fatigue threshold stress intensity factor ΔK_{TH}. Below ΔK_{TH} cracks do not extend by cyclic loading. Measuring ΔK_{TH} can be difficult, however, involving long test times and many other practical problems. (ASTM Task Group E24.04.03 is currently studying fatigue-crack-growth-threshold testing procedures.)

A linear relation between log da/dN and log ΔK is sometimes observed between the upper and lower asymptotes. Paris et al [*21*, 22] expressed the crack-growth behavior in that region by the simple power law

$$da/dN = C\Delta K^m \tag{26}$$

Here C and m are empirical constants obtained for a particular set of data. The exponent m is a dimensionless quantity that typically lies in the range $2 < m < 9$.

Many other more general crack-growth equations have been used in the literature to relate da/dN with ΔK. One expression suggested by Forman et al [*25*], for example, also includes the stress ratio term R and another empirical constant K_c to reflect the upper asymptote in da/dN as ΔK approaches the fracture toughness of the material

$$da/dN = (C\Delta K^m)/[(1 - R)K_c - \Delta K] \tag{27}$$

This expression has been successfully used to represent da/dN versus ΔK curves for different stress ratios by a single mathematical expression. In general, many other models of the following form have also been used

$$da/dN = F(K) \tag{28}$$

Here $F(K)$ is a mathematical expression that fits da/dN over an appropriate range of ΔK values, including the upper and lower asymptotes. The empirical model may also account for other loading variables such as mean stress, temperature, and so forth.

Returning now to the original objective of predicting the fatigue crack growth life, it is a simple task to integrate Eq 28 for the total cycles N_f required to grow an initial crack of length a_0 to some final size a_f. Solving Eq 28 for the cyclic life gives

$$N_f = \int_{a_0}^{a_f} [da/F(K)] \tag{29}$$

As an example, compute the fatigue crack growth life for an edge crack located in a semi-infinite strip (Fig. 1*b* configuration with $a/w \rightarrow 0$). Assume the initial crack size a_0, the constant amplitude stress $\Delta\sigma$, and the final crack size a_f are known. In addition, assume fatigue crack growth is adequately described by Eq 26, where C and m are known material constants. Now, the stress intensity factor equation obtained from Fig. 1*b* for the edge-crack simplifies to

$$K = \sigma\sqrt{\pi a}\,1.12 \tag{30}$$

Combining Eqs 26, 29, and 30, and integrating gives

$$\begin{aligned} N_f &= \int_{a_0}^{a_f} [da/F(K)] \\ &= \int_{a_0}^{a_f} (da/C\Delta K^m) = \int_{a_0}^{a_f} da/[C(1.12\Delta\sigma\sqrt{\pi a})^m] \\ N_f &= \{1/[C(1.12\Delta\sigma\sqrt{\pi})^m(1 - 0.5\,m)]\}[a_f^{1-0.5m} - a_0^{1-0.5m}] \end{aligned} \tag{31}$$

Note that a closed form solution has been obtained for the fatigue crack growth life for this particular example. The loading is determined by the constant amplitude stress $\Delta\sigma$; the material is specified by the constants C and m (and the choice of Eq 26 for the crack growth model), and the component geometry is reflected by the crack sizes a_i, a_f, and by the edge-cracked stress intensity factor (Eq 30). Since most practical problems are more complex, involving complicated stress intensity factor equations or fatigue crack growth models or both, it is usually not possible to integrate Eq 29 in closed form as in this example. In those cases, a numerical integration scheme is used. Moreover, variable amplitude load histories (where $\Delta\sigma$ is not constant) can be considered by cycle-by-cycle integration methods. Engle describes various procedures used to compute fatigue crack growth lives for more general problems.[2]

As a final note, it is important to recognize limitations to the stress intensity factor based approach described here. It is, of course, assumed that K is a valid crack parameter and that crack-tip plasticity effects are negligible. Large peak loads applied during the fatigue cycling can introduce large plastic zones that significantly influence subsequent fatigue crack growth (cause fatigue crack retardation). Procedures for analyzing peak overloads and other load history effects are described by Saff.[3] Mean stress, temperature, and environmental influences may also be significant. In addition, problems can arise when considering very small crack sizes. (ASTM Task Group E24.04.06 is currently studying the "small" crack problem.)

Stress Corrosion Cracking

The chemical and thermal environment subjected to a component can significantly influence crack growth under both static and cyclic loading. Environmentally assisted crack growth resulting from a sustained static load is known as stress corrosion cracking, while the combined action of a cyclic load and an "aggressive" environment is commonly called corrosion fatigue. This section briefly outlines the fracture mechanics approach to stress corrosion cracking.

The stress corrosion cracking phenomenon can be described with the aid of Fig. 12. Imagine that a series of specimens are machined from a single sheet of steel and preflawed to various crack lengths. The members are immersed in a tank of salt water (or some other environment of interest) and subjected to a fixed load. The cracks in some specimens grow and eventually cause fracture, with the total failure time being dependent on the initial crack size. Plotting the initially applied stress intensity factor K (computed with the applied load and initial crack size) versus the time t_f to specimen failure gives the K versus t_f curve shown schematically in Fig. 12. Note that specimens initially loaded to the fracture toughness K_c value fracture immediately but that as the applied K is reduced for other specimens, crack growth life increases until a "threshold" value of stress intensity factor, labeled K_{ISCC}, is reached. (The subscripts ISCC denote Mode I stress corrosion cracking.) Specimens loaded below K_{ISCC} do not fracture but have "infinite" stress corrosion lives. The K_{ISCC} value is an important measure of a material's ability to resist stress corrosion cracking and will vary for different alloys and chemical environments. Stress corrosion cracking threshold values are available for many common structural material/environment combinations [*17, 18*]. It should be noted that the K_{ISCC} value may be a function of time for more stress corrosion cracking materials such as tough steels and aluminums.

[2]Engle, R. M., in this publication, pp. 25–35.
[3]Saff, C. R., in this publication, pp. 36–49.

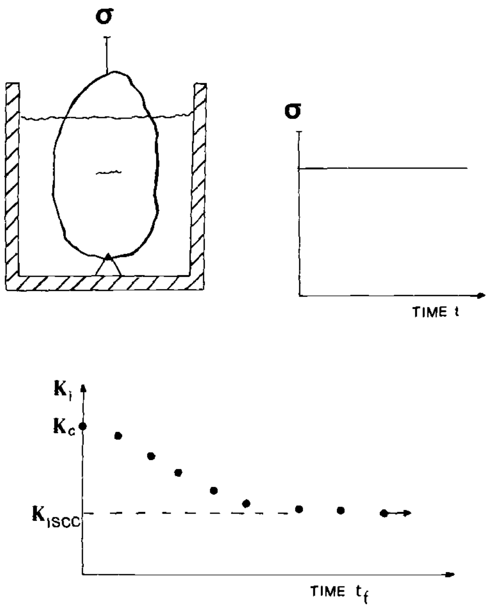

FIG. 12—*Schematic representation of cracked specimen immersed in an "aggressive" environment and subjected to sustained stress and resulting plot of initial stress intensity factor* K_i *versus specimen life* t_f *for several tests.*

If crack lengths were measured as a function of elapsed time, instead of recording only total time to failure, the stress corrosion data could be expressed in a crack growth rate format similar to that used for fatigue. In this case, the crack growth rate da/dt would be computed from the crack length versus time data and plotted versus the stress intensity factor for the corresponding crack (computed for the sustained load using the appropriate stress intensity factor equation). Typical data [*17*] for 300M steel tested in distilled water (the aggressive environment) are shown in Fig. 13. Note that in this case the crack growth rate da/dt is expressed in units of length per time, instead of length per cycle as for fatigue.

Again the log da/dt versus log K curve assumes a sigmoidal shape between a lower K_{ISCC} and upper K_C asymptote. As before, these data could be represented by an empirical equation.

$$da/dt = f(K) \tag{32}$$

Here $f(K)$ is some convenient mathematical function of K. Now, the total time t_f required to grow a crack from length a_0 to a_f is given by

$$t_f = \int_{a_0}^{a_f} (da)/[f(K)] \tag{33}$$

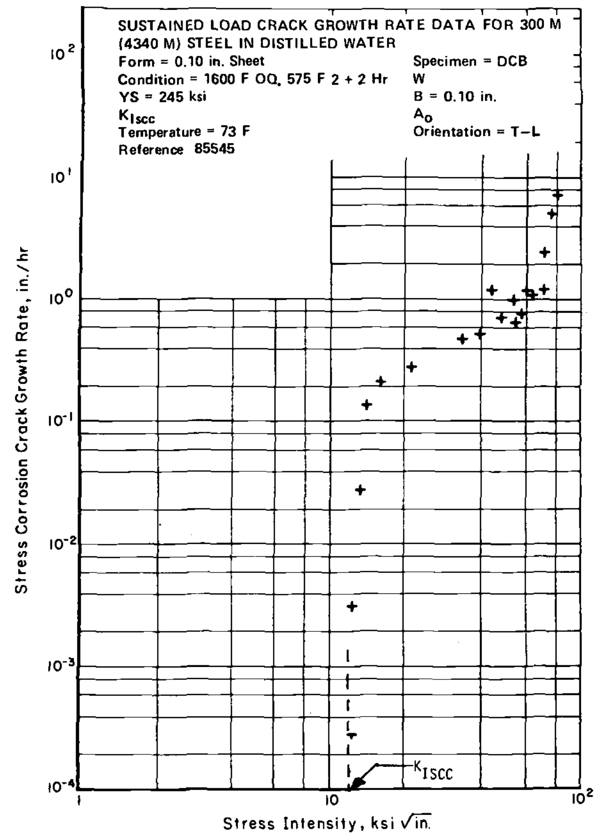

FIG. 13—*Sustained load stress corrosion cracking data for 300M steel in distilled water (reproduced from Ref* 17).

Note that different crack geometries and material property curves are treated in a manner analogous to computing fatigue crack growth lives.

It is important here to also note the significant effect environment has when combined with cyclic loading. In general, corrosion fatigue crack growth rates can be considerably faster than observed for cyclic loading in an inert environment. The influence the environment plays on fatigue life depends on the cyclic frequency, the shape of the applied load versus time curve, the temperature, the environment, the crack orientation (with respect to material axes), and, of course, the particular material of interest. Since so many variables can influence corrosion fatigue, it is best to collect data as closely to anticipated service conditions as possible.

Concluding Remarks

This paper outlines the stress intensity factor approach for analyzing cracked structures. Although small amounts of crack-tip plasticity are allowed, elastic behavior is nominally assumed. Fatigue crack growth or fracture problems involving "large" scale plasticity must be analyzed by other crack parameters (*R* curve, *J* integral, crack opening displacement, and so forth). Reference to these "nonlinear" approaches is found in Refs *2–8* and *20*.

In spite of the small scale plasticity limitation, many practical problems[4] can be analyzed to a reasonable degree of accuracy with the stress intensity factor approach. The method has been developed to a degree where stress intensity factor solutions [*9–11*] and LEFM material property data [*17, 18*] are available in handbook form. In addition, standard test procedures (ASTM E 399 and E 647) have been developed for measuring the crack-growth material properties.

References

[*1*] Tetelman, A. S. and McEvily, A. J., Jr., *Fracture of Structural Materials*, John Wiley and Sons, New York, 1967.

[*2*] Knott, J. F., *Fundamentals of Fractures Mechanics*, John Wiley and Sons, New York, 1973.

[*3*] Broek, D., *Elementary Engineering Fracture Mechanics*, Noordhoff International Publishing, Leyden, Netherlands, 1974.

[*4*] Hertzberg, R. W., *Deformation and Fracture Mechanics of Engineering Materials*,, John Wiley and Sons, New York, 1976.

[*5*] Rolfe, S. T. and Barsom, J. M., "*Fracture and Fatigue Control in Structures-Applications of Fracture Mechanics*," Prentice-Hall, Inc., Englewood Cliffs, NJ, 1977.

[*6*] Parker, A. P., *The Mechanics of Fracture and Fatigue*, E. & F. N. Spon, London, England, 1981.

[*7*] H. Liebowitz, Ed., *Fracture An Advanced Treatise*, Volume I-VII, Academic Press, New York, 1969–1970.

[*8*] Toor, P. M., "References and Conference Proceedings in the Understanding of Fracture Mechanics," draft report submitted to ASTM Subcommittee E24.06 on Fracture Application, American Society for Testing Materials, Philadelphia, June 1982.

[*9*] Sih, G. C., *Handbook of Stress Intensity Factors for Researchers and Engineers*, Institute of Fracture and Solid Mechanics, Lehigh University, Bethleham, PA, 1973.

[*10*] Tada, G., Paris, P., and Irwin, G., *The Stress Analysis of Cracks Handbook*, Del Research Corporation, Hellertown, PA, 1973.

[*11*] Rooke, D. P. and Cartwright, D. J., *Compendium of Stress Intensity Factors*, Her Majesty's Stationary Office, England, 1976.

[*12*] Williams, M. L., "On the Stress Distribution at the Base of a Stationary Crack," *Journal of Applied Mechanics*, Vol. 24, No. 1, 1957, pp. 109–114.

[*13*] Eftis, J., Subramonian, N., and Liebowitz, H., "Crack Border Stress and Displacement Equations Revisited," *Engineering Fracture Mechanics*, Vol. 9, No. 1, 1977, pp. 189–210.

[*14*] Rooke, D. P., Baratta, F. I., and Cartwright, D. J., "Simple Methods of Determining Stress Intensity Factors," *Engineering Fracture Mechanics*, Vol. 14, No. 2, 1981, pp. 397–426.

[*15*] "A Critical Evaluation of Numerical Solutions to the 'Benchmark' Surface Flaw Problem," *Experimental Mechanics*, Vol. 20, No. 8, Aug. 1980, pp. 253–264.

[*16*] Irwin, G. P., "Fracture," *Handbuch der Physik*,, Vol. VI, Springer, Berlin, 1958, p. 551.

[*17*] *Damage Tolerance Design, A Compilation of Fracture and Crack-Growth Data for High-Strength Alloys, Metals and Ceramics Information Center*, Battelle Columbus Laboratories, Columbus, OH, 1975.

[*18*] *Metallic Materials and Elements for Aerospace Vehicle Structures*, Military Standardization Handbook MIL-HDBK-5C, Naval Publication and Forms Center, Philadelphia, 1978.

[*19*] Grandt, A. G., Jr., "Stress Intensity Factors for Some Thru-Cracked Fastener Holes," *International Journal of Fracture*,, Vol. 11, No. 2, April 1975, pp. 283–294.

[4]In this publication: Chang, J. B., pp. 50–68; Swift, T., pp. 69–107; and Forman, R. G. and Hu, T., pp. 108–133.

[20] *Elastic-Plastic Fracture, STP 668,* J. D. Landes, J. A. Begley, and G. A. Clarke, Eds., American Society for Testing and Materials, Philadelphia, 1979.
[21] Paris, P. C., Gomez, M. P., and Anderson, W. E., "A Rational Analytic Theory of Fatigue," *The Trend in Engineering,* University of Washington, Vol. 13, No. 1, Jan. 1961, p. 9.
[22] Paris, P. C., "Fatigue—An Interdisciplinary Approach," *Proceedings of the 10th Sagamore Conference,* Syracuse University Press, Syracuse, NY, 1964, p. 107.
[23] Anderson, W. E. and James, L. A., "Estimating Cracking Behavior of Metallic Structures," *Journal of the Structural Division, Proceeding of the American Society of Civil Engineers,* Vol. 96, No. ST4, April, 1970, pp. 773–790.
[24] Hudak, S. J., Saxena, A., Bucci, R. J., and Malcolm, R. C., *Development of Standard Methods of Testing and Analyzing Fatigue Crack Growth Rate Data,* Technical Report AFM-TR-78-40, Air Force Materials Laboratory, WPAFB, OH, May 1978.
[25] Forman, R. G., Kearney, V. E., and Engle, R. M., "Numerical Analysis of Crack Propagation in a Cyclic-Loaded Structure," *Journal of Basic Engineering,* Vol. 89D, No. 3, 1967, pp. 459–464.

Robert M. Engle, Jr. [1]

Damage Accumulation Techniques in Damage Tolerance Analysis

REFERENCE: Engle, R. M., Jr., "**Damage Accumulation Techniques in Damage Tolerance Analysis,**" *Damage Tolerance of Metallic Structures: Analysis Methods and Applications, ASTM STP 842*, J. B. Chang and J. L. Rudd, Eds., American Society for Testing and Materials, 1984, pp. 25–35.

ABSTRACT: Damage tolerance analysis requires the capability to assess the damage, usually measured by incremental crack growth, accumulating in a given piece of structure under flight-by-flight spectrum loading. This requirement implies the need to process this damage accumulation over thousands of flights consisting of millions of load cycles. Many models have been developed to analyze the process of damage accumulation under spectrum loading. All these models have been computerized to permit timely cost-effective damage tolerance analyses to be performed.

This paper examines the techniques used to perform the damage accumulation process within these computerized models. Techniques range from simple closed-form numerical integration to sophisticated equivalent damage techniques based on statistical representation of the flight-by-flight spectrum. Recommendations for applications to various types of spectra are offered.

KEY WORDS: crack propagation, damage assessment, numerical integration, life analysis, crack growth analysis, damage tolerance, flight-by-flight loading

With the advent of multi-mission aircraft, life predictions have become much more complex. Flight-by-flight spectra involving hundreds of thousands of load cycles have become the rule rather than the exception for damage tolerance analysis. These load spectra require entirely different approaches for economical analysis than the blocked spectra that were used for design just a few years ago. Some flight-by-flight spectra have become so complex that the most cost-effective manner of analyzing them is an equivalent damage approach where the complex spectrum is replaced by a simpler spectrum that is statistically equivalent and gives the same damage per flight or per flight hour. An example portion of one of these flight-by-flight spectra is given in Fig. 1. This sample load history segment contains 84 peaks and valleys representing 0.30 flight hours. To qualify

[1]Aerospace engineer, Structures Division, Air Force Wright Aeronautical Laboratories, Wright-Patterson Air Force Base, OH 45433.

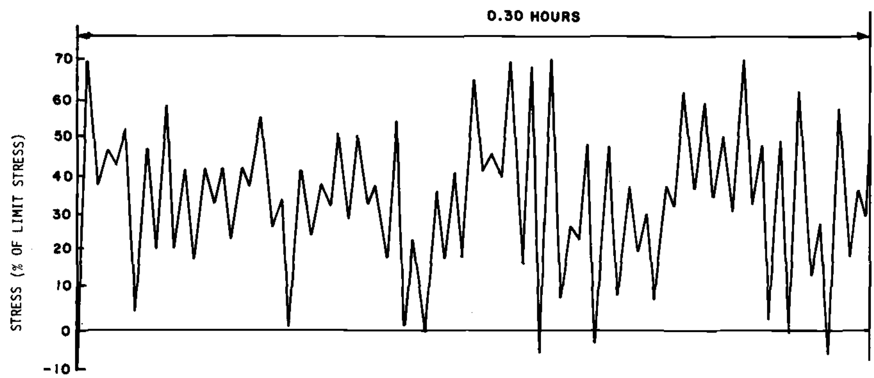

FIG. 1—*Typical 1 flight segment of flight-by-flight spectrum.*

an aircraft for 8000 h (typical for modern fighters) would require analyzing approximately 2.3 million load cycles on a cycle-by-cycle basis. The cost for parametric type studies using such complex spectra would be prohibitive.

Most crack growth analysis computer programs are essentially specialized numerical integration routines, which merely integrate a given crack growth rate relationship (da/dN versus ΔK) through a given load spectrum to obtain the accumulated incremental crack growth per cycle of loading using some type of load interaction (retardation) model. This integration may be on a cycle-by-cycle basis, in which the accumulation technique is a simple summation, or it may be over a large constant amplitude block, in which case some more complex numerical technique might be preferred. The choice of integration, or damage accumulation, technique is often the most significant cost driver in a damage tolerance analysis. In recognition of this fact, much work has been done in the area of damage accumulation for spectrum loading. Several types of integration techniques or schemes will be discussed in the following paragraphs with emphasis on the range of applicability and the accuracy versus cost used as major parameters for comparison. Topics, such as retardation models, cycle counting, and stress intensity factors, are treated elsewhere in this volume.

Cycle-by-Cycle Approaches

Detailed design and failure analyses require the most accurate crack growth analysis possible. This implies a capability to consider the effects of every load cycle on the structure and to consider the interactions of all pertinent damage parameters. While the load interaction modelling is of paramount importance as far as accuracy is concerned, the damage accumulation (integration) scheme often controls the cost and turnaround time. While these analyses are called "cycle-by-cycle," most treat any load level discretely regardless of the number of cycles in the sequence. Many of the techniques will default to direct summation when there is only one cycle in the load level. Several of the more prominent numerical integration techniques are described in the following sections.

Direct Summation

The simplest form of damage accumulation is the direct summation of the damage caused by each cycle, a cycle at a time. This approach is applicable for any combination of load and geometry. Examination of the load history in Fig. 1 makes it obvious that this is the only practical approach to analyzing a load history of this complexity. Since virtually every cycle is unique there is no advantage to be gained by using a sophisticated technique in an attempt to increase the efficiency of the calculations. The damage seen by the structure is quite simply the total of the individual components of damage for each cycle as calculated by the damage model.

The damage accumulation relationship is given by

$$a_f = a_0 + \sum (da/dN)_i$$

Closed Form Integration

For very simple geometries, such as wide center-cracked panels, and simple crack growth rate relationships, such as the Paris equation or the Walker equation, it is often possible to express the damage for a given load level in closed form. The number of cycles to grow a crack of a given size a_0 to a final size a_f under a given load can be obtained by direct integration of the crack growth rate relationship (see Fig. 2). If, as is more often the case, the final crack size for a given number of cycles of a given load is the desired output, the equation for ΔN in Fig. 2 is simply solved for a_f. The damage accumulation relationship then becomes

$$a_f = a_0 + \sum a_{fi}$$

This damage accumulation technique, while very fast, is seldom applicable for realistic geometries since the stress intensity factors for typical structures of interest do not lend themselves to closed-form solution. This method is used in

• CRACK GROWTH RATE EQUATION:

$$\frac{da}{dN} = C\left[(1-R)^m K_{max}\right]^n \quad \text{WHERE} \quad K_{max} = \sigma_{max}\sqrt{\pi a}$$

• APPLY DIRECT INTEGRATION:

$$\Delta N = \int_{a_0}^{a_f} \frac{da}{C\left[(1-R)^m K_{max}\right]^n}$$

$$= \frac{2}{C(2-n)(1-R)^{mn}(\sigma_{max}\sqrt{\pi})}\left(a_f^{\frac{2-n}{2}} - a_0^{\frac{2-n}{2}}\right)$$

FIG. 2—*Closed form integration.*

CRACKS-PD [1] under the assumption that the crack-growth increment is small for each load block. This permits the rate relationship to be factored into a form suitable for closed form integration.

Numerical Integration

Since closed form solutions are not feasible in most cases, numerical integration techniques become necessary. Three such methods that are used in existing crack growth programs are the following:

(1) Runge-Kutta integration,
(2) Taylor series approximation, and
(3) linear approximation.

The Runge-Kutta technique is a numerical method that approximates the integral of the function by evaluating the slopes at four points in the integration interval. These slopes are then combined in a weighted manner (see Fig. 3) to calculate the integral. This requires the evaluation of the crack growth rate da/dN a minimum of four times per load level. Currently used in the CRACKS computer program [2], Runge-Kutta is very accurate. However, it consumes a substantial amount of computer time when used to analyze load histories such as the type shown in Fig. 1. For load histories containing large constant amplitude blocks this technique provides excellent results with minimum computer expenditures.

The Taylor series approximation method used by Johnson in the CGR [3] program is similar in concept to the Runge-Kutta technique described above. Instead of evaluating the slope of the function at selected points, Johnson develops a power series expansion about a_i and performs the numerical integration using this power series. Like Runge-Kutta, this method is very accurate but is time consuming for cycle-by-cycle type load histories.

$$\Delta a = a_{n+1} - a_n = \frac{1}{6}(K_0 + 2K_1 + 2K_2 + K_3)$$

$$\text{WHERE} \quad K_0 = \Delta N \cdot \left.\frac{da}{dn}\right|_{a_n}$$

$$K_1 = \Delta N \cdot \left.\frac{da}{dn}\right|_{a_n + K_0/2}$$

$$K_2 = \Delta N \cdot \left.\frac{da}{dn}\right|_{a_n + K_1/2}$$

$$K_3 = \Delta N \cdot \left.\frac{da}{dn}\right|_{a_n + K_2}$$

FIG. 3—*Runge-Kutta integration technique.*

The linear approximation technique was introduced in the EFFGRO [4] program. Currently in wide use throughout the industry, this method strikes an excellent balance between accuracy and computational efficiency. The basis for the approximation is the assumption that the damage parameters remain constant over some small increment of crack growth Δa. Thus, the damage accumulation process for this increment may be linearized and treated as shown in Fig. 4. This process is repeated for each load level in the stress history. One significant advantage of the linear approximation method is that it considers more cycles at a time whenever the rate of change of crack growth rate is small but considers fewer cycles when the change in crack growth rate is large. The accuracy of the linear approximation method is controlled by the size of a. A study conducted by Chang et al [10] demonstrated that the value of a shown below produced results with an accuracy of the same order as the Runge-Kutta method in the CRACKS program. The results of this study are shown in Table 1 along with the required computer central processing unit (CPU) times for several classes of loading problems. It is obvious from the table that the linear approximation method is superior in all but the block loading cases.

Flight-by-Flight Approaches

Flight-by-flight load histories are very complex in nature. Any given mission can include ground loads, loads resulting from turbulence (gust loads), maneuver

(a) FOR LOAD LEVEL (j) CALCULATE $\left(\frac{da}{dN}\right)_j$

USING $(\sigma_{max})_j$ AND $(\sigma_{min})_j$

(b) COMPARE $\frac{0.01a}{(da/dN)_j}$ TO N_j

IF $\frac{0.01a}{(da/dN)_j} > N_j$, $\Delta a_j = N_j \times \left(\frac{da}{dN}\right)_j$, GO TO (c)

IF $\frac{0.01a}{(da/dN)_j} < N_j$, $\Delta a_j = 0.01a$

$N_j = N_j - \frac{0.01a}{(da/dN)_j}$, $a = 1.01a$

GO TO (a)

(c) $j = j + 1$, GO TO (a)

(d) REPEAT ENTIRE PROCESS FOR EVERY LOAD LEVEL IN EACH BLOCK.

FIG. 4—*Steps in the linear approximation method.*

TABLE 1—*CRACKS (Runge-Kutta) versus CRKGRO (linear approximation).*

CRACKS Prediction Cycles	CRACKS CPU	CRKGRO Prediction Cycles	CRKGRO CPU	CPU (CRACKS)/ CPU (CRKGRO)
		CONSTANT AMPLITUDE		
1 009 500	0.135	1 004 270	0.026	5.2
2 199 750		2 184 830		
1 010 325	1.002	1 001 420	0.068	14.7
150 000		150 000		
11 325	0.018	11 310	0.010	1.8
24 675		24 630		
		SINGLE OVERLOAD		
14 105	0.039	14 105	0.037	1.05
14 105		12 860		
40 015	0.009	42 515	0.007	1.37
12 505		12 505		
35 010	0.024	35 010	0.007	3.45
25 010		25 010		
		BLOCK LOADING		
11 500	0.022	10 885	0.026	0.84
17 620		17 705		
10 485	0.024	10 495	0.025	0.96
23 000		22 135		
74 750	0.031	74 625	0.018	1.74
12 050		10 970		
65 750	0.013	65 625	0.018	0.72
95 750		95 760		
		FLIGHT SPECTRUM		
156 650	2.667	155 290	0.460	5.8
90 070	0.500	90 500	0.227	2.2

loads (air-to-air combat, and so forth), and ground-air-ground loads. Further, the increasing use of multi-mission aircraft compounds these complexities. As a result, crack growth analysis becomes very cumbersome, especially for parametric analyses such as in the early design stages or for individual aircraft tracking. It is highly desirable that some equivalent loading be developed to provide the same rate of damage accumulation to reduce cost and complexity of both tests and analyses. Many investigators have proposed methods for developing equivalent load histories [*5–9*]. Chang et al [*10*] have reviewed several of the more prominent. Three general types will be discussed below. In essence, all of these methods replace the complex load history with an equivalent history, which produces the same damage or rate of damage while greatly simplifying the testing and analysis tasks.

Equivalent Stress Methods

Many investigators have developed equivalent stress methods for crack growth analysis. These methods involve the conversion of the flight-by-flight load history into a constant amplitude load history where a single cycle or group of cycles represents a single flight of the actual load history. Figure 5 depicts this process in a schematic fashion. In this case, the loads in the flight-by-flight spectrum are replaced by an effective stress equal to the root-mean-square (RMS) stress if "b" is set to two. Once the equivalent loads are developed, the solution to the crack growth rate analysis becomes the evaluation of a constant amplitude loading. This particular version of the equivalent stress method was developed for the Air Force by Chang et al [*10*]. Figure 6 shows a comparison of crack growth predictions based on both cycle-by-cycle and equivalent constant amplitude methods with test data from Ref. *10*. While not so accurate as the cycle-by-cycle method the equivalent constant amplitude method has been shown [*11*] to provide adequate accuracy with appreciable cost savings.

Equivalent Damage Methods

While the equivalent stress method operates directly on the flight-by-flight loads to obtain a constant amplitude load, the equivalent damage method uses the crack growth rate relationship as the normalizing parameter to obtain an equivalent load. The damage is calculated for each load level in the stress history, and the crack growth rate equation is then solved to determine the constant amplitude load, which will give the same damage on an average per flight basis. This is the technique used in the CRACKS-PD program [*1*] to obtain the equivalent stress per flight that makes the rapid integration possible. The sequence of operations in the equivalent damage method is as follows.

1. Consider a load history of H flights with a total of N_t cycles.
2. Define the average growth rate per flight as the sum of N_t growth rates divided by H flights.

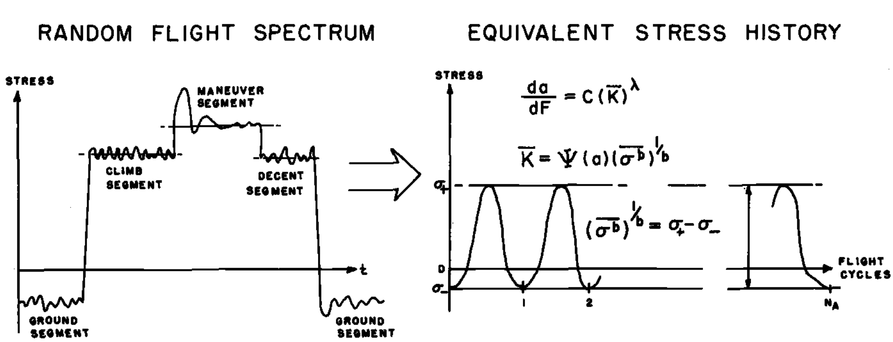

FIG. 5—*Equivalent constant amplitude technique.*

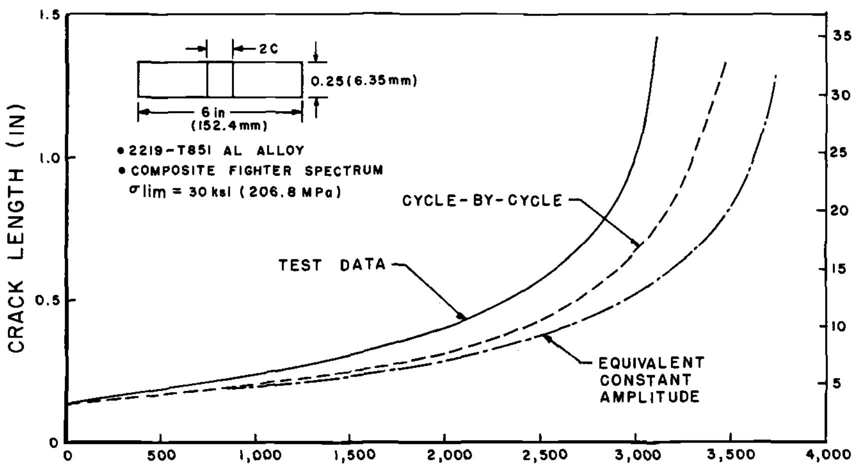

FIG. 6—*Data correlation: equivalent constant amplitude technique.*

3. Assume a crack growth rate relationship.
4. Define the rate per flight in terms of the crack growth rate relationship.
5. Define the equivalent stress in terms of the growth rate parameters.
6. Establish the damage relationship as a function of the equivalent stress.

Growth Rate per Flight Methods

A third technique for reducing the magnitude of the calculations in a spectrum crack growth prediction combines some features of the equivalent constant amplitude approaches described above with standard cycle-by-cycle approaches. Two versions of this method are depicted schematically in Fig. 7. In the first version [*12*] a representative block of flights ΔF is selected for analysis (Fig. 7*a*). Using any standard cycle-by-cycle method a crack growth increment Δa is calculated for each of several initial crack sizes. A characteristic value of ΔK is obtained using an equivalent stress technique as described above. From these analyses then a spectrum crack growth rate curve (da/dF versus ΔK) can be developed and used to make life predictions for parametric studies of this spectrum. This curve applies to any geometry and to any proportional change of all stresses in the given spectrum. However, should another spectrum, material, or environment be of interest, the entire process must be repeated to obtain a second spectrum crack growth rate curve.

In an extension of the above approach, Gallagher [*13*] proposed choosing several ΔF blocks and analyzing each at selected initial crack sizes. Using this technique, the analyst can evaluate not only the growth rate per flight but also the potential scatter in those growth rates (Fig. 7*b*). This method may also be used to determine the appropriate ΔF block for use in the simpler approach of Fig. 7*a*.

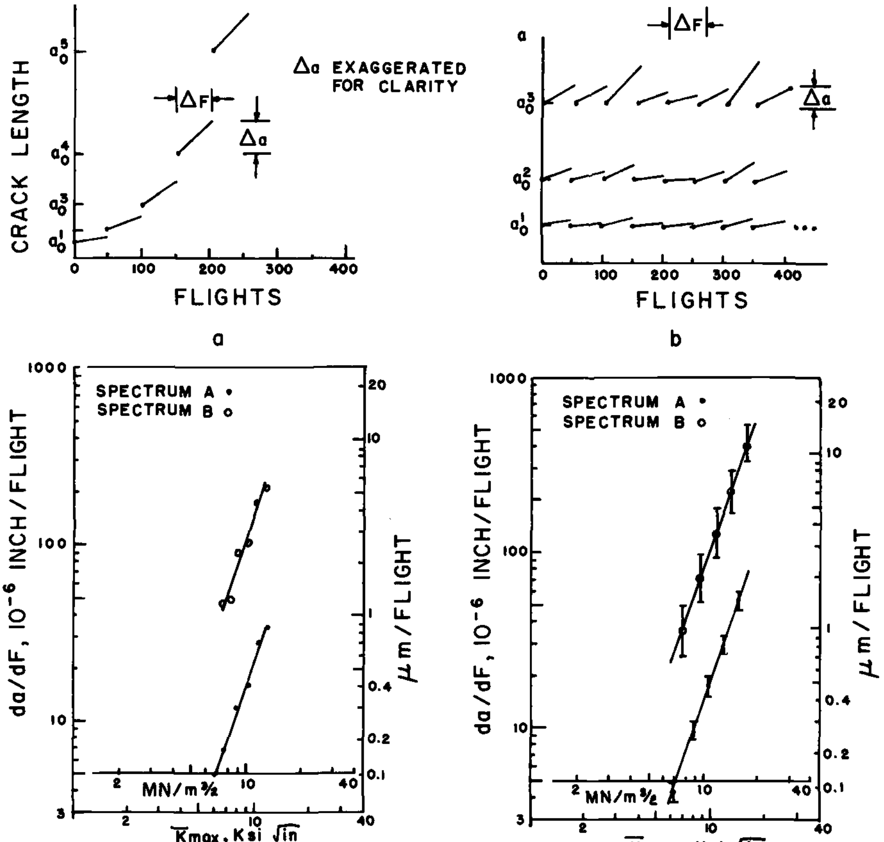

FIG. 7—*Flight-by-flight damage accumulation concepts.*

Table 2 presents a comparison of predictions with test results for both methods. Seven variations of Spectrum A and four of Spectrum B were examined. The life prediction ratio parameter is the ratio of the predicted life to the test life. Test data were obtained from radial corner cracks in 7075-T6511 aluminum panels. In general all predictions were within 20% of the test life. The simple approach of Fig. 7*a* results in a savings of computer time of a factor of five over typical cycle-by-cycle approaches. The statistical method of Fig. 7*b* uses approximately the same time as a cycle-by-cycle approach but provides data for evaluating variabilities in the analysis not otherwise available except at exhorbitant cost.

The most significant limitation of this technique is the accuracy with which the ΔF block can be defined to represent the behavior of the actual spectrum. Gallagher defines a class of spectra, called steady-state spectra, which lends itself to analysis by this method. For spectra that do not exhibit a periodic behavior, much of the computational advantage of these techniques is lost because of the size or number of ΔF blocks required to define the spectrum behavior or both.

TABLE 2—*Life Prediction Ratios* N_p/N_t.

Spectrum Variation	Cycle-by-Cycle Analysis	Flight-by-Flight Analysis	Flight-by-Flight Statistical Analysis
A1	1.27	1.25	1.34
A2	0.98	0.96	0.98
A3	1.09	1.07	1.08
A4	0.84	0.84	0.84
A5	1.17	1.14	1.20
A6	1.09	1.06	1.09
A7	0.83	0.81	0.83
B1	1.09	1.05	1.24
B2	1.08	0.91	1.08
B3	0.94	0.81	0.95
B4	0.96	0.84	0.97

Summary

Selection of a single damage accumulation technique for crack growth analysis is not usually practical or desirable. The choice is driven by several factors:

(1) desired level of accuracy,
(2) available data base,
(3) type of spectra,
(4) importance of retardation effects, and
(5) computer budget.

Numerical integration methods can excel for block loading type spectra but are much less efficient for flight-by-flight loading. The statistically based methods, both equivalent stress and equivalent damage, can be very efficient for spectra that are not dominated by a few very high loads, but retardation effects tend to be washed out in the development of the equivalent constant amplitude load. This disadvantage is overcome to some extent in the flight-by-flight methods since the spectrum da/dF curve already contains the effects of load interactions. However, mission-mix studies are a problem since the required periodic block does not remain fixed, requiring the da/dF curve to be regenerated for some spectrum variations. For general purpose crack growth analysis the linear approximation approach offers the most flexibility of any technique as well as the best overall computational efficiency of the cycle-by-cycle techniques.

References

[1] Engle, R. M., Jr. and Wead, J. A., "CRACKS-PD, A Computer Program for Crack Growth Analysis using the Tektronix 4051 Graphics System," AFFDL-TM-79-63-FBE, Air Force Flight Dynamics Laboratory, Wright-Patterson Air Force Base, OH, June 1979.

[2] Engle, R. M., Jr., "CRACKS, A FORTRAN IV Digital Computer Program for Crack Propagation Analysis," AFFDL-TR-70-107, Air Force Flight Dynamics Laboratory, Wright-Patterson Air Force Base, OH, Oct. 1970.

[3] Johnson, W. S., "CGR, An Improved Computerized Model to Predict Fatigue Crack Growth Under Spectrum Loading," NSRDC Report 4577, Naval Ship Research and Development Center, Bethesda, MD, Jan. 1975.

[4] Szamossi, M., "Crack Propagation Analysis by Vroman's Model, Program EFFGRO," NA-72-94, Rockwell International, Los Angeles, CA, 1972.

[5] Schilling, C. G., Klippstein, K. H., Barsom, J. M., and Blake, G. T., "Fatigue of Welded Steel Bridge Members Under Variable Amplitude Loadings," National Cooperative Highway Research Report 188, Washington, DC, 1978.

[6] Albrecht, P. and Friedland, M., "Fatigue-Limit Effect on Variable Amplitude Fatigue of Stiffeners," *Journal of the Structural Division, Proceedings of the American Society for Civil Engineers,* Vol. 105, No. ST12, Dec. 1979, pp. 2657–2675.

[7] Committee on Fatigue and Fracture Reliability of the Committee on Structural Safety and Reliability of the Structural Division, "Fatigue Reliability: Variable Amplitude Loading," *Journal of the Structural Division, Proceedings of the American Society for Civil Engineers,* Vol. 108, No. ST1, Jan. 1982.

[8] Elber, W., "Equivalent Constant-Amplitude Concept for Crack Growth under Spectrum Loading," *Fatigue Crack Growth Under Spectrum Loads, ASTM STP 595,* American Society for Testing and Materials, Philadelphia, 1976, pp. 236–250.

[9] Barsom, J. M., "Fatigue-Crack Growth Under Variable Amplitude Loading in ASTM A 514B Steel," *Progress in Flaw Growth and Fracture Toughness Testing, ASTM STP 536,* American Society for Testing and Materials, Philadelphia, 1973, pp. 147–167.

[10] Chang, J. B., Stolpestad, J. H., Shinozuka, M., and Vaicaitis, R., "Improved Methods for Predicting Spectrum Loading Effects-Phase I Report, Vol. I: Results and Discussion," AFFDL-TR-79-3036, Vol. I, Air Force Flight Dynamics Laboratory, Wright-Patterson Air Force Base, OH, March 1979.

[11] Chang, J. B., Hiyama, R. M., and Szamossi, M., "Improved Methods for Predicting Spectrum Loading Effects, Vol. I: Technical Summary," AFWAL-TR-81-3092, Vol. I, Flight Dynamics Laboratory, Wright-Patterson Air Force Base, OH, Nov. 1981.

[12] Brussat, T. R., "Rapid Calculation of Fatigue Crack Growth by Integration," *Fracture Toughness and Slow-Stable Cracking, ASTM STP 559,* American Society for Testing and Materials, Philadelphia, 1974, pp. 298–311.

[13] Gallagher, J. P., "Estimating Fatigue-Crack Lives for Aircraft: Techniques," *Experimental Mechanics,* Vol. 16, No. 11, Nov. 1976, pp. 425–433.

Charles R. Saff[1]

Crack Growth Retardation and Acceleration Models

REFERENCE: Saff, C. R., "**Crack Growth Retardation and Acceleration Models,**" *Damage Tolerance of Metallic Structures: Analysis Methods and Application, ASTM STP 842,* J. B. Chang and J. L. Rudd, Eds., American Society for Testing and Materials, 1984, pp. 36–49.

ABSTRACT: In predicting crack growth behavior under arbitrary spectrum loads, one must consider the effects of tensile and compressive overloads to retard and accelerate growth. There are two major categories of crack growth models for prediction of retardation and acceleration behavior: yield zone models and closure models. Capabilities and limitations of these models are discussed with respect to accuracy in predicting various growth behaviors.

Yielding at notches or holes can significantly alter the retardation behavior caused solely by crack-tip plasticity. Careful analysis of notch plasticity is required to predict behavior of flaws growing from notches under spectrum loading.

KEY WORDS: crack propagation, plastic deformation, fatigue (materials), spectrum loads, retardation, mathematical models

Two primary influences on crack growth behavior are retardation following overloads, and acceleration following compressive loads. This behavior is reflected in the results from tests of fighter and transport stress spectra (Fig. 1), wherein the spectrum variations shown to have greatest influence on crack growth life include tensile overloads and, to a lesser extent, compressive overloads [*1*, *2*]. The major difference between fighter and transport aircraft stress spectra is in the ground-air-ground cycle, which occurs once per flight. This cycle produces major loads in transport aircraft but not in maneuverable fighter aircraft. To predict spectrum crack growth behavior requires prediction methodology that accounts for retardation and acceleration.

Numerous models for the effects of retardation and acceleration exist as shown in Fig. 2 [*3–20*]. These models can be divided into two groups, models based on yield zone size alone (yield zone models) and models based on closure caused by

[1]Technical specialist, Structural Research, McDonnell Aircraft Co., McDonnell Douglas Corp., P.O. Box 516, St. Louis, MO 63166.

SPECTRUM VARIATION TYPE	CHANGE IN CRACK GROWTH LIFE FROM LIFE UNDER DESIGN SPECTRUM		
	>50%	<50%	<10%
REORDERING OF LOADS WITHIN A MISSION		O	Δ
SEQUENCE OF MISSIONS		Δ	O
MISSION MIX	O Δ		
FLIGHT LENGTH	O		Δ
OVERLOADS	O Δ		
COMPRESSION LOADS		O Δ	
EXCEEDANCE CURVE VARIATIONS	O Δ		
COUPLING OF PEAKS AND VALLEYS		O Δ	
LIMIT STRESS	O Δ		

O Transport spectra Δ Fighter spectra

FIG. 1—*Effects of spectrum variations on crack growth life.*

YIELD ZONE MODELS	CLOSURE MODELS
WHEELER 1970	ELBER (CONCEPT) 1969
WILLENBORG, ENGLE, WOOD 1971	BELL (GENERALIZED CLOSURE) 1974
	NEWMAN (FINITE ELEMENT) 1974
VROMAN 1971	DILL AND SAFF (CONTACT STRESS) 1975
PORTER 1971	KANNINEN, FEDDERSON, ATKINSON (SUPER-DISLOCATION) 1975
GRAY (GENERALIZED WHEELER) 1973	
GALLAGHER AND HUGHES (GENERALIZED WILLENBORG) 1974	ELBER (MODEL) ....1976 PARIS 1976
JOHNSON 1981	BUDIANSKY AND HUTCHINSON 1976
CHANG ET. AL 1981	DE KONING 1980

FIG. 2—*Crack growth models.*

crack surface deformations that occur within the yield zone (closure models). Yield zone models were developed earliest, although the closure concept was presented by Elber [*9*] about the time these models were being formulated (Fig. 2). This probably occurred because the closure concept is more difficult to model.

In this paper, the Wheeler and Willenborg models are examined as representative of the yield zone concept, its capabilities and limitations. These models became familiar to the aircraft industry through their incorporation in the CRACKS routines for crack propagation analysis [*21*]. The contact stress model is presented to demonstrate the capabilities of a closure model.

In addition to retardation and acceleration resulting from crack-tip plasticity, yielding at a notch or hole from which the crack grows is often an important factor in crack growth behavior. The interaction of notch plasticity and crack-tip plasticity is a complex nonlinear phenomenon that can sometimes change the relative severity of load spectra and must be considered for accurate crack growth prediction. The limitations of current analysis techniques are discussed and an engineering approach to solution of crack growth from yielded holes is presented.

Yield Zone Model

Wheeler Model

The Wheeler model [*3*] is a yield zone model that predicts retardation by reducing the crack growth rate through analysis of the plastic zone created by an overload (Fig. 3). The amount of retardation depends on the ratio of current crack-tip plasticity to previous plasticity. If the current plastic zone extends beyond the length of the prior plastic zone, no retardation is predicted. Generally, the exponent m is an empirically determined adjustment to the retardation found in the test.

At the McDonnell Aircraft Co. (MCAIR), we have used the Wheeler model to fit hundreds of spectrum crack growth test results. We have developed techniques that allow us to make a reasonable estimate for the retardation exponent m given the maximum spectrum stress and the flaw shape parameter Q [*22*], as shown in Fig. 4. The relationship of m to $f_{max}/\sqrt{Q}$ varies with material and is generally lower for cyclically softening materials, like 6Al-4V titanium and 4340 steel (Fig. 5).

The refined model can accurately predict crack growth behavior for a wide variety of spectra (Fig. 6), but many spectrum tests are required in any material to determine the retardation factor m. In addition, as currently formulated, the model does not predict acceleration caused by compressive loads.

Willenborg Model

Some of these drawbacks are overcome by the Willenborg model [*4, 8*]. This model is based on yield zone analyses, but in this case retardation is accounted

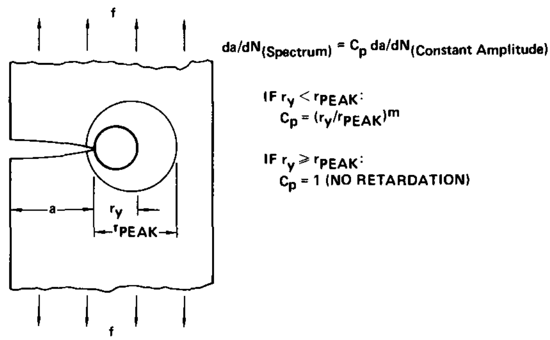

FIG. 3—*Wheeler model.*

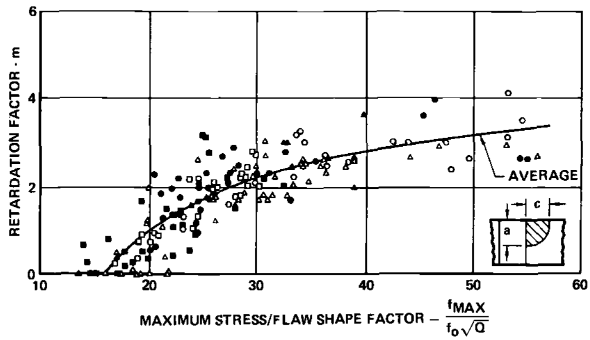

$Q \approx 1 + 1.47\,(a/c)^{1.64}$
f_o = 1 ksi = 6.89 MPa

FIG. 4—*Relationship of retardation factor to stress level.*

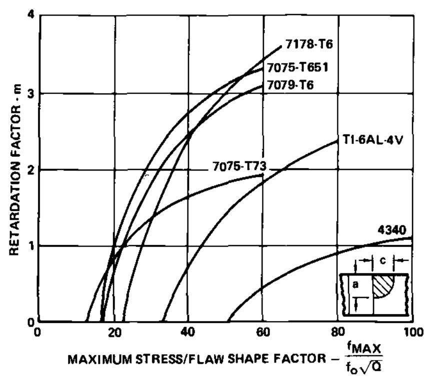

$Q \approx 1 + 1.47\,(a/c)^{1.64}$
f_o = 1 ksi = 6.89 MPa

FIG. 5—*Variation of retardation factor with material.*

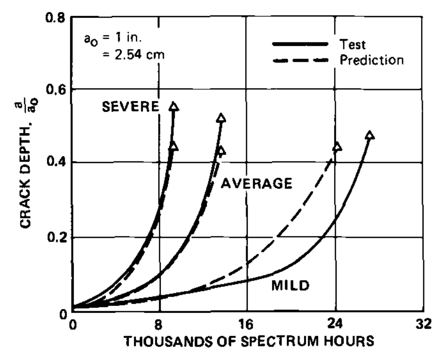

FIG. 6—*Comparison of crack growth prediction and test for three variations of a wing skin spectrum.*

for by a reduction in stress intensity factor and by truncating the minimum effective stress intensity factor at zero (Fig. 7).

One drawback of the original Willenborg model [4] was that whenever the peak stress for any overload exceeded other peak stresses by more than a factor of two, no further crack growth would be predicted to occur. Gallagher and Hughes [8] introduced a parameter to allow adjustment of the peak stress ratio at which crack growth shutoff would occur (Fig. 8). Overloads tests are used to determine the overload ratio required to shut off crack growth.

As originally formulated, the Willenborg model could not predict acceleration due to compressive loads [23]. One method for accommodating the effects of compressive loads is to alter the computation of the plastic zone size to reduce zone sizes when compressive loads occur. Although developed from analyses of simple load spectra, this altered model predicts the effects of compression on crack growth life under complex spectra (Fig. 9).

In the program, "Effect of Fighter Attack Spectrum on Crack Growth," [1, 24] this version of the Willenborg model was used to predict crack growth lives for

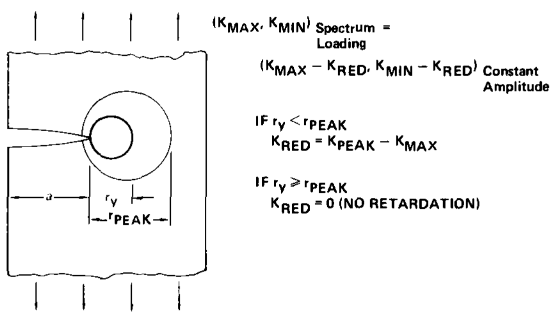

FIG. 7—*Willenborg model.*

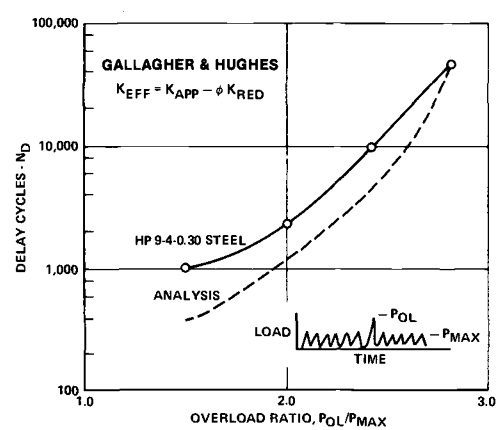

FIG. 8—*Gallagher and Hughes revision of Willenborg model to predict growth when overload ratio exceeds two.*

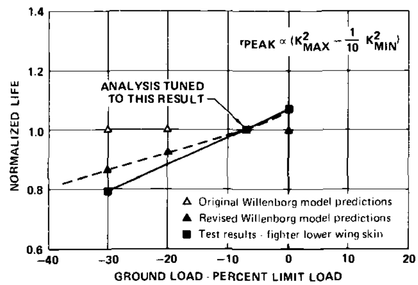

FIG. 9—*Adjustment of Willenborg model allows prediction of compressive load effects.*

27 different load spectra. It was shown to predict crack growth lives within 50% of the test data in 22 of the 27 cases (Fig. 10).

This model still suffers from a fault common to all yield zone models; because it is based solely on the relationship of current plasticity to previous plastic zone sizes, it cannot predict differences in retardation caused by single and multiple overloads (Fig. 11).

Closure Models

Contact Stress Model

The contact stress model [*12, 13*] was developed primarily because of the deficiencies in yield zone models and the amount of testing required for analysis of new materials.

The model is based on the crack closure concept originated by Elber [*9*]. Thus, it is based on the assumption that crack growth is controlled not only by the behavior of the plastic zone but by residual deformations left in the wake of the crack as it grows through previously deformed material (Fig. 12).

In the contact stress model, Dugdale-like analyses of the plastic zone are used to compute the plastic deformation ahead of the growing crack. These defor-

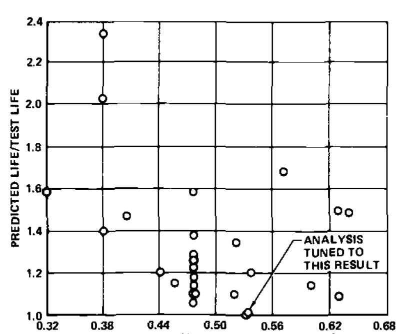

FIG. 10—*Comparison of Willenborg model analyses with spectrum test results.*

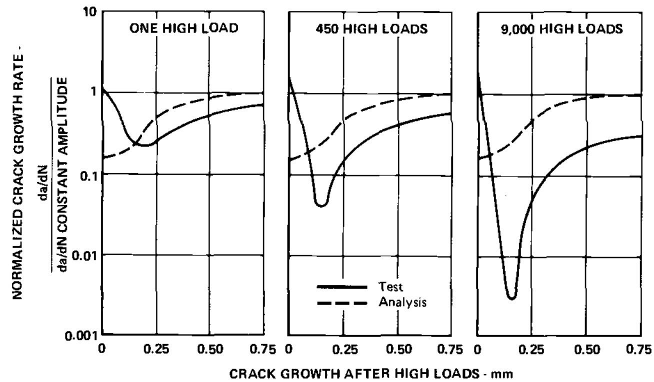

FIG. 11—*Comparison of Wheeler model predictions with overload test data of Trebules et al* [25].

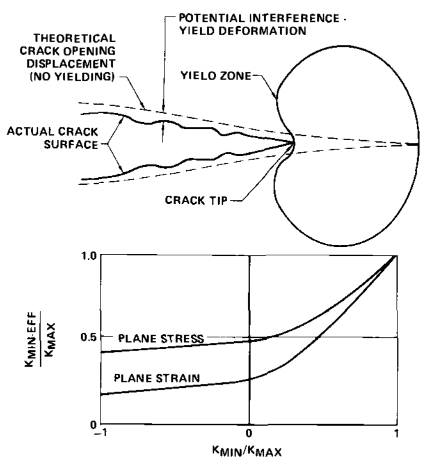

FIG. 12—*Contact stress model.*

mations are treated as a wedge of material separating the faces of the extended crack. Analyses of this wedge, both ahead of and behind the crack tip, are used to define the deformations occurring at the crack tip. These deformations are assumed to control crack growth behavior during any given load cycle.

Deformations computed at minimum load are left in the wake of the crack as permanent residual deformations. These residual deformations left in the wake of the growing crack preserve a history of prior loading and provide the basis for the model to predict crack growth behavior for a wide variety of load spectra without empirical adjustment.

To help visualize how the model works, consider the single overload case shown in Fig. 13. Before the overload, the crack is loaded cyclically at constant ΔK, leaving a constant residual deformation in the wake. At the time of the overload considerable additional deformation occurs, forming a large concen-

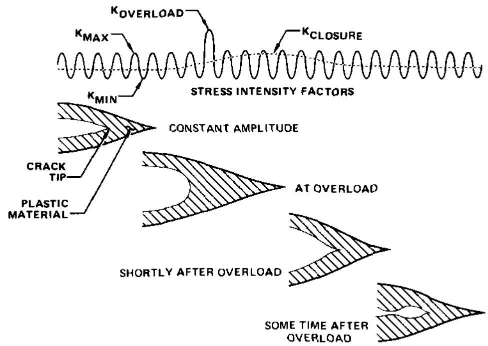

FIG. 13—*Crack growth behavior following a single overload.*

tration of plastic deformation just ahead of the crack tip. Shortly after the overload, as the crack progresses into the region of large residual deformations, the change in crack-tip deformations becomes considerably reduced, causing retardation. As the crack continues to grow through and beyond the large residual deformations, these deformations influence crack-tip behavior less, and constant amplitude behavior is gradually recovered.

Comparison of contact stress model analyses and the multiple overloads data from Trebules et al [25] shows that this model can accurately correlate crack growth behavior following both single and multiple overloads (Fig. 14).

The model requires no stress ratio adjustments because the crack-tip deformations change with applied stress ratio and can be used to predict these effects accurately (Fig. 15). In addition, the model can predict the effects of additional overloads in a periodic spectrum, as shown by comparison of predictions with the test data from Schivje et al [26] in Fig. 15.

Because residual deformations are reduced when compressive loads are applied, the model predicts the effect of compressive loads to reduce retardation

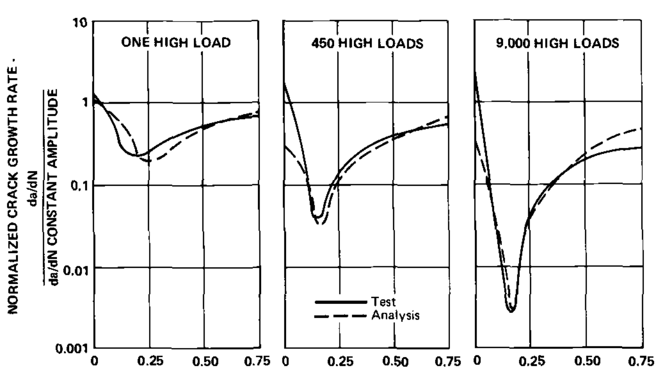

FIG. 14—*Comparison of contact stress model predictions with overload test data of Trebules et al* [25].

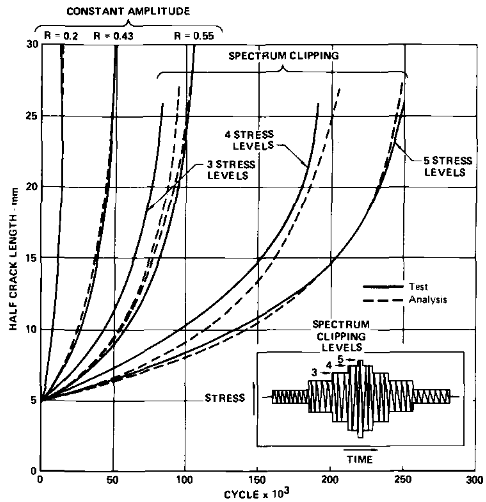

FIG. 15—*Comparison of contact stress model analyses with test data of Schivje et al* [26].

following overloads (Fig. 16). The effect of compression on constant amplitude crack growth is not nearly as great as on the spectra with overloads [*13*, *27*].

The contact stress model was used to compute crack growth for each of the 27 spectrum crack growth tests of Ref *1*. The contact stress model predictions are shown in Fig. 17 to be within 25% of the test results.

The comparison of yield zone and closure models shown in Fig. 18 indicates the ability of closure models to analytically predict many more characteristics of spectrum crack growth than yield zone models, although yield zone models have been empirically enhanced recently by the work of Johnson [*19*] and Chang [*20*]. Because closure models are complex they must be simplified before they can be used to predict spectrum crack growth lives efficiently and routinely. The contact

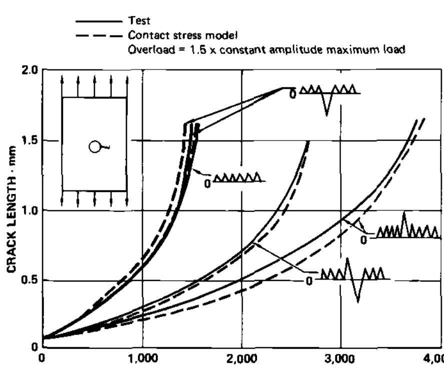

FIG. 16—*Comparison of contact stress model analysis and test results from Hsu and Lassiter* [27].

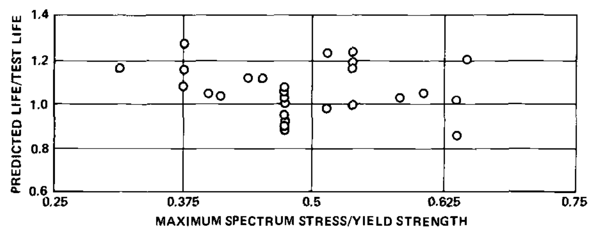

FIG. 17—*Comparison of contact stress model analyses with spectrum test data.*

CAPABILITY	YIELD ZONE MODELS	CLOSURE MODELS
RETARDATION FOLLOWING HIGH LOADS	√	√
EFFECTS OF STRESS RATIO		√
INCREASED RETARDATION FOLLOWING MULTIPLE HIGH LOADS		√
EFFECTS OF COMPRESSION LOADS		√
DELAYED RETARDATION		√
ACCELERATION DURING HIGH LOADS		√

FIG. 18—*Comparison of crack growth model capabilities.*

stress model has been simplified for routine analysis and has become the primary crack growth prediction methodology used at MCAIR [*28*].

Both yield zone and closure models are currently based on analyses of long, central through cracks. However, yielding at fastener holes, or other notches, plays an important role in crack growth retardation as well.

Effects of Notch Plasticity on Retardation

Current analyses of cracks growing from holes or notches assume that the only effect of plasticity at a hole is to modify the stress intensity factors experienced by the flaw. Crack-tip plastic zone sizes and displacements computed for very small flaws are often smaller than the plastic stress field around the hole (Fig. 19). More rigorous analyses show that the effect of the flaw is to extend the plastic zone slightly from the hole. These analyses also show that the crack surface displacements and growth behaviors are almost entirely controlled by plastic stresses and strains at the hole rather than by crack-tip plasticity as is often assumed.

Sometimes the current approach to notch plasticity can result in incorrect prediction of spectrum crack growth behavior. Consider the three fighter wing skin spectra shown in Fig. 20. In most cases, we would expect the air-to-air spectrum to be most severe and the air-to-ground spectrum to be least severe. This is true for center cracked panels, as shown by the data of Chang et al [*5*] (Fig. 21).

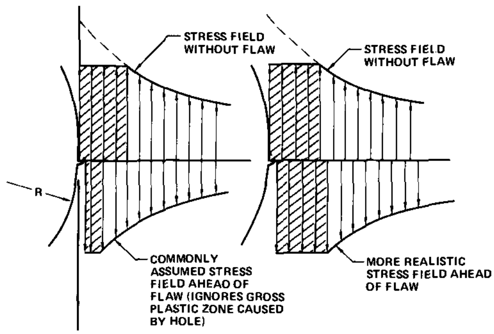

FIG. 19—*Comparison of two differing analyses of crack-tip plasticity for a crack from a hole.*

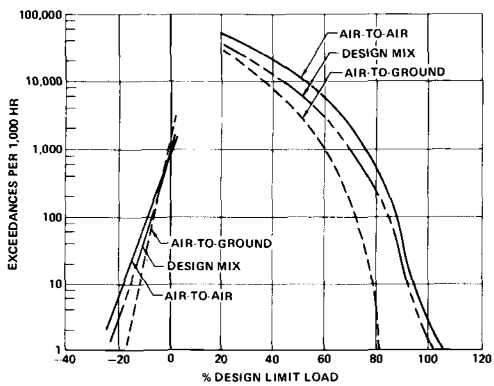

FIG. 20—*Comparison of fighter lower wing skin spectra.*

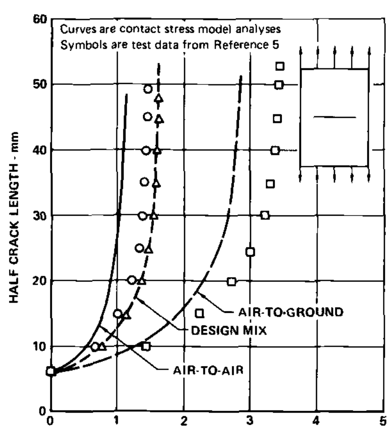

FIG. 21—*Comparison of crack growth behavior in center-cracked panels under three fighter wing skin spectra.*

However, for through cracks at holes (initial depths of 0.45 mm) the severities of the spectra are significantly reordered (Fig. 22). In this case, the air-to-ground spectrum is most severe and the design mix spectrum is least severe.

Crack growth analyses using common assumptions of hole and crack-tip plasticity will not predict the actual behavior (Fig. 23). In this case, the predicted growth for the air-to-ground spectrum is close to the measured growth for the air-to-air spectrum. Using a more complete analysis of hole and crack-tip plasticity, we were able to correlate the results of both center-cracked panel and open-hole panel tests (Figs. 21 and 22).

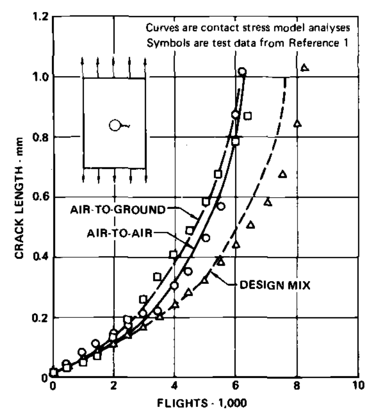

FIG. 22—*Comparison of crack growth behavior at open holes under three fighter wing skin spectra.*

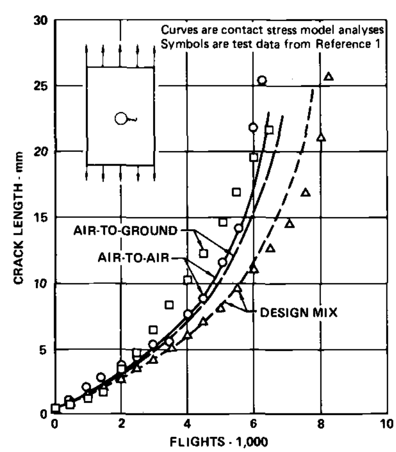

FIG. 23—*Comparison of typical flaw growth from hole analyses with test results.*

Summary

In predicting crack growth under spectrum loads, one must consider both retardation and acceleration, modeling capabilities and limitations, and the effects of residual stress fields. High loads have been shown to be most influential in the life of flawed components, often retarding the crack growth significantly. Large compressive loads have a secondary influence that reduces the retardation afforded by overloads. These effects must be considered in predicting crack growth lives.

Crack closure models offer the potential to analytically predict many more characteristics than yield zone models. While closure models are mathematically more complicated than yield zone models, they can be simplified for routine analysis.

The effects of yielding at notches on crack growth can sometimes reverse the retardation behavior predicted by analysis, or found by test of center-cracked panels. Careful analysis of notch plasticity is required to predict accurately the behavior of flaws growing from notches under spectrum loading.

References

[1] Dill, H. D. and Saff, C. R., "Effect of Fighter Attack Spectrum on Crack Growth," AFFDL-TR-76-112, Air Force Flight Dynamics Laboratory, Wright-Patterson Air Force Base, OH, March 1977.

[2] Abelkis, P. R., "Effect of Transport/Bomber Loads Spectrum on Crack Growth," AFFDL-TR-78-134, Air Force Flight Dynamics Laboratory, Wright-Patterson Air Force Base, OH, Nov. 1978.

[3] Wheeler, O. E., "Spectrum Loading and Crack Growth," *American Society for Mechanical Engineers Transactions, Journal of Basic Engineering,* Vol. 94, March 1972, pp. 181–186.

[4] Willenborg, J., Engle, R. M., and Wood, H. A., "A Crack Growth Retardation Model Using an Effective Stress Concept," AFFDL-TR-71-1, Air Force Flight Dynamics Laboratory, Wright-Patterson Air Force Base, OH, Jan. 1971.

[5] Chang, J. B., Stolpestad, J. H., Shinozuka, M., and Vaicaitis, R., "Improved Methods for Predicting Spectrum Loading Effects—Phase I Report," AFFDL-TR-79-3036, Vol. 1, Air Force Flight Dynamics Laboratory, Wright-Patterson Air Force Base, OH, March 1978.

[6] Porter, T. R., "Method of Analysis and Prediction of Variable Amplitude Fatigue Crack Growth," *Engineering Fracture Mechanics,* Vol. 4, No. 4, Dec. 1972, pp. 717–736.

[7] Gray, T. D. and Gallagher, J. P., "Predicting Fatigue Crack Retardation Following a Single Overload Using a Modified Wheeler Model," *Mechanics of Crack Growth, ASTM STP 590,* American Society of Testing and Materials, Philadelphia, 1976.

[8] Gallagher, J. P. and Hughes, T. F., "Influence of Yield Strength on Overload Affected Fatigue Crack Growth Behavior in 4340 Steel," AFFDL-TR-74-27, Air Force Flight Dynamics Laboratory, Wright-Patterson Air Force Base, OH, July 1974.

[9] Elber, W., "The Significance of Fatigue Crack Closure," *Damage Tolerance In Aircraft Structures, ASTM STP 486,* American Society for Testing and Materials, Philadelphia, 1971, pp. 230–242.

[10] Bell, P. D. and Creager, M., "Crack Growth Analyses for Arbitrary Spectrum Loading," AFFDL-TR-74-129, Air Force Flight Dynamics Laboratory, Wright-Patterson Air Force Base, OH, 1974.

[11] Newman, J. C., "A Finite Element Analysis of Fatigue Crack Closure," NASA TM X-72005, National Aeronautics and Space Administration, Hampton, VA, 1975.

[12] Dill, H. D. and Saff, C. R., "Spectrum Crack Growth Prediction Method Based on Crack Surface Displacement and Contact Analyses," *Fatigue Crack Growth Under Spectrum Loads, ASTM STP 595,* American Society for Testing and Materials, Philadelphia, 1976, pp. 306–319.

[13] Dill, H. D. and Saff, C. R., "Analysis of Crack Growth Following Compressive High Loads Based on Crack Surface Displacement and Contact Stress Analyses," *Cyclic Stress-Strain and Plastic Deformation Aspects of Fatigue Crack Growth, ASTM STP 637,* American Society for Testing and Materials, Philadelphia, 1977, pp. 141–152.

[14] Kanninen, M. F., Atkinson, C., and Feddersen, C. E., "A Fatigue Crack Growth Analysis Method Based on a Simple Representation of Crack-Tip Plasticity," *Cyclic Stress-Strain and Plastic Deformation Aspects of Fatigue Crack Growth, ASTM STP 637,* American Society for Testing and Materials, Philadelphia, 1977, pp. 122–140.

[15] Elber, Wolf, "Equivalent Constant-Amplitude Concept for Crack Growth Under Spectrum Loading," *Fatigue Crack Growth Under Spectrum Loads, ASTM STP 595,* American Society for Testing and Materials, Philadelphia, 1976, pp. 236–250.

[16] Paris, P. C., "Measurements and Analytical Models for Crack Closure in Fatigue," presented at Washington University, St. Louis, MO, 1976.

[17] Budiansky, B. and Hutchinson, J. W., "Analysis of Closure in Fatigue Crack Growth," *Journal of Applied Mechanics,* Vol. 45, No. 2, June 1978, pp. 267–276.

[18] DeKoning, A. U., "A Simple Crack Closure Model for Prediction of Fatigue Crack Growth Rates Under Variable Amplitude Loading," NLF MP-80006U, National Aerospace Laboratory NLR, Amsterdam, Netherlands, Jan. 1980.

[19] Johnson, W. S., "Multi-Parameter Yield Zone Model for Predicting Spectrum Crack Growth," *Methods and Models for Predicting Fatigue Crack Growth Under Random Loading, ASTM STP 748,* American Society for Testing and Materials, Philadelphia, 1981, pp. 85–102.

[20] Chang, J. B., Hiyama, R. M., and Szamossi, M., "Improved Methods for Predicting Spectrum Loading Effects," AFWAL-TR-81-3092, Air Force Flight Dynamics Laboratory, Wright-Patterson Air Force Base, OH, Vol. I, 1981.

[21] Engle, R. M., "CRACKS, A Fortran IV Digital Computer Program for Crack Propagation Analysis," AFFDL-TR-70-107, Air Force Flight Dynamics Laboratory, Wright-Patterson Air Force Base, OH, 1970.

[22] Pinckert, R. E., "Damage Tolerance Assessment of F-4 Aircraft,"Paper 76-904, American Institute for Aeronautics and Astronautics, New York, Sept. 1974.

[23] Wood, H. A., "The Use of Fracture Mechanics Principles in the Design and Analysis of Damage Tolerant Aircraft Structures," *Fatigue Life Prediction for Aircraft Structures and Materials,* AGARD-LS-62, Amsterdam, Netherlands, 1973, pp. 4.1–4.3.

[24] Dill, H. D., Saff, C. R., and Potter, J. M., "Effects of Fighter Attack Spectrum on Crack Growth," *Effect of Load Spectrum Variables on Fatigue Crack Initiation and Propagation, ASTM STP 714,* American Society for Testing and Materials, Philadelphia, 1980, pp. 205–217.

[25] Trebules, V. W., Roberts, R., and Hertzberg, R. W., *Progress in Flaw Growth and Fracture Toughness Testing, ASTM STP 536,* American Society for Testing and Materials, Philadelphia, 1973, pp. 115–146.

[26] Schivje, J., Broek, D., and de Rijk, P., "Fatigue Crack Propagation Under Variable Amplitude Loading," NLR TN-M 2094, National Aerospace Laboratory, Amsterdam, Netherlands, Dec. 1961.

[27] Hsu, T. M. and Lassiter, L. W., "Effects of Compressive Overloads on Fatigue Crack Growth," American Institute for Aeronautics and Astronautics, Paper No. 74-365, New York, AIAA/ASME/SAE Structures, Structural Dynamics and Materials Conference, Las Vegas, NV, April 1974.

[28] Pinckert, R. E. and Scheidter, R. A., "Improved Fatigue Life Tracking Procedures for Navy Aircraft Structures — Phase II Final Report," NADC-77194-60, Naval Air Development Center, Warminster, PA, Nov. 1981.

James B. Chang[1]

ASTM Fatigue Life Round-Robin Predictions

REFERENCE: Chang, J. B., "**ASTM Fatigue Crack Life Round-Robin Predictions,**" *Damage Tolerance of Metallic Structures: Analysis Methods and Applications, ASTM STP 842*, J. B. Chang and J. L. Rudd, Eds., American Society for Testing and Materials, 1984, pp. 50–68.

ABSTRACT: A series of round-robin predictions of fatigue crack life have been conducted since 1976 by ASTM Task Group E24.06.01 on Application of Fracture Data to Life Prediction. The primary objective of these round-robin exercises was to investigate (1) if the compact type (CT) specimen constant-amplitude fatigue-crack-growth-rate data could be used to predict the growth behavior and lives of part-through crack (PTC) specimens under constant amplitude loading, and (2) if center-crack-tension (CCT) specimen constant-amplitude fatigue-crack-growth-rate data could be used to predict the growth behavior and lives of CCT specimens subjected to variable amplitude and random spectrum loadings. Five sets of round-robin predictions were conducted on a total of 57 specimens that were made of three materials: 2219-T851 aluminum, 6Al-4V titanium, and 9Ni-4Co-0.2C steel. This paper summarizes the results of these round-robin analytical predictions and their correlations to test data.

KEY WORDS: fatigue (materials), cracking, fatigue life, compact type specimen, center crack tension specimen, part-through crack specimen, constant amplitude fatigue crack growth rate data, variable amplitude loading, random spectrum loading, 2219-T851 aluminum, 6Al-4V titanium, 9Ni-4Co-0.2C steel, round-robin analysis

Nomenclature

c_i	Initial half crack length
c_f	Final half crack length
c_{cr}	Critical half crack length
K	Stress intensity factor
K_c	Fracture toughness of the material
N_{pred}	Number of cycles obtained from the analytical prediction
N_{test}	Number of cycles applied to the specimen
R	Ratio of minimum stress to maximum stress in a cycle
da/dN	Fatigue crack growth rate

[1]Engineering specialist, The Aerospace Corporation, Los Angeles, CA 90009; formerly, Rockwell International Corporation, North American Aircraft Operations, Los Angeles, CA 90009.

ΔK Stress intensity factor range
σ_{max} Maximum cyclic stress

Introduction

The implementation of the fracture control plan on structures, such as aircraft, spacecraft, and pressure vessels, subjected to repeated (cyclic) loadings requires the capability for accurate predictions of the growth behavior of cracks or crack-like flaws contained in the primary structural components under service loadings. To perform analytical life predictions on structures containing cracks, the common practice in the industry is to use a crack-growth analysis computer code such as CRACKS [*1*], EFFGRO [*2*], and CGR-GD [*3*]. Most computer codes are based on the linear elastic fracture mechanics (LEFM) concept and use a damage accumulation package that interrelates the following items:

(1) cyclic loading descriptions, including the maximum and minimum loads (stresses) of each cycle and the number of cycles;
(2) crack configurations, sizes, locations, and configurations of the cracked body;
(3) crack-tip stress-intensity-factor equations;
(4) load interaction model accounting for retardation and acceleration effects to crack growth;
(5) material's constant amplitude crack-growth-rate data, fracture data, and other material properties corresponding to the service environment; and
(6) numerical integration procedure.

Among these items, data used in item number five (5), including da/dN and K_c, are directly related to the activity of ASTM Committee E24 on Fracture Testing. A tentative test method has been established by ASTM Subcommittee E24.04, on Subcritical Crack Growth, namely, ASTM Test for Constant-Load-Amplitude Fatigue Crack Growth Rates Above 10^{-8} m/Cycle (E 647). Compact type (CT) and center-cracked-tension (CCT) specimens are the two standard specimens recommended in ASTM Standard E 647 for generating the constant amplitude crack-growth-rate data. However, the usual type of problem in damage tolerance analyses is to predict the life of surface flaws and edge corner cracks at holes, and so forth, contained in structures subjected to spectrum loadings in accordance with Military Specification Airplane Damage Tolerance Requirements (Mil-A-83444). Questions often raised by analysts were: (1) Can CT specimen constant-amplitude fatigue-crack-growth-rate data be used to predict the crack growth behavior of part-through cracks (PTC) under constant amplitude loading? and (2) Can CT or CCT specimen constant-amplitude fatigue-crack-growth-rate data be used to predict the crack growth behavior and lives of any type of crack contained in structures subjected to variable amplitude loadings? These loadings include single or multiple overloads/underloads, block loadings, flight-by-flight spectrum loadings, and random spectrum loadings.

To seek for the answers to the above listed two key questions, a series of round-robin analyses have been performed within the membership of ASTM Task Group E-24.06.01 on Application of Fracture Data to Life Prediction. The primary mission of this task group is to determine if fracture mechanics data generated from ASTM standard test methods can be used to predict fatigue-crack-growth behavior and lives of structures containing cracks or cracklike flaws. This task group is further charged with making recommendations for additional testing if the need becomes apparent. This task group also provides the members of ASTM Committee E-24 with the opportunity to evaluate their in-house capability for predicting fatigue crack growth. Table 1 summarizes the past round-robin prediction activities conducted by Task Group E24.06.01 from 1976 until 1981. As can be seen from the table, the primary test material was 2219-T851 aluminum alloy. This was because of the availability of the crack growth data. Available fatigue-crack-growth-data of other materials were also included in the round-robin analyses.

All the round-robin predictions were conducted by providing the participants with the test and specimen descriptions including cyclic loading types and conditions, maximum/minimum stress levels, environmental conditions, specimen dimensions, initial crack sizes, the material baseline (constant-amplitude) crack-growth-rate data, and the fracture toughness data. All the fracture mechanics data were generated in accordance with the ASTM recommended specimens (CT and CCT specimens). Without knowing the test results, each participant was asked to predict the crack-growth behavior or lives of the cracked specimens or both. After the analytical predictions were performed and results were submitted to Task Group E24.06.01, experimental test results were then furnished to each participant for the evaluation of their prediction capability and for refinement on their methodology. This paper describes the data furnished to each participant of each round-robin exercise and summarizes the results of the round-robin predictions.

TABLE 1—*Summary of past round-robin exercises conducted by ASTM Task Group E24.06.01.*

Year Conducted	Load and Specimen Type	Material	Data Furnished to Participant	Requested Predictions, number of cycles to
1976	constant amplitude surface flaw	2219-T851 aluminum 6-4 titanium	CT da/dN data CT K_{Ic} and K_c data	breakthrough failure
1977	constant amplitude surface flaw	2219-T851 aluminum	CT da/dN data CT K_{Ic} and K_c data	breakthrough failure
1978	constant amplitude surface flaw	9-4-20 steel	CT da/dN data CT K_{Ic} and K_c data	breakthrough failure
1979	variable amplitude CCT	2219-T851 aluminum	CCT da/dN data CCT K_c data	failure
1980	random spectrum CCT	2219-T851 aluminum	CCT da/dN data CCT K_c data	failure

Surface Flaw Specimens

Three sets of round-robin predictions were performed by participating members of ASTM Committee E24, from 1975 through 1977. All the round-robin prediction cases conducted in this series were the coupon type of specimens. These specimens contained surface flaws exposed to various types of environmental conditions and subjected to constant amplitude loadings at various stress levels, stress ratios, and loading frequencies. Three materials were covered in this series of round-robin analysis exercises. They were 2219-T851 aluminum, 6Al-4V titanium, and 9Ni-4Co-0.2C steel. Selected baseline constant amplitude fatigue-crack-growth-rate (da/dN) data and fracture toughness data for these three materials were furnished to each participant of the round-robin predictions. The da/dN data were generated from CT specimens by following the test procedure and data reduction technique developed as part of an aircraft system fracture mechanics material data generation program [*4*]. These procedures and reduction techniques met the subsequent requirements of ASTM E 647 without significant deviations.

Figures 1 through 3 are the typical examples of the constant amplitude CT specimen da/dN data furnished to each participant for these round-robin exercises. The solid lines in these figures are the computer generated curves representing a mean-fit to the test data under a specific test/environment condition. For example, data points shown in Fig. 3 were obtained from a test, with a HP 9Ni-4Co-0.2C steel CT specimen, tested in a low-humidity air (LHA) environment, at room temperature, under constant amplitude load cycles with a stress ratio of $R = 0.08$, and a loading rate of 6 Hz. The da/dN data for 2219-T851 aluminum, 6Al-4V titanium, and 9Ni-4Co-0.02C steel in other environments including distilled water (DW) and sump-tank water (STW) conditions and at other loading rates and stress ratios were also included in the data package furnished to each participant.

In all the round-robin prediction exercises, each participant was provided with data sheets, which contained the specimen descriptions and test load conditions as well as the test environment conditions of each test case. However, test results were not provided. A typical data sheet is shown in Fig. 4. The analytical exercise was to predict the number of loading cycles for a given size of surface flaw to grow through the thickness of the specimen (breakthrough), or to grow to its critical size (failure) or both. The specimen parameters and the test load/environment parameters of all test cases predicted in these three round-robin exercises are summarized in Tables 2 through 4. In all of these tables, the test results and the calculated prediction ratios N_{pred}/N_{test} of each test case are also included. Notice that when the prediction ratio is unity, that is, $N_{pred}/N_{test} = 1.000$, the prediction is perfect. Any prediction ratio greater than 1.000 indicates that the fatigue crack growth life of the specimen was overestimated (so-called unconservative prediction). On the other hand, any prediction ratio less than 1.000 is conservative in the sense that the analysis predicts less life than the

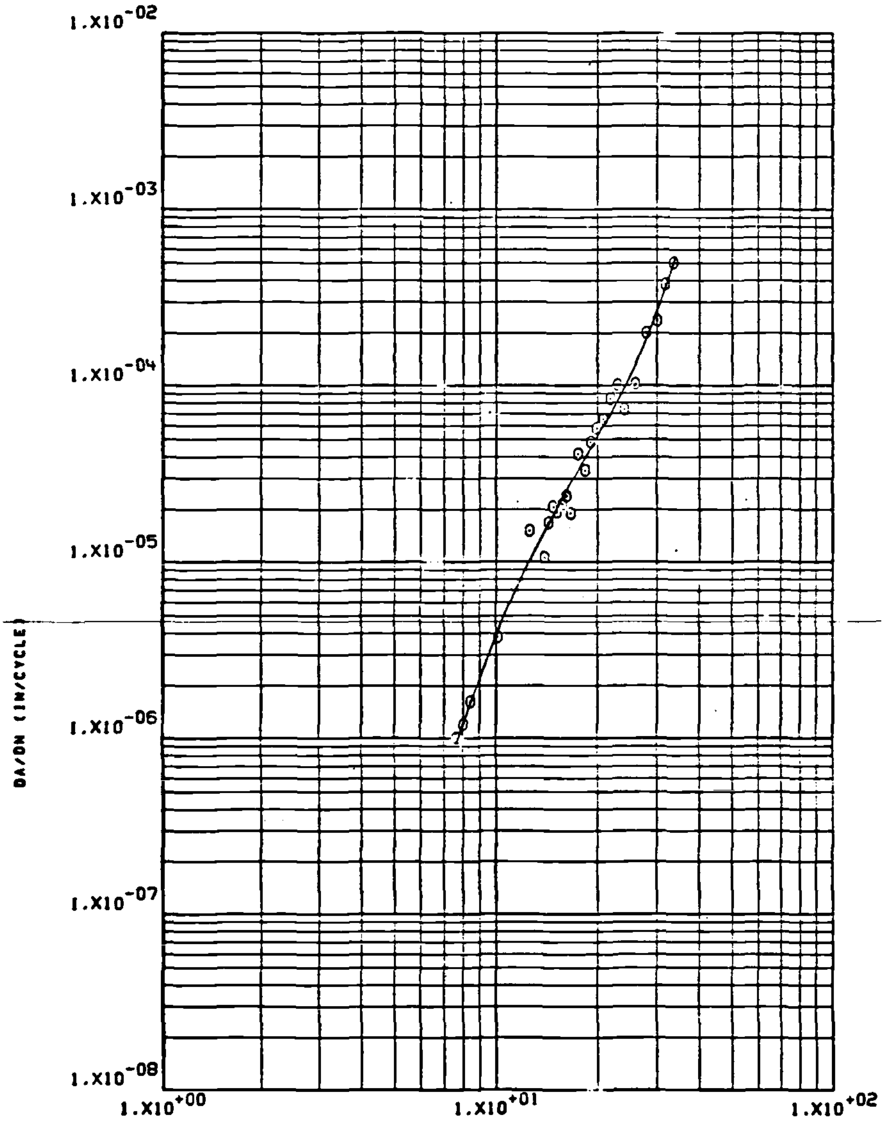

FIG. 1—*Fatigue crack growth of the 2219-T851 aluminum alloy.*

specimen experienced in the test. The mean and standard deviation of the prediction ratio for each test case has also been calculated and presented in these tables.

The correlation results of these three round-robin exercises have been discussed by Vroman [5], so it will not be repeated here. Overall results of these

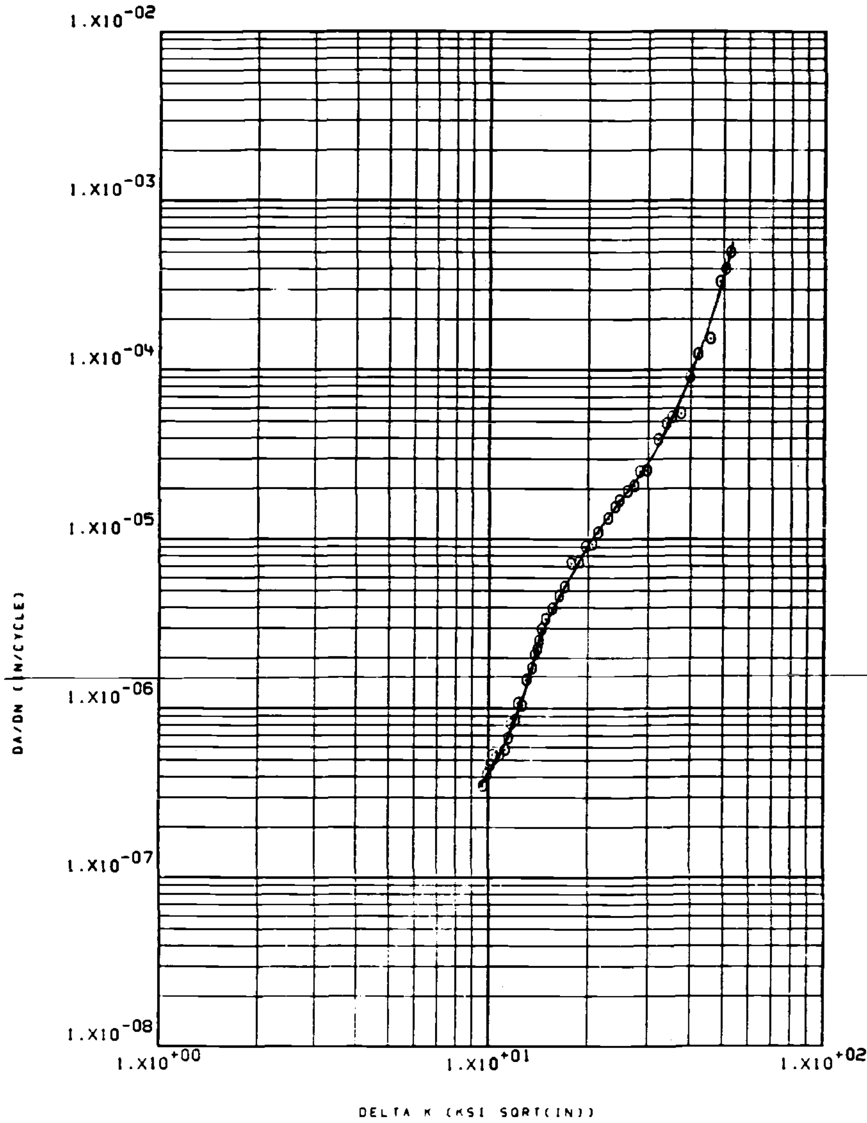

FIG. 2—*Fatigue-crack-growth data of the 6-4 titanium alloy at recrystallized annealed condition.*

three sets of analytical exercises have been summarized by Vroman in Ref *5*. From these round-robin prediction results, the E24.06.01 Task Group concluded that fatigue crack lives of PTC specimens (such as coupons containing surface flaws) under constant amplitude loading can be predicted with sufficient accuracy using the crack-growth-rate data obtained from the CT specimens.

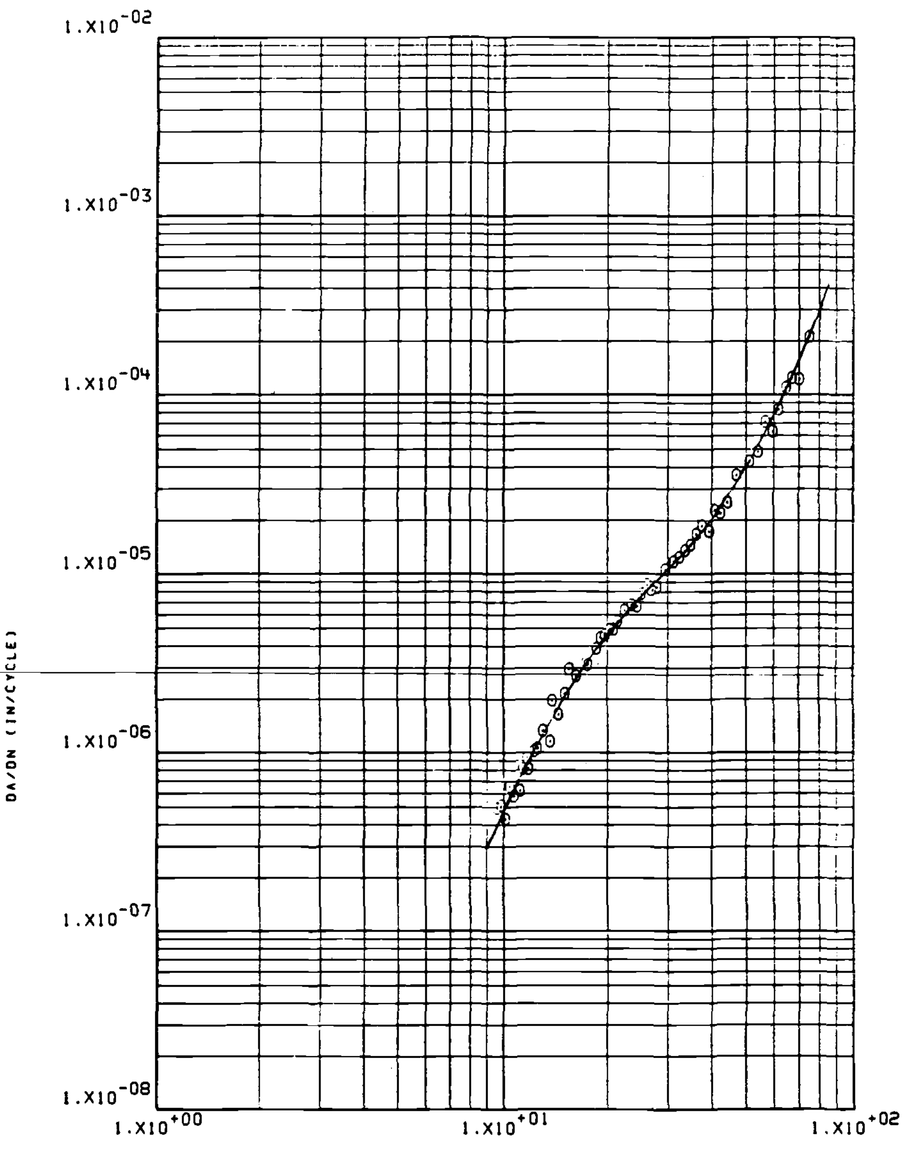

FIG. 3—*Fatigue-crack-growth data of HP 9-4-20 steel.*

Enclosure (2) to ltr dtd 10 Nov 76 Page 1 of 10 Pages

PART-THROUGH-CRACK SPECIMEN

Specimen No. 23-18

Test No. 441

Material: 2219-T851

Environment: Dry Air (LHA)

Cyclic Loading Rate: 60 CPM

Range Ratio: +.05

Constant Amplitude Maximum Stress: 32 KSI

Specimen Test Section Dimensions
Thickness: 0.500 in.
Width: 4.00 in.

Initial Crack Size
Depth (a): 0.060 in.
Aspect Ratio (a/2c): 1/2

Analytical Predictions
"a" @ N = 5,000:
"a" @ N = 10,000:
"a" @ N = 15,000:
Cycles to Breakthrough:
Surface Length at Breakthrough:
Cycles to Failure:
Surface Length at Failure:

FIG. 4—*Sample data sheet used in the ASTM round-robin exercise.*

CCT Specimens Under Variable Amplitude Loadings

In 1979, the E24.06.01 Task Group initiated a new series of round-robin prediction exercises. The purpose was to determine if CCT specimen constant amplitude crack-growth-rate data could be used to predict fatigue crack growth of CCT specimens subjected to variable amplitude loadings. The experimental data base used in this set of round-robin analyses was obtained from a research program conducted by the author at Rockwell International, North American Aircraft Division, for the U.S. Air Force [*6*]. The objective of this research effort was to upgrade the crack-growth analysis technology required for the implementation of the damage tolerance control procedures for any aircraft system. One of the primary tasks performed in this research program was to develop an improved fatigue-crack-growth-life prediction methodology used for assessing the damage tolerant ability of aircraft structures.

TABLE 2—*First surface flaw round-robin exercise results.*[a]

Specimen Number	Specimen Parameters[b]	Test Parameters[c]	Test Lives, cycles	Prediction Radio[d]
23-18	2219-T851 aluminum	32, LHA	24 600	0.754 ± 0.196
23-17	2219-T851 aluminum	14, STW	192 000	1.444 ± 0.193
40-8	6Al-4V-Ti titanium	84, LHA	6 784	0.670 ± 0.247
40-2	6Al-4V-Ti titanium	36, LHA	172 200	1.095 ± 0.527

[a]1 in. = 25.4 mm and 1 ksi = 6.8948 MPa.
[b]All specimens 0.50 in. thick, initial crack size 0.060 in. deep by 0.120 in. surface length ($a/2c$ = ½).
[c]Stress in ksi, LHA = low humidity air, and STW = sump-tank water. All specimens cycled at 0.05 stress range ratio and 60-cpm frequency.
[d]Mean and standard deviation from four analysts.

TABLE 3—*Second surface flaw round-robin exercise results.*

Specimen Number	Specimen Parameters[a]	Test Parameters[b]	Test Lives, cycles	Prediction Ratio[c]
23-18	typical	32, LHA	24 632	0.692 ± 0.148
37-3	...[d]	32, LHA	20 089	0.988 ± 0.288
32-2	...[d,e]	32, LHA	19 868	0.454 ± 0.099
23-16	typical	14, DW	205 000	1.388 ± 0.295
23-12	typical	32, DW	23 000	0.747 ± 0.127
23-13	typical	32, DW[f]	20 000	0.880 ± 0.158
23-17	typical	14, STW	192 000	2.186 ± 1.390
27-76	typical	14, STW[f]	168 000	1.982 ± 1.027
23-14	typical	32, STW	20 400	0.841 ± 0.149
23-10	typical	32, STW[f]	19 367	0.900 ± 0.177

[a]All material 2219-T851 aluminum.
[b]Constant amplitude stress in ksi, LHA = low humidity air, DW = distilled water, STW = sump-tank water, stress range ratio = +0.05 for all specimens, and 1 ksi = 6.8948 MPa.
[c]Mean and standard deviation from six analysts.
[d]Thickness is 1.00 in., all others are 0.50 in., 1 in. = 25.4 mm.
[e]Initial crack is 0.090 in. deep ($a/2c$ = ⅓), all others are 0.060 in. deep ($a/2c$ = ½).
[f]Cyclic loading frequency = 6 cpm, and all others = 60 cpm.

Variable amplitude loading tests were conducted in the above mentioned research program as part of an experimental effort in order to aid in the formulation of the fatigue-crack-life prediction methodology. This experimental program consisted of (1) baseline (constant-amplitude) crack growth rates and fracture toughness data generation tests, (2) constant amplitude tests with various stress levels, (3) single overload/underload or periodic overload/underload tests, (4) multiple overload/underload tests, and (5) random spectrum load tests. All specimens tested in this experimental program were the ASTM standard CCT specimens (ASTM E 647) fabricated from 6.35-mm (0.25-in.) thick 2219-T851 aluminum plates. All plates were from the same lot of material. The CCT specimen was 15.24 cm (6 in.) wide and 45.72 cm (18 in.) long, with a 6.35-mm (0.25-in.) long center notch that was fabricated by using the electrical discharge

TABLE 4—*Third surface flaw round-robin exercise results.*

Specimen Number	Specimen Parameters[a]	Test Parameters[b]	Test Lives, cycles	Prediction Ratio[c]
188	typical	32, LHA	362 410	0.548 ± 0.286
184	typical	54, LHA	66 272	0.798 ± 0.271
583	. . .[d]	54, LHA	78 231	0.796 ± 0.245
189	typical	54, LHA[g]	105 000	0.828 ± 0.342
190	. . .[e]	54, LHA[h]	201 352	0.690 ± 0.337
186	[f]	54, LHA	52 211	0.775 ± 0.233
482	typical	54, STW[i]	47 869	1.085 ± 0.371
484	typical	54, STW	58 559	0.887 ± 0.304
185	typical	126, LHA	7 054	0.829 ± 0.212
191	. . .[f]	126, LHA	6 477	0.642 ± 0.251
483	typical	126, STW[i]	5 038	1.068 ± 0.272
486	typical	126, STW	6 134	0.877 ± 0.224

[a]All material 9Ni-4Co-0.20C steel.
[b]Initial crack aspect ratio $a/2C$ is ⅓, all others are ½.
[c]Mean and standard deviation from five analysts.
[d]Thickness is 1.00 in., all others are 0.50 in., 1 in. = 25.4 mm.
[e]Initial crack is 0.060 in.
[f]Initial crack aspect ratio $a/2C$ is ⅓, all others are ½.
[g]Stress range ratio = +0.3.
[h]Stress range ratio = +0.5; all other stress ratios = 0.
[i]Cyclic loading frequency = 6 cpm; all others = 60 cpm.

machining (EDM) process. The maximum width of the EDM notch was less than 0.245 mm (0.01 in.) under constant amplitude loading. Precracking was done with a 55.16-MPa (8-ksi) maximum stress at a 0.01 stress ratio. All tests were run at a cyclic rate of 6 Hz in an ambient laboratory air environment at room temperature. Cyclic crack-growth measurements were taken visually. The resolution of the crack length measurement was approximately 0.13 mm (0.005 in.).

Twenty test cases were selected for this set of round-robin prediction exercises. Again, each participant was provided with the baseline fatigue-crack-growth-rate and fracture toughness data of the material (2219-T851 aluminum) together with the test load description of each of the 20 test cases. Figure 5 shows the baseline crack-growth-rate data that consists of six sets of data points obtained from specimens tested under constant amplitude loadings at four stress ratios, R = 0.01, 0.1, 0.3, and 0.7. The maximum stress was kept at 138 MPa (20 ksi) in these tests. The da/dN versus ΔK chart was plotted by an interactive graphics computer program, PLOTRATE, developed by Chang et al at Rockwell [7]. It uses the seven-point polynomial method as recommended by ASTM E 647 to determine da/dN from the crack size versus elapsed cycles (a versus n) data set. Values of ΔK were calculated using the ASTM standard formula for CCT specimens. The fracture toughness value for the 6.35-mm (0.25-in.) thick 2219-T851 aluminum plate was determined from the static fracture tests employing the CCT specimens. The average fracture toughness was K_c = 70.85 MPa (m)$^{1/2}$ (65 ksi [in.]$^{1/2}$).

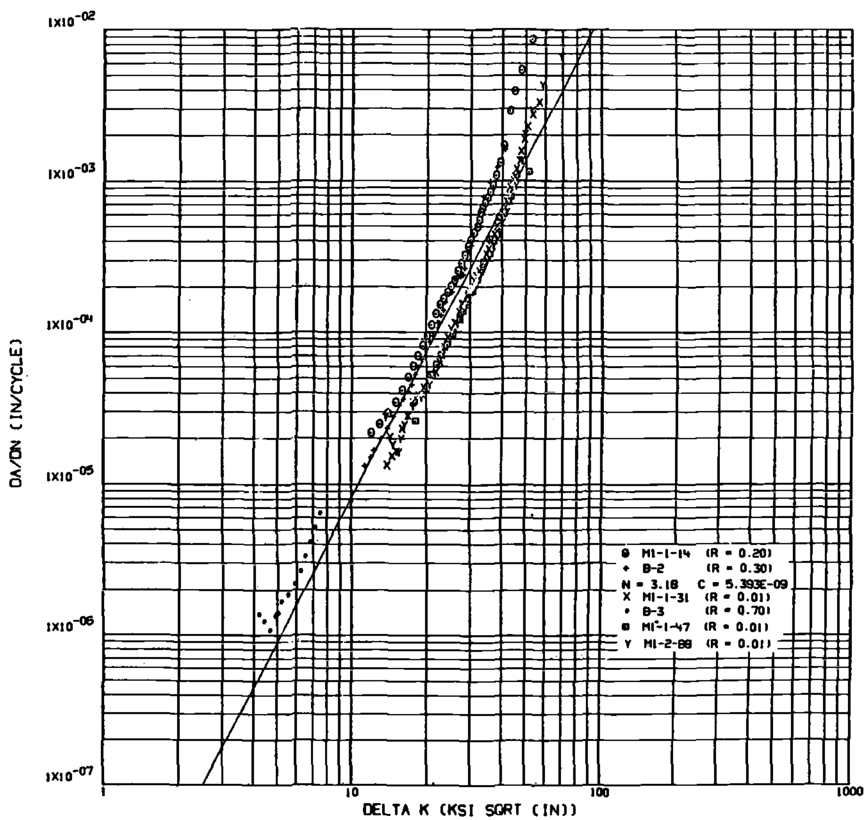

FIG. 5—*Fatigue-crack-growth data of the 2219-T851 aluminum at various stress ratios.*

The loading profiles of the 20 test cases selected by the author for this round-robin exercise are shown in Fig. 6. These tests were conducted with the intention of investigating the load-interaction effects to the fatigue crack growth, which includes primarily (1) single- or multiple-overload retardation, (2) compressive-load acceleration, and (3) reducing of overload retardation by compressive loads. The test parameters of each of these 20 test cases are also presented in Fig. 6. The test-life column in Fig. 6 shows the number of cycles for a center-through crack to grow from an initial size (half crack length c_i) to its critical size c_{cr}.

Six sets of analytical predictions were received by the ASTM E24.06.01 Task Group. Results of the round-robin analytical crack life predictions are also summarized in Fig. 6. The number of cycles required to grow a crack from a given initial crack size to the failure was predicted in each test case. In order to assess the analysis accuracy, prediction ratios N_{pred}/N_{test} were calculated by the author for all of the analytical predictions. Again, for any prediction, if the prediction ratio is smaller than 1.0, it is considered to be a conservative prediction. On the

Test No.	Test Parameters	Test Life cyc.	Prediction Ratio A	B	C	D	E	F	Average
M-13	0/20, 0/45 2,500, 2,500	49,600	0.66	2.5+	5.97	0.91	0.48	0.24	–
M-16	0/20, -6/20 2,500, 2,500	11,370	1.12	1.13	1.2	1.1	1.19	1.07	1.14 ± 0.051
M-20	0/20, -6/30 2,500, 2,500	36,083	0.37	0.55	0.46	1.26	0.36	0.34	0.56 ± 0.35
M-23	0/20, -6/30 2,500, 2,500	11,200	0.77	1.14	0.97	2.65	0.76	0.71	1.17 ± 0.74
M-24	-6/20, -6/30 2,500, 2,500	10,950	0.59	1.14	0.98	0.65	0.67	0.77	0.80 ± 0.22
M-26	-24/8, -16/8 2,500, Fail	269,840	1.0	1.44	1.23	1.67	0.93	0.91	1.20 ± 0.31
M-27	-24/8, -16/8 2,500, 2,500	194,723	1.18	1.5	1.36	1.68	1.03	1.03	1.30 ± 0.26
M-28	-6/20, -15/30 2,500, 2,500	10,003	0.6	1.0	0.97	0.63	0.67	0.78	0.78 ± 0.17
M-29	-6/20, -15/40 2,500, 2,500	15,005	0.6	2.5+	8.12	1.34	0.69	0.77	–
M-30	-6/20, -15/40 2,500, 2,500	20,007	0.5	2.5+	7.03	1.13	0.63	0.63	–
M-31	0/8, 0/20 10,000, Fail	22,430	0.92	0.94	0.95	0.92	0.94	0.88	0.93 ± 0.03
M-35	0/8, 14/20 10,000, Fail	178,838	1.1	1.08	1.23	1.13	1.32	0.66	1.09 ± 0.23
M-37	-24/8, 0/20 10,000, Fail	24,200	0.91	0.95	0.93	0.89	0.91	0.86	0.91 ± 0.03
M-44	0/40, 0/20 500, Fail	50,470	0.15	0.58	0.34	0.006	0.42	0.14	–
M-45	9/30, 6/20 3,370, Fail	23,624	0.76	0.77	0.19	8.16	0.7	0.64	1.87 ± 3.09
M-46	12/40, 6/20 500, Fail	133,260	0.21	0.38	0.08	∞	0.59	0.14	–
M-54	6/20, 6/40 500, 50	9,316	1.47	1.65	0.89	0.59	1.23	0.88	1.12 ± 0.40
M-56	0/20, 0/40 -12/0 2,500, 50, 50	18,130	0.57	0.57	0.51	0.57	1.23	0.56	0.67 ± 0.28
M-57	0/20, -12/0 0/40 2,500, 50, 50	20,760	0.62	2.04	1.75	0.62	1.37	0.45	1.14 ± 0.67
M-58	-6/20, -6/40 2,500, 500	2,774	1.6	2.07	2.09	0.94	2.0	1.80	1.75 ± 0.44

FIG. 6—*Variable amplitude loading round-robin exercise results.*

other hand, for any case if the prediction ratio is greater than 1.0, the prediction is unconservative.

It can be seen from Fig. 6, crack growth lives of many tests cases predicted by the six participants exhibited a wide range of results. This is particularly true for test cases such as M-13, M-29, M-30, M-44, M-45, and M-46. Order of magnitude differences in predictions were shown in these cases. Upon close examination, it was found that all these tests contained high stress level single- or multiple-overload cycles (σ_{max} = 276 MPa or 40 ksi). Severe retardation on crack growth was caused by the high tensile overload cycles in these tests. Accurate predictions rely on the ability of the analytical methodology used in the prediction to account for the retardation effects to the crack growth. Since only the constant amplitude crack-growth-rate data of the 2219-T851 aluminum were furnished to the participant of this round-robin exercise, the fact that the round-robin life predictions showed a large variation is not surprising. From this set of round-robin exercises, the following conclusions were drawn.

1. To predict crack growth behavior under variable amplitude loadings, test data other than constant amplitude crack growth rates are needed.
2. Analytical methods used by a majority of the participants were not capable of providing accurate predictions on these 20 test cases selected for the round-robin exercise.

CCT Specimens Under Random Spectrum Loadings

After the completion of the preceding round robin, it was suggested by the membership of ASTM Committee E24 that a round-robin prediction using random spectrum test data should be conducted. This was suggested because the random spectrum is the typical type of loading that many structures experience in service, including airframe structures, bridges, offshore drilling platforms, and so forth. Further, this type of loading produces all of the crack-growth retardation and acceleration effects that cracks experience when propagating in a structure. Thus, in 1980, the ASTM Task Group E24.06.01 initiated this round-robin exercise. The experimental data base used in this round-robin analysis was again that generated from the aforementioned U.S. Air Force sponsored research program conducted by the author at Rockwell [*6*].

Crack-growth data were collected from random load tests conducted using the following load spectra: air-to-air (A-A); air-to-ground (A-G); instrumentation and navigation (I-N); and composite missions of a typical fighter aircraft and the composite mission of a transport aircraft. These random load spectra data were furnished to each participant in tabular form. Table 5 is a typical load spectrum table. It is the fighter composite mission. Numerical values in this table are the minimum and maximum stresses for each cycle. These values are in the form of percentage of the design limit stress (DLS). Three levels of DLS were tested: DLS = 138, 207, and 276 MPa (20, 30, and 40 ksi). The fighter composite unit block was constructed in the following form

$$11(\text{A-A})_{1-11} + 11(\text{A-G})_{1-11} + 3(\text{I-N})_{1-3}$$
$$+ 11(\text{A-A})_{12-22} + 11(\text{A-G})_{12-22} + 3(\text{I-N})_{4-6}$$

where $11(\text{A-A})_{1-11}$ designates eleven flights of the A-A mission taken from the first flight to the eleventh flight of the A-A baseline mission.

The complete set of the A-A, A-G, and I-N baseline mission tables have been documented by Chang in Ref *8*. This reference also includes a brief description

TABLE 5—*Sample random load spectrum of a typical fighter composite mission.*

0001	C....RANDOM COMPOSITE (N = 1055)									
0002	−05.0*	70.0	16.1	54.1	20.1	45.5	25.0	52.3	36.0	58.7
0003	28.2	44.5	18.6	48.6	24.5	81.9	8.6	29.4	17.8	52.4
0004	17.5	29.5	10.2	79.9	18.8	50.6	32.5	53.7	17.3	65.7
0005	50.6	63.5	3.1	67.5	10.9	60.6	44.0	54.9	16.2	45.1
0006	14.7	34.0	20.4	58.4	31.2	45.6	27.8	63.5	9.4	69.7
0007	36.1	58.2	−5.0	79.4	27.6	42.9	27.9	41.0	9.4	33.5
0008	16.0	40.2	5.2	39.1	19.5	51.9	9.3	31.4	19.1	48.6
0009	0.4	27.6	16.9	36.2	11.8	28.7	9.3	33.2	1.8	13.2
0010	1.4	50.2	18.6	31.8	19.1	48.8	34.0	63.7	29.9	86.8
0011	22.5	42.7	12.2	40.8	22.0	41.9	21.2	42.2	16.3	26.6
0012	−3.6	27.3	11.9	45.3	−5.0	48.8	14.7	48.6	23.6	57.2
0013	36.4	58.3	32.7	48.7	27.1	41.5	29.7	81.1	29.3	60.7
0014	19.8	43.5	28.5	74.9	19.2	48.5	22.4	38.3	5.1	52.8
0015	34.0	45.0	14.7	46.4	3.0	34.8	19.8	48.7	33.4	54.2
0016	25.4	38.7	18.3	36.0	18.5	63.7	17.7	56.1	11.7	29.3
0017	−7.5	41.4	15.3	33.8	9.7	36.1	−5.0	61.7	16.3	50.9
0018	30.1	47.9	25.4	52.1	24.9	65.2	−10.3	50.7	12.6	44.6
0019	32.1	47.0	24.3	38.4	19.6	46.2	23.4	42.3	3.5	52.9
0020	35.8	64.4	16.9	30.6	19.1	47.2	6.4	74.1	12.2	50.2
0021	28.8	45.6	12.7	46.2	15.3	39.2	20.2	46.4	36.3	58.6
0022	3.8	60.0	11.9	44.6	29.5	41.3	11.5	40.4	−5.0	47.4
0023	6.9	44.3	32.4	58.2	16.3	55.1	−4.6	83.3	0.6	37.5
0024	24.1	57.7	16.2	34.8	22.2	65.7	24.8	47.5	13.4	55.9
0025	42.5	64.5	24.9	38.5	−22.0	61.8	36.2	66.4	39.4	60.9
0026	35.4	56.8	25.5	51.2	34.5	54.9	26.8	39.5	−3.7	81.0
0027	−1.8	47.0	12.5	59.6	8.3	53.9	7.7	45.3	29.7	66.4
0028	−5.0	49.2	5.5	33.5	15.0	36.1	2.7	58.5	2.8	40.9
0029	13.8	38.1	13.2	51.7	4.0	33.3	9.4	29.3	11.6	68.5
0030	19.0	45.4	30.9	45.9	13.5	48.1	21.1	57.3	13.9	35.2
0031	18.7	37.3	19.3	40.6	1.1	25.6	8.3	67.1	32.8	71.0
0032	21.5	51.4	12.5	42.8	11.3	41.4	22.8	47.5	17.9	48.9
0033	17.5	55.1	−5.0	41.4	12.2	79.3	15.1	50.4	28.7	45.8
0034	34.3	59.1	28.3	45.5	29.1	52.9	12.0	65.1	30.9	48.0
0035	9.2	66.8	47.6	61.6	15.0	31.1	14.3	50.6	7.7	53.2
0036	39.7	68.1	6.8	20.5	6.2	56.5	9.3	75.7	12.6	52.7
0037	31.3	55.7	17.4	57.7	22.3	61.7	29.0	51.7	39.8	55.5
0038	12.2	42.6	8.1	25.8	−5.0	60.0	13.5	56.0	14.8	63.7
0039	21.6	32.8	20.3	43.4	9.7	48.1	33.5	45.2	−7.3	47.1
0040	8.4	77.9	45.9	58.8	10.3	71.8	10.6	38.2	23.3	46.2
0041	−9.8	40.3	4.9	41.1	17.9	42.7	5.1	41.8	27.2	58.7
0042	29.8	42.9	13.3	46.0	1.2	26.5	−4.5	51.3	5.4	26.6
0043	15.4	38.3	8.6	39.0	5.3	60.3	−5.0	42.2	13.0	34.4
0044	15.8	55.6	12.7	40.8	23.6	49.4	36.7	53.9	25.7	41.0
0045	18.2	33.3	22.5	46.5	3.0	44.7	6.4	39.8	22.5	64.3
0046	24.5	57.0	26.3	53.4	9.8	33.3	0.9	46.4	0.3	48.9
0047	24.5	47.4	22.3	47.2	6.3	77.9	25.9	74.7	18.7	64.1
0048	22.7	58.6	4.7	72.1	7.6	72.3	17.5	53.0	−5.0	59.3
0049	15.0	42.4	27.8	41.6	17.3	70.0	12.9	47.5	25.4	66.3
0050	50.3	89.9	−0.2	69.5	47.1	60.2	13.1	66.1	11.6	71.4
0051	18.7	53.3	18.2	35.5	10.7	42.3	5.6	61.4	23.5	49.3
0052	19.1	51.0	1.3	45.7	15.9	32.5	20.9	43.4	28.9	47.3
0053	22.5	46.1	21.8	52.4	36.4	61.3	8.7	57.5	38.5	54.9
0054	−5.0	39.9	28.4	50.2	8.9	31.0	13.8	55.9	42.8	75.9
0055	16.6	50.3	34.6	46.2	11.4	66.4	11.7	55.5	−6.0	50.9
0056	37.6	51.0	22.5	37.5	14.6	24.7	1.2	33.1	6.7	26.8
0057	1.5	42.0	0.5	41.0	11.2	47.8	19.5	37.6	9.6	49.7
0058	−0.4	40.1	29.0	44.2	23.4	60.8	14.2	40.4	23.3	45.3
0059	−10.0	70.0	29.6	41.9	4.2	20.1	7.8	48.9	6.3	37.1

*% of $\sigma_{\lim}$.

as to how these spectra were generated. A more detailed description can be found in Ref *6*, so it will not be repeated here in this report. The transport composite mission spectrum table was also presented in Ref *6* and *8*.

All specimens used in the random spectrum load tests were the CCT specimens. They were identical to those used in the variable amplitude loading test program as described in the preceding section. All tests were conducted in the Structures Test Laboratory of Rockwell, using the 500K MTS fatigue test systems. Applied loads were controlled by the Datam servo system 70, a computer controlled fatigue test system. In most cases, the EDM crack starter slot in the specimen was precracked under constant-amplitude loading. Precracking was accomplished at a R-factor of zero and with a maximum cyclic stress of 69 MPa (10 ksi). This precracking produced an initial crack length $2c$ of approximately 7.62 mm (0.30 in.). All tests were run in ambient laboratory air at room temperature. The cyclic rates were between 4 and 6 Hz, depending on such factors as load level, load range, and the presence of compressive loads.

Again, six sets of analytical predictions were received by the ASTM Task Group E24.06.01 in this round-robin exercise. Table 6 lists the participants and their organizations, together with the analytical methods and computer codes used in their predictions. Detailed descriptions of the analytical method and numerical procedures used by participants are documented in the corresponding technical papers [*9–13*] collected in Ref *8*. These papers also provided dis-

TABLE 6—*Analytical methods and computer codes used in the random spectrum round-robin exercise.*

Analyst	Analysis Method	Computer Code Used
JC(1)	walker crack growth rate equation; compressive loads set to zero; tensile overload retardation effect not accounted for	EFFGRO[a]
CMH	root-mean-square method	CYCLIF
JN	modified Elber's equation; load interaction effects accounted for by analytical closure model	FAST
WSJ	modified Forman's equation; load interaction accounted for by the multiple-parameter yield zone model	CGR-LARC[b]
JR	Walker's crack-growth-rate equation; compressive loads set to zero; tensile overload retardation accounted by the Willenborg model	CRACKS
JC(2)	Walker's crack-growth-rate equation; load interaction effects accounted for by the Willenborg/Chang model	CRKGRO[c]

[a]The Vroman retardation model can be executed as an option.
[b]Originated from the CGR-GD program.
[c]Identified as the modified EFFGRO in Ref *8*.

cussions and assessments of the sensitivity of the parameters used in each fatigue crack growth analysis model by each individual participant.

Results of the round-robin analytical crack life predictions are summarized in Table 7. The associated test number and test parameters, which included the random flight mission type, and the DLS level of each test are also listed in this table. The test-life column records the number of cycles N_{test} for a center-through crack to grow from an initial crack size c_i (after precracking) to its critical size (identified as failure) c_{cr}. For those test cases where the experimental specimens were not tested to failure, the final crack sizes c_f were given. The analytical predicted lives N_{pred} were presented also in terms of the number of cycles. Again, in order to provide a better means in assessing predictive accuracies, the prediction ratios N_{pred}/N_{test} were calculated and presented in Table 7.

Conclusions

Five series of round-robin exercises have been carried out by ASTM Task Group E24.06.01 to determine (1) whether CT specimen constant-amplitude fatigue-crack-growth-rate data can be used to predict the fatigue crack lives of part-through cracks under constant amplitude loading and (2) whether data from constant-amplitude fatigue crack growth tests on CCT specimens can be used to predict fatigue crack lives of CCT specimens subjected to variable amplitude loadings, including single- or multiple-overloads, and random spectrum loadings. Based on the results of the five series of round-robin predictions, the following conclusions have been achieved.

1. The fatigue crack lives of part-through crack specimens under constant amplitude loadings can be predicted with sufficient accuracy using the constant amplitude load fatigue-crack-growth-rate data obtained from compact specimens.
2. Reasonably accurate predictions can be achieved for CCT specimens subjected to random spectrum loadings using CCT specimen constant-amplitude fatigue-crack-growth-rate data and the state-of-the-art crack growth retardation/acceleration models such as the Closure Model [*10*], the Multiple Parameter Yield Zone Model [*11*], and the Willenborg/Chang Model [*13*].
3. State-of-the-art crack-growth-analysis methods used by the round-robin exercise participants predicted fatigue crack lives more accurately for specimens subjected to random spectrum loadings than for the single- or multiple-overload/underload variable amplitude loadings.
4. The improvement of prediction accuracies depend primarily upon the availability of low-value *K* crack-growth data, in general, and the low stress level cases, in particular.
5. Test data other than constant amplitude fatigue-crack-growth-rate data are needed for predicting crack-growth behavior and lives of crack specimens under variable amplitude loadings.

TABLE 7—*Random spectrum loading round-robin exercise results.*

Test	Mission Type	Test Life, cycles (c_i to c_f, in.)[a]	Analytical Predictions, cycles (N_{pred}/N_{test})					
			JC(1)	CMH	JN	WSJ	JR	JC(2)
M-81	fighter (A-A)[b]	115700	140720	246000	115800	137000	213110	168720
	DLS[c] = 20 ksi[d]	(0.16 to 0.501)	(1.21)	(2.13)	(1.01)	(1.18)	(1.84)	(1.46)
M-82	fighter (A-A)	58585	44525	79000	39125	57000	74055	53312
	DLS = 30 ksi	(0.15 to failure)	(0.76)	(1.35)	(0.67)	(0.97)	(1.26)	(0.91)
M-83	fighter (A-A)	18612	14703	25359	11940	19700	25944	17309
	DLS = 40 ksi	(0.15 to failure)	(0.79)	(1.36)	(0.64)	(1.06)	(1.39)	(0.93)
M-84	fighter (A-G)[e]	268908	302816	395292	396230	342000	496284	368662
	DLS = 20 ksi	(0.158 to failure)	(1.13)	(1.47)	(1.47)	(1.27)	(1.85)	(1.37)
M-85	fighter (A-G)	95642	73644	99368	84850	90020	131868	91816
	DLS = 30 ksi	(0.144 to failure)	(0.77)	(1.04)	(0.89)	(0.94)	(1.38)	(0.96)
M-86	fighter (A-G)	36367	23275	29789	23820	30000	45034	29093
	DLS = 40 ksi	(0.153 to failure)	(0.64)	(0.82)	(0.65)	(0.82)	(1.24)	(0.80)
M-88	fighter (I-N)[f]	380443	281528	475292	959700	589000	810900	528816
	DLS = 30 ksi	(0.150 to failure)	((0.74)	(1.25)	(2.52)	(1.55)	(2.13)	(1.39)
M-89	fighter (I-N)	164738	95548	155294	242380	223000	288900	184507
	DLS = 40 ksi	(0.150 to failure)	(0.58)	(0.94)	(1.47)	(1.35)	(1.75)	(1.12)
M-90	fighter composite	218151	231240	430225	255090	270000	401140	290140
	DLS = 20 ksi	(0.153 to failure)	(1.06)	(1.97)	(1.17)	(1.24)	(1.84)	(1.33)
M-91	fighter composite	65627	51845	93473	51165	66000	97679	65630
	DLS = 30 ksi	(0.15 to failure)	(0.79)	(1.42)	(0.78)	(1.01)	(1.49)	(1.01)
M-92	fighter composite	22182	17080	31446	15370	22800	34000	21738
	DLS = 40 ksi	(0.15 to failure)	(0.77)	(1.42)	(0.69)	(1.03)	(1.53)	(0.98)
M-93	transport composite	1359000	2419020	...	1031200	1470000	3599000	1780290
	MSS[g] = 14 ksi	(0.25 to 0.54)	(1.78)	...	(0.76)	(1.08)	(2.65)	(1.31)
M-94	transport composite	279000	426870	...	348550	257000	628074	318060
	MSS = 19.6 ksi	(0.258 to 0.38)	(1.53)	...	(1.25)	(0.92)	(2.25)	(1.14)
Average (N_{pred}/N_{test}) ratio			(0.96)	(1.38)	(1.07)	(1.11)	(1.74)	(1.13)
Standard deviation			(0.36)	(0.42)	(0.33)	(0.20)	(0.42)	(0.22)

[a] 1 in. = 25.4 mm.
[b] A-A = air-to-air.
[c] DLS = design limit stress.
[d] 1 ksi = 6.9 MPa.
[e] A-G = air-to-ground
[f] I-N = instrumentation and navigation.
[g] MSS = maximum spectrum stress.

Acknowledgments

The round-robin prediction activities reported herein were conducted by ASTM Task Group E24.06.01 on Application of Fracture Data to Life Predictions, originally chaired by G. A. Vroman, now chaired by J. L. Rudd and the author. The task group is under the guidance of C. M. Hudson, Chairman of Subcommittee E24.06 on Fracture Mechanics Application. His continuous encouragement on this task group activity is highly appreciated.

The author would also wish to express his thanks to all the members of ASTM Committee E24 on Fracture Testing for their enthusiastic support and for actively participating in the round-robin exercises. The following members who contributed considerable time and effort to participate in the round-robin analyses are gratefully acknowledged:

- H. L. Eidinoff, Grumman Aerospace Corporation
- R. G. Forman, NASA Johnson Space Center
- G. Hales, General Dynamics, Fort Worth Division
- C. M. Hudson, NASA Langley Research Center
- W. S. Johnson, NASA Langley Research Center
- K-W Liu, Rockwell International Corporation, North American Aircraft operation
- J. C. Newman, NASA Langley Research Center
- D. E. Peterson, Rockwell International Corporation, Rocketdyne Division
- L. P. Pook, Department of Trade and Industry, United Kingdom
- J. L. Rudd, Air Force Flight Dynamics Laboratory
- M. Szamossi, Rockwell International Corporation, North American Aircraft operation
- M. L. Vanderglas, Ontario Hydro Research, Canada
- G. A. Vroman, Rockwell International Corporation, Rocketdyne Division, presently, TRW Defense and Space System Group

References

[1] Engle, R. M., Jr., "CRACKS II User's Manual," AFFDL-TM-74-173, Air Force Flight Dynamics Laboratory, Wright-Patterson Air Force Base, OH, July 1974.

[2] Szamossi, M., "Crack Propagation Analysis by Vroman's Model, Computer Analysis Summary, Program EFFGRO," NA-72-74, Rockwell International, Los Angeles, CA, 1972.

[3] Johnson, W. S., and Spamer, T., "A User's Guide to CGR-GD, A Computerized Crack Growth Prediction Program," General Dynamics Report F25-241, Fort Worth, TX, Nov. 1976.

[4] Ferguson, R. R. and Berryman, R. C., "Fracture Mechanics Evaluation of B-1 Materials," AFML-TR-76-137, Air Force Materials Laboratory, Wright-Patterson Air Force Base, OH, 1976.

[5] Vroman, G. A., "Life Prediction Analysis of Part-Through Cracks," *Part-Through Crack Fatigue Life Prediction, ASTM STP 687,* J. B. Chang, Ed., American Society for Testing and Materials, Philadelphia, 1979, pp. 89–95.

[6] Chang, J. B., Stolpestad, J. H., Shinozuka, M., and Vaicaitis, R., "Improved Methods for Predicting Spectrum Loading Effects—Phase I Report," AFFDL-TR-79-3036, Air Force Flight Dynamics Laboratory, Wright-Patterson Air Force Base, OH, 1979.

[7] Chang, J. B., Klein, E. J., and Cheng, J. S., "Automated Procedures for Fatigue Crack Growth Test data processing and presentation (PLOTRATE User Guide)," NA-78-860, Rockwell International, Los Angeles, CA, 1979.

[8] Chang, J. B., "Round-Robin Crack Growth Prediction on Center-Cracked-Tension Specimens Under Random Spectrum Loading," *Methods and Models for Predicting Fatigue Crack Growth Under Random Loading, ASTM STP 748*, J. B. Chang and C. M. Hudson, Eds., American Society for Testing and Materials, Philadelphia, 1981, pp. 3–40.

[9] Hudson, C. M., "A Root-Mean Square Approach for Predicting Fatigue Crack Growth Under Random Loading," *Methods and Models for Predicting Fatigue Crack Growth Under Random Loading, ASTM STP 748*, J. B. Chang and C. M. Hudson, Eds., American Society for Testing and Materials, Philadelphia, 1981, pp. 41–52.

[10] Newman, J. C., Jr., "A Crack-Closure Model for Predicting Fatigue Crack Growth Under Aircraft Spectrum Loading," *Methods and Models for Predicting Fatigue Crack Growth Under Random Loading, ASTM STP 748*, J. B. Chang and C. M. Hudson, Eds., American Society for Testing and Materials, Philadelphia, 1981, pp. 53–84.

[11] Johnson, W. S., "Multi-Parameter Yield Zone Model for Predicting Spectrum Crack Growth," *Methods and Models for Predicting Fatigue Crack Growth Under Random Loading, ASTM STP 748*, J. B. Chang and C. M. Hudson, Eds., American Society for Testing and Materials, Philadelphia, 1981, pp. 85–102.

[12] Rudd, J. L. and Engle, R. M., "Crack Growth Behavior of Center-Cracked Panels Under Random Spectrum Loading," *Methods and Models for Predicting Fatigue Crack Growth Under Random Loading, ASTM STP 748*, J. B. Chang and C. M. Hudson, Eds., American Society for Testing and Materials, Philadelphia, 1981, pp. 103–114.

[13] Chang, J. B., Szamossi, M., and Liu, K-W, "Random Spectrum Fatigue Crack Life Predictions With or Without Considering Load Interactions," *Methods and Models for Predicting Fatigue Crack Growth Under Random Loading, ASTM STP 748*, J. B. Chang and C. M. Hudson, Eds., American Society for Testing and Materials, Philadelphia, 1981, pp. 115–132.

Thomas Swift[1]

Fracture Analysis of Stiffened Structure

REFERENCE: Swift, T., "**Fracture Analysis of Stiffened Structure,**" *Damage Tolerance of Metallic Structures: Analysis Methods and Application, ASTM STP 842,* J. B. Chang and J. L. Rudd, Eds., American Society for Testing and Materials, 1984, pp. 69–107.

ABSTRACT: A method, based on displacement compatibility, is presented for the fracture analysis of cracked stiffened structure. The method provides an economical means for the determination of crack-tip stress intensity factors and stiffener stress concentration factors that can be used for parametric crack growth and residual strength studies during the initial design phase of an aircraft structure. The results of a typical parametric study are included. Emphasis is placed on the need to account for stiffener bending stresses in residual strength calculations. This need is supported by test evidence. Fastener shear failure known as unzipping is discussed. An example, supported by test evidence, is shown where this phenomenon can precipitate failure of stiffened structure containing cracks. A method of analysis, based on fastener nonlinear shear displacements, is described, which can account for the effect of fastener failure during the failure process of a cracked stiffened panel. The method is verified by test.

KEY WORDS: cracks, fracture (materials), crack propagation, damage tolerance, cracked stiffened structure, fracture mechanics, residual strength

In recent years there have been increasing demands to improve commercial aircraft structural safety. Paradoxically, present day economics are placing demands on designers to improve structural efficiency, which usually results in higher working stress levels. In addition, advanced computer technology being used today enables greater accuracy to be attained in stress analysis, thus reducing some of the conservatism that existed with less sophisticated methods. Even though considerable attention may be paid to ensuring an adequate fatigue life for the structure, this set of circumstances leads to the conclusion that the possibility of fatigue cracking within the life of the aircraft cannot be ignored. In order to maintain safety throughout the operational life of the structure, the current Federal Aviation Administration (FAA) regulations now include the requirement to base inspection intervals on crack propagation, taking into account not only fatigue as the damage initiator, but also corrosion and accidental damage.

[1]National resource specialist, Fracture Mechanics Metallurgy, Federal Aviation Administration, 4344 Donald Douglas Drive, Long Beach, CA 90808.

The current generation of wide-bodied aircraft were designed with the capability to sustain two bay skin cracks with broken central stiffeners anywhere in the basic structure, as illustrated by Fig. 1. This design philosophy, to include large damage capability, ensures increased external inspectability and should be continued for all future aircraft. It can be achieved with the proper combination of material choice, geometric configuration, and upper bound on limit stress levels.

Although analysis methods have been presented by numerous authors in the past [*1–4*], which enable allowable stress levels to be calculated for the two bay crack condition, recent contact with individuals within the fracture analysis community requires that a number of important points be re-emphasized.

Damage Tolerance Analysis Methods

Crack Propagation

Crack growth analysis for complex structural geometry is normally carried out by computerized integration procedures that solve the basic equation for constant amplitude loading

$$N = \int_{a_i}^{a_f} da/[F(\Delta KM)] \tag{1}$$

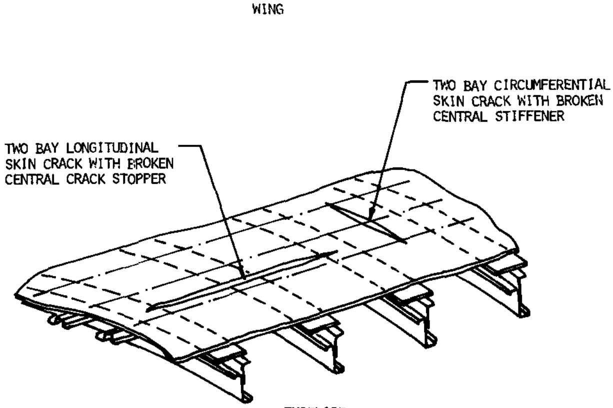

FIG. 1—*Basic structure damage capability at limit load.*

where

a = half crack length,
M = influence of material,
ΔK = stress intensity factor range,
N = number of cycles, and
a_f and a_i = final and initial crack sizes.

$$\Delta K = (1 - R)F_{\max}\sqrt{\pi a}\,\beta \qquad (2)$$

where

R = stress ratio,
$F_{\max}$ = cycle peak stress, and
β = effect of geometry.

Residual Strength

The residual strength for complex structural geometry can be calculated from the following equation

$$F_{cr} = K_{cr}/(\sqrt{\pi a}\,\beta) \qquad (3)$$

where

F_{cr} = gross stress at fast fracture or failure,
K_{cr} = critical stress intensity factor,
a = half crack length, and
β = effect of geometry.

The term β here is the same as that following Eq 2 and is one of the more important terms required in both crack propagation and residual strength analysis.

Effect of Geometry

There are several ways to determine the effects of geometry on the crack-tip stress intensity factor. One of these is by direct finite-element analysis of stiffened and unstiffened panels [*10*]. The value of β in this case is determined by taking the ratio of crack-tip stresses in the stiffened versus unstiffened panels as a function of crack length. This procedure requires the finite-element analysis of both stiffened and unstiffened panels and requires a considerable amount of computer running time.

Another method to determine the value of β is by finite-element energy release rate analysis. In this method the stress intensity factor is determined from the rate of change of energy with respect to crack area as the crack propagates. Stiffening element stresses, as a function of crack length, can also be obtained using this method. The approach is less expensive, by a factor of 2.0, than the direct finite-element method but is still costly when used for parametric studies during the design phase of an aircraft structure development.

Perhaps the most ideal method to determine the value of β, in parametric analysis, is the displacement compatibility method. This method involves calculating displacements in the cracked sheet at discrete locations and making these displacements compatible with stiffener displacements, after accounting for fastener displacement. The method is ideal for parametric studies of basic structural configurations because of its relatively low cost. This reduced cost, by as much as 50 to 1 compared to the two panel finite-element approach, is due primarily to the need only to invert a small matrix to determine unknown fastener forces. The majority of calculation needed is performed analytically, which is not as time consuming in a computer as inverting large matrices in a finite-element method. The displacement compatibility method will be described in more detail in this paper.

Displacement Compatibility Analysis Development

Method Description

The crack-tip stress intensity factor in an unstiffened panel is related to the stress field ahead of the crack tip. In the case of the stiffened panel, as the crack propagates, load is transferred out of the cracked sheet into the intact stiffening elements through the rivet fastening system. In the particular case of a two bay crack system described earlier, in which the center stiffener is assumed failed, load is transferred out of the broken stiffener into the cracked sheet as illustrated by Fig. 2. The resultant effect on the crack-tip stress intensity factor can be determined through a displacement compatibility analysis. In this analysis method, displacements in the cracked sheet at each fastener location are made compatible with those in the stiffening elements taking full account of stiffener bending and fastener shear displacement.

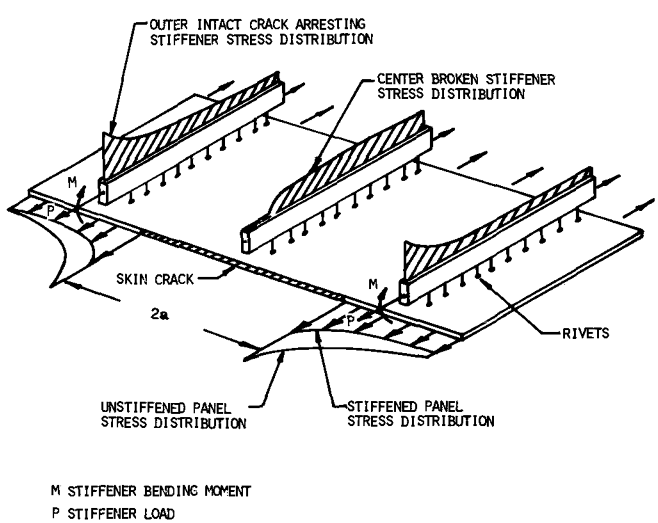

FIG. 2—*Stiffened panel stress distribution.*

Sheet Displacements

For the two bay crack condition with a broken central stiffener the cracked skin displacements are obtained by superposition of the four cases shown in Fig. 3. Displacements resulting from these four cases are

(1) V_1, the displacement anywhere in the cracked sheet caused by the applied gross stress,

(2) V_2, the displacement in the uncracked sheet resulting from uncracked outer stiffener fastener loads,

(3) V_3, the displacement in the uncracked sheet resulting from the center broken stiffener, and

(4) V_4, the displacements in the cracked sheet resulting from stress applied to the crack face equal and opposite to the stresses caused by rivet loads.

Consider Displacement V_1

Displacements in the cracked sheet resulting from overall gross stress can be determined using Westergaard's [*11*] complex stress functions with the theory of elasticity. This analysis is described briefly herein.

It can be shown that the differential equations of equilibrium for two-dimensional problems can be expressed as

$$(\partial \sigma_x / \partial x) + (\partial \tau_{xy} / \partial y) = 0 \tag{4}$$

$$(\partial \sigma_y / \partial y) + (\partial \tau_{xy} / \partial x) = 0 \tag{5}$$

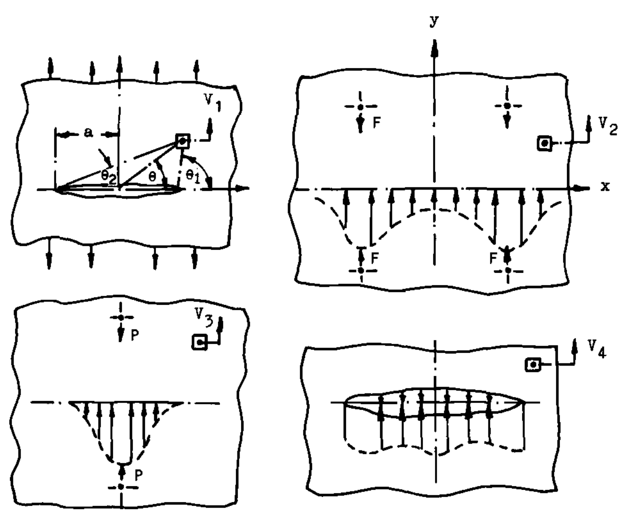

FIG. 3—*Deflections that are superimposed to determine total sheet displacement.*

In addition, to satisfy strain compatibility the following equation applies

$$(\partial^2\sigma_x/\partial x^2) + (\partial^2\sigma_y/\partial x^2) + (\partial^2\sigma_x/\partial y^2) + (\partial^2\sigma_y/\partial y^2) = 0 \tag{6}$$

Equations 4 and 5 can be satisfied by taking any stress function $\phi(x, y)$ and using the following expressions

$$\sigma_x = (\partial^2\phi/\partial y^2) \quad \sigma_y = (\partial^2\phi/\partial x^2) \quad \tau_{xy} = -(\partial^2\phi/\partial x\partial y) \tag{7}$$

Substituting Eq 7 into 6 leads to

$$(\partial^4\phi/\partial x^4) + (2\partial^4\phi/\partial x^2\partial y^2) + (\partial^4\phi/\partial y^4) = 0 \tag{8}$$

Equation 8 is a biharmonic equation, and any stress function chosen must satisfy this equation. Westergaard [11] found that choosing a stress function

$$\phi = Re\bar{\bar{Z}} + yIm\bar{Z} \tag{9}$$

where

$$\bar{Z} = (d\bar{\bar{Z}}/dz), \qquad Z = (d\bar{Z}/dz) \quad \text{and} \quad Z' = (dZ/dz)$$

would satisfy equilibrium and compatibility for any problem.

Re and *Im* are real and imaginary portions of the complex function Z. A complex function of $z = x + iy$, Z, is chosen to satisfy the boundary conditions of each specific problem.

Differentiation of Eq 9 and substitution into Eq 7 results in the following equations for stress

$$\begin{aligned} \sigma_x &= ReZ - yImZ' \\ \sigma_y &= ReZ + yImZ' \end{aligned} \tag{10}$$

Substitution of Eq 10 into the biaxial equation for strain in the y direction results in the following equation for strain

$$\varepsilon_y = (1/E)[(1 - \nu)ReZ + (1 + \nu)yImZ'] \tag{11}$$

where ε_y is strain in the y direction and ν is Poisson's ratio.

Integration of Eq 11 gives the following equation for displacement V anywhere in the cracked sheet

$$V = (1/E)[2Im\bar{Z} - (1 + \nu)yReZ] \tag{12}$$

For the infinite panel, Westergaard [11] determined that the following stress function would satisfy the boundary conditions

$$Z = \sigma z/\sqrt{z^2 - a^2} = \sigma z(z^2 - a^2)^{-1/2} \tag{13}$$

where σ is defined in Fig. 5.

Adding a term to cancel out the effect of stress in the x direction and substituting Eq 13 into Eq 12 gives an equation for the displacement V_1 for a uniaxially loaded panel

$$V_1 = \sigma\{2\sqrt{r_1 r_2}\sin(\theta_1 + \theta_2)/2 - (1 + \nu)yr \cdot [\cos(\theta - \theta_{1/2} - \theta_{2/2})]/\sqrt{r_1 r_2} + \nu y\}/E \tag{14}$$

Consider Displacement V_2

The stress distribution anywhere in an infinite plate resulting from a concentrated force F can be determined from the work of Love [*12*] as follows

$$\sigma_y = [Fy(1 + \nu)/4\pi B(x^2 + y^2)]\{[(3 + \nu)/(1 + \nu)] - [2x^2/(x^2 + y^2)]\} \tag{15}$$

The displacement resulting from force F is given by

$$V_F = [F(1 + \nu)/4\pi BE]\{[(3 - \nu)/2]\log(x^2 + y^2) + [(1 + \nu)x^2/(x^2 + y^2)]\} + C \tag{16}$$

Where x and y are measured from the load point, C is a constant of integration, and B is the plate thickness. Equation 16 contains a singularity that can be eliminated by distribution of the concentrated force F uniformly over the rivet diameter D. Using Eq 16 to obtain the displacement of an elemental load and integrating the effect over the rivet diameter will yield an equation free from the singularity at the load center. The resulting equation can then be used to obtain the displacement V_2 for the system of four forces shown in Fig. 3, by superposition as follows

$$\begin{aligned} V_2(x_i, y_i, x_j, y_j) = {} & \frac{F(1 + \nu)(3 - \nu)}{16\pi EB}\left\{(X_A + 1)\log\left[\frac{(X_A + 1)^2 + Y_A^2}{(X_A + 1)^2 + Y_B^2}\right]\right. \\ & - (X_A - 1)\log\left[\frac{(X_A - 1)^2 + Y_A^2}{(X_A - 1)^2 + Y_B^2}\right] + (X_B + 1) \\ & \cdot \log\left[\frac{(X_B + 1)^2 + Y_A^2}{(X_B + 1)^2 + Y_B^2}\right] - (X_B - 1)\log\left[\frac{(X_B - 1)^2 + Y_A^2}{(X_B - 1)^2 + Y_B^2}\right] \\ & + 4\left(\frac{1 - \nu}{3 - \nu}\right)\left[Y_A \tan^{-1}\left(\frac{2Y_A}{Y_A^2 + X_A^2 - 1}\right) + Y_A \tan^{-1}\right. \\ & \cdot \left(\frac{2Y_A}{Y_A^2 + X_B^2 - 1}\right) - Y_B \tan^{-1}\left(\frac{2Y_B}{Y_B^2 + X_B^2 - 1}\right) \\ & \left.\left. - Y_B \tan^{-1}\left(\frac{2Y_B}{Y_B^2 + X_A^2 - 1}\right)\right]\right\} \end{aligned} \tag{17}$$

Consider Displacement V_3

The displacement V_3, resulting from a system of two rivet forces at the center of the panel as shown in Fig. 3, can be obtained in the same way as Eq 17. Thus, the displacement V_3 for a pair of forces P is given by

$$
\begin{aligned}
V_3(x_i, y_i, y_j) = \frac{P(1+\nu)(3-\nu)}{16\pi EB} & \left\{ \left(\frac{2x_i}{D} + 1\right) \log\left[\frac{\left(\frac{2x_i}{D} + 1\right)^2 + Y_A^2}{\left(\frac{2x_i}{D} + 1\right)^2 + Y_B^2}\right] \right. \\
& - \left(\frac{2x_i}{D} - 1\right) \log\left[\frac{\left(\frac{2x_i}{D} - 1\right)^2 + Y_A^2}{\left(\frac{2x_i}{D} - 1\right)^2 + Y_B^2}\right] + 4\left(\frac{1-\nu}{3-\nu}\right) \\
& \left. \cdot \left[Y_A \tan^{-1}\left(\frac{2Y_A}{Y_A^2 + \frac{4x_i^2}{D^2} - 1}\right) - Y_B \tan^{-1}\left(\frac{2Y_B}{Y_B^2 + \frac{4x_i^2}{D^2} - 1}\right)\right]\right\}
\end{aligned}
\tag{18}
$$

where

$X_A = (2/D)(x_i - x_j)$,

$X_B = (2/D)(x_i + x_j)$,

$Y_A = (2/D)(y_i - y_j)$, and

$Y_B = (2/D)(y_i + y_j)$.

The ith term reflects the point at which the displacement is required, and the jth term reflects coordinates of the forces.

Consider Displacement V_4

The stress distribution along the x axis, where the crack will eventually be, resulting from a system of forces as shown in Fig. 4, can be obtained from Eq 15 by transfer of axis. The forces F and P reflect the effects of outer stiffener and center stiffener rivet forces, respectively

$$\sigma_y(x, o) = -[(1+\nu)y_1/2\pi B][F_j\alpha(x_j, y_j, b) + P_j\beta(y_j, b)] \tag{19}$$

where

$$
\begin{aligned}
\alpha(x_j, y_j, b) = [(3+\nu)/(1+\nu)] & \left[\frac{1}{(b-x_j)^2 + y_j^2} + \frac{1}{(b+x_j)^2 + y_j^2}\right] \\
& - \frac{2(b-x_j)^2}{[(b-x_j)^2 + y_j^2]^2} - \frac{2(b+x_j)^2}{[(b+x_j)^2 + y_j^2]^2}
\end{aligned}
\tag{20}
$$

$$\beta(y_j, b) = \left(\frac{3+\nu}{1+\nu}\right)\left(\frac{1}{b^2 + y_j^2}\right) - \left[\frac{2b^2}{(b^2 + y_j^2)^2}\right] \tag{21}$$

The displacement V_4 is obtained by applying an equal and opposite stress distribution over the crack face to cancel out the stress caused by the rivet forces

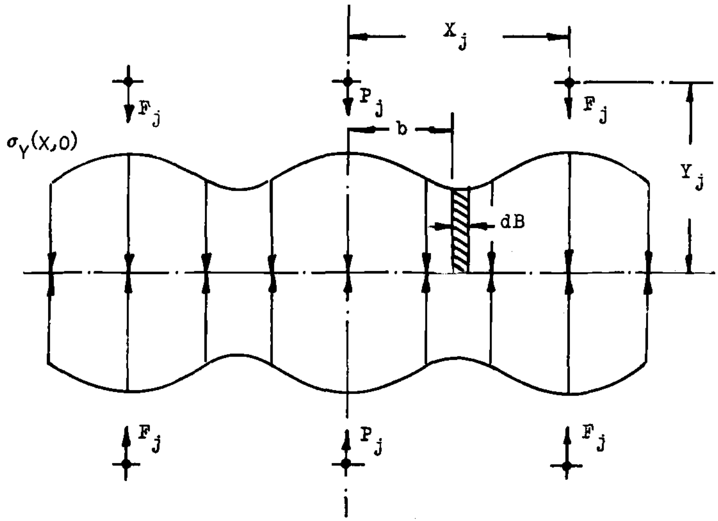

FIG. 4—*Stress distribution at* Y = 0 *because of rivet forces.*

F and P. The displacement caused by this stress distribution can be obtained from Eq 12 by using a complex stress function derived by Irwin [13] for the condition shown in Fig. 5

$$Z = 2Pa/[B\pi(z^2 - b^2)]\left[\frac{1 - (b/a)^2}{1 - (a/z)^2}\right]^{1/2} \tag{22}$$

Substituting $\sigma_y(x, o)tdb$ for P, and integrating over half the crack length will eventually yield an expression for V_4 in general terms as follows

$$V_4 = -[(1 + \nu)y_j/2\pi^2EB]$$
$$\left[F_j\int_0^a \alpha(x_j, y_j, b)\varepsilon(x_i, y_i, b)\,db + P_j\int_0^a \beta(y_j, b)\varepsilon(x_i y_i, b)\,db\right] \tag{23}$$

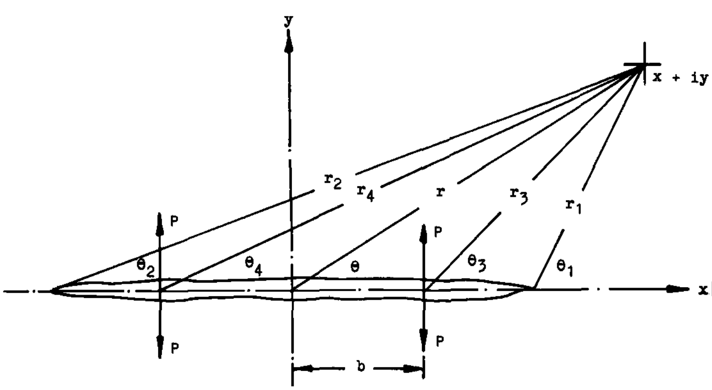

FIG. 5—*Concentrated forces applied to crack face.*

where α and β are given by Eqs 20 and 21, and ε is given by

$$\varepsilon(x_i, y_i, b) = \log\left[\frac{(a^2 - b^2) + (a^2 - b^2)^{1/2}(BC + AD) + r_1 r_2}{(a^2 - b^2) - (a^2 - b^2)^{1/2}(BC + AD) + r_1 r_2}\right]$$
$$- \frac{y_i(1 + \nu)(a^2 - b^2)^{1/2}}{r_1 r_2 r_3^2 r_4^2} \tag{24}$$
$$\{(x_i^2 - b^2 - y_i^2)[x_i(AC - BD) + y_i(BC + AD)]$$
$$- 2x_i y_i[x_i(BC + AD) - y_i(AC + BD)]\}$$

where

$A = (r_i + x_i - a)^{1/2}$,

$B = (r_i - x_i + a)^{1/2}$,

$C = (r_2 + x_i + a)^{1/2}$, and

$C = (r_2 - x_i - a)^{1/2}$.

It is necessary to integrate Eq 23 numerically. The total sheet displacement is as follows:

$$V_{\text{Total}} = V_1 + V_2 + V_3 + V_4$$

Outer, Intact Stiffener Displacement

The outer stiffener is assumed to be supported on three frames running normal to the stiffeners. The center frame is on the skin crack centerline. Stiffener extension at the fastener shear face is determined because of axial loads and bending from fastener loads and direct loads resulting from axial stresses. Stiffener bending is induced since the fastener shear faces are offset from the stiffener neutral axis. The average bending moment between each fastener, obtained through the use of the three-moment-equation, is given by

$$M_{A_i} = \sum_{j=i}^{j=2n} CF_j - \left[\frac{3C}{2L^3}\sum_{j=n+1}^{j=2n} F_j(2Lv_j - y_j^2)\right]\left[L - \frac{y_{(i-1)} + y_i}{2}\right] \tag{25}$$

Stiffener displacement caused by bending from fastener loads is given by

$$\delta_{M_i} = (C/EI)\sum_{i=n+1}^{i=i} M_{A_i}(Y_i - Y_{(i-1)}) \tag{26}$$

Stiffener displacement resulting from direct fastener loads is given by

$$\delta_{D_i} = (1/AE)\sum_{j=n+1}^{j=i} F_j y_j + (y_i/AE)\sum_{j=i+1}^{j=2n} F_j \tag{27}$$

Stiffener displacement resulting from gross stress is given by

$$\delta_{G_i} = \sigma y_i/E \tag{28}$$

where

C = distance from neutral axis to shear face,
I = stiffener inertia,
L = distance between supports,
n = number of active fasteners per stiffener, and
y = rivet coordinate from crack centerline.

Center Broken Stiffener Displacements

The center stiffener is assumed broken at the center of the skin crack. It is assumed supported by a frame at the break and two other frames at each side of the break. The average bending moment between each fastener is given by

$$M_{A_i} = \sum_{j=1}^{j=i} CP_j - \left[\frac{C}{L}\sum_{j=1}^{j=n} P_j\left(\frac{5}{4} - \frac{3Y_j}{4L^2}\right)\right]\left[\frac{y_{(i+1)} + y_i}{2}\right] \tag{29}$$

Stiffener displacement resulting from bending from fastener loads is given by

$$\delta_{M_i} = (C/EI)\sum_{i=i}^{i=n-1} M_{A_i}(y_{(i+1)} - y_i) \tag{30}$$

Stiffener displacement resulting from direct load is given by

$$\delta_{D_i} = (1/AE)\sum_{j=1}^{j=i} P_j(y_n - y_1) + (1/AE)\sum_{j=i+1}^{j=n-1} P_j(y_n - y_j) \tag{31}$$

Fastener Displacements

The displacement compatibility analysis is based on displacement compatibility between the cracked skin and the stiffener after accounting for rivet displacement. Thus, stiffener plus rivet displacements are made equal to skin displacements. It is of interest to note that the rivet contribution to stiffener plus rivet displacement is more than 75% and is therefore an extremely important consideration. Errors up to 50% in crack-tip stress intensity factors can result by neglecting fastener displacements.

It has been determined by tests that the elastic displacement in shear can be represented by the following empirical relation

$$\delta_R = (F/ED)\left[A + C\left(\frac{D}{B_1} + \frac{D}{B_2}\right)\right] \tag{32}$$

where

F = applied load,
E = modulus of sheet material,
D = rivet diameter,
B_1 and B_2 = thickness of joined sheets,
A = 5.0 for aluminum rivets and 1.666 for steel fasteners, and
C = 0.8 for aluminum rivets and 0.86 for steel fasteners.

Compatibility of Displacment

The solution of the stiffened panel problem is obtained by the solution of a set of simultaneous equations based on the following compatibility relations. Compatibility at the center broken stiffener is given by

$$
\begin{aligned}
&\sum_{j=n+1}^{j=2n} F_j\left[\nu_2(x_n, y_n, x_j, y_j) - \frac{(1+\nu)y_j}{2\pi^2 EB}\int_0^a \alpha(x_j, y_j, b)\varepsilon(x_n, y_n, b)\, db\right] \\
&- \sum_{j=1}^{j=n} P_j\left[\nu_3(x_n, y_n, y_j) - \frac{(1+\nu)y_j}{2\pi^2 EB}\int_0^a \beta(y_j, b)\varepsilon(x_n, y_n, b)\, db\right] \\
&+ \delta R_n - \delta D_i - \delta M_i - \delta R_i \\
&- \sum_{j=n+1}^{j=2n} F_j\left[\nu_2(x_i, y_i, x_j, y_j) - \frac{(1+\nu)y_j}{2\pi^2 EB}\int_0^a \alpha(x_j, y_j, b)\varepsilon(x_i, y_i, b)\, db\right] \\
&+ \sum_{j=1}^{j=+n} P_j\left[\nu_3(x_i, y_i, y_j) - \frac{(1+\nu)y_j}{2\pi^2 EB}\int_0^a \beta(y_j, b)\varepsilon(x_i, y_i, b)\, db\right] \\
&= \sigma\nu_1(x_i, y_i) - \sigma\nu_1(x_n, y_n)
\end{aligned}
\tag{33}
$$

Compatibility at the outer intact stiffener is given by:

$$
\begin{aligned}
&\delta D_i + \delta M_i + \delta R_i \\
&- \sum_{j=n+1}^{j=2n} F_j\left[\nu_2(x_i, y_i, x_j, y_j) - \frac{(1+\nu)y_j}{2\pi^2 EB}\int_0^a \alpha(x_j, y_j, b)\varepsilon(x_i, y_i, b)\, db\right] \\
&+ \sum_{j=1}^{j=n} P_j\left[\nu_3(x_i, y_i, y_j) - \frac{(1+\nu)y_j}{2\pi^2 EB}\int_0^a \beta(y_j, b)\varepsilon(x_i, y_i, b)\, db\right] \\
&= \sigma\nu_1(x_i, y_i) - \delta G_i
\end{aligned}
\tag{34}
$$

A system of simultaneous equations is set up from these compatibility equations as shown in Fig. 6. The matrix is $2n \times 2n$ in size where n is the number of active fasteners assumed in each of the center and outer stiffeners. A value of n of 15 is usually adequate for the broken central stiffener case.

As illustrated in Fig. 6, the compatibility matrix is made up of a series of sections formed by terms of the compatibility equations. The section DCC is a 14×14 matrix of skin displacements at each of the center stiffener rivets resulting from center stiffener rivet loads. Only the first 14 rivets are considered in this matrix since all the displacements at the broken center stiffener are made relative to the fifteenth, most remote rivet from the crack, and this is considered separately. DCC is formed from the eighth term of Eq 33. The section DCO is a 14×15 matrix of skin displacements at each of the center stiffener rivets resulting from outer stiffener rivet loads.

DCO is formed from the seventh term of Eq 33. Both DCC and DCO are initially formulated as 15×15 matrices. The fifteenth row in DCC is replaced by a series of ones. The reason for this is to form the fifteenth equation, which is the equilibrium for the broken central stiffener and equates the sum of the rivet

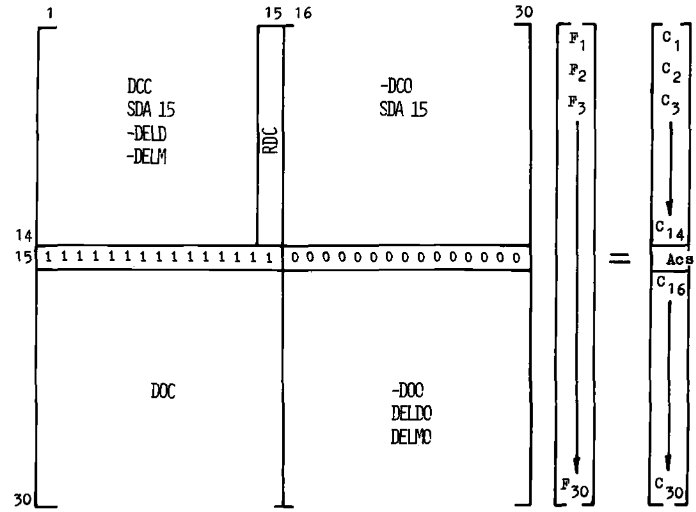

FIG. 6—*Matrix of compatibility equations for two bay crack with center broken stiffener.*

loads to the load in the stiffener beyond the fifteenth rivet. The fifteenth column of DCC is replaced by the rivet flexibility of the fifteenth rivet in the center stiffener, obtained from Eq 32. The section SDA15 is a 14 × 30 matrix representing the skin displacement at the fifteenth rivet in the center stiffener. This displacement is the one to which all center stiffener displacements are referenced. The first 14 columns are formed from DCC with i equal to 15. Column 15 in this matrix is eventually replaced by RDC as shown in Fig. 6, based on Eq 32. Columns 16 to 30 are formed from DCO with i equal to 15, that is, displacement at the fifteenth rivet. All the 14 rows in this matrix are identical to each other. The section DELD is a 14 × 14 matrix of center stiffener displacements resulting from rivet direct loads. The matrix is formulated from Eq 31 plus the third term of Eq 34. The section DELM is a 14 × 14 matrix of center stiffener displacements resulting from bending. It is formed by first obtaining a matrix DDELM, which is a matrix of increments of stiffener displacement resulting from bending. For example, $\Delta\delta M_1$ ($DDELM_1$) is the extension of the center broken stiffener between the first and second rivets. $\Delta\delta M_2$ ($DDELM_2$) is the center stiffener extension between the second and third rivets and so forth. The total displacement at the ith rivet is given by Eq 30. DELM is formed by first summing the elements of the DDELM matrix. The section DOC is a 15 × 15 matrix of skin displacements at each of the outer stiffener rivets resulting from center stiffener rivet loads. DOC is formed from the fifth term of Eq 34 where j is 1 to 15, and i is 15 to 30. The i, j notation reflects the skin displacement at the ith rivet resulting from the jth rivet load. The section DOO is a 15 × 15 matrix of skin displacements at each of the outer stiffener rivets resulting from outer stiffener rivet loads. DOO is formed from fourth term of Eq 34. The section DELDO is a 15 × 15 matrix of outer stiffener displacements resulting from rivet direct loads and is formulated from first and third terms of Eq 34, or Eqs 27 and 32. The section DELMO is a 15 × 15 matrix of outer stiffener displacements resulting from bending. It is formed by first obtaining a matrix DDELMO, which is a matrix of increments of outer stiffener displacements caused by bending. For example, $\Delta\delta M_1$ ($DDELMO_1$) is the extension of the outer stiffener between the first and second rivets. $\Delta\delta M_2$ ($DDELMO_2$) is the extension of the outer stiffener between the second and third rivets. The total deflection at the ith rivet is given by the second term of Eq 34 or Eq 30. The matrix DELMO is formed by summing the elements of the DDELMO matrix.

The final compatibility matrix, illustrated by Fig. 6, is inverted and solved for fastener loads.

Crack-Tip Stress Intensity Factor

Crack-tip stress intensity factors caused by each pair of center stiffener fastener loads as shown in Fig. 7*a* are given by [*14*]

$$K_{cs} = (\sqrt{a}P/2B\sqrt{\pi})\left[\frac{2a^2 + (3 + \nu)Y_1^2}{(a^2 + Y_1^2)^{3/2}}\right] \tag{35}$$

For each set of outer stiffener fastener loads, as shown in Fig. 7*b*, the stress intensity is given by [*14*]

$$K = (2FY_1\sqrt{\pi a}/\pi B)\left[\left(\frac{3 + \nu}{2}\right)\right]\left[I_1 - (1 + \nu)I_2\right] \tag{36}$$

where

$$I_1 = \beta/Y_1\sqrt{(Y_1^2 + a^2 - x_1^2)^2 + 4x_1^2Y_1^2} \tag{37}$$

$$I_2 = \frac{[(a^2 + x_1^2)Y_1^2 + (a^2 - x_1^2)^2]\beta^2 + x_1^2Y_1^2(Y_1^2 - a^2 + x_1^2)}{2Y_1\beta[(Y_1^2 + a^2 - x_1^2)^2 + 4x_1^2Y_1^2]^{3/2}} \tag{38}$$

$$\beta = (1/\sqrt{2})\left[(Y_1^2 + a^2 - x_1^2) + \sqrt{(Y_1^2 + a^2 - x_1^2)^2 + 4x_1^2Y_1^2}\right]^{1/2} \tag{39}$$

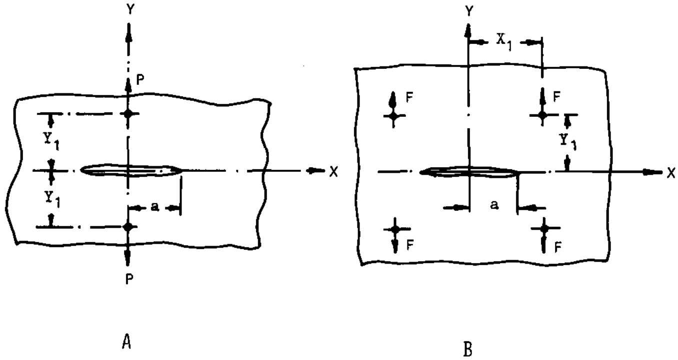

FIG. 7—*Fastener forces.*

Total stress intensity is obtained by superposition for each set of active fasteners, paying attention to load direction, and the effects of overall stress.

Parametric Study

Geometry Description

In order to illustrate the usefulness of the displacement compatibility method a parametric study has been performed similar to a study that may take place during the development of any commercial aircraft structure. The example chosen is a two bay crack with a broken central stiffener that may be representative of a circumferential crack in the crown of a fuselage shell subjected to axial stress resulting from pressure and fuselage bending stresses. Figure 8 shows the configurations considered. The effects of varying the stiffener area and spacing are considered.

Effects of Stiffening on Stress Intensity

The effect of stiffening on crack-tip stress intensity factor for the considered configurations is illustrated by Figs. 9 through 12. Figure 9 illustrates that when crack lengths are small the effect of the broken stiffener is to increase the stress intensity factor above that expected from an unstiffened panel. As the crack becomes longer, the outer intact stiffeners cause a reduction in the stress intensity factor below that expected from an unstiffened panel, thus illustrating the crack arrest capability of the outer intact stiffeners. The values of β shown in Figs. 9

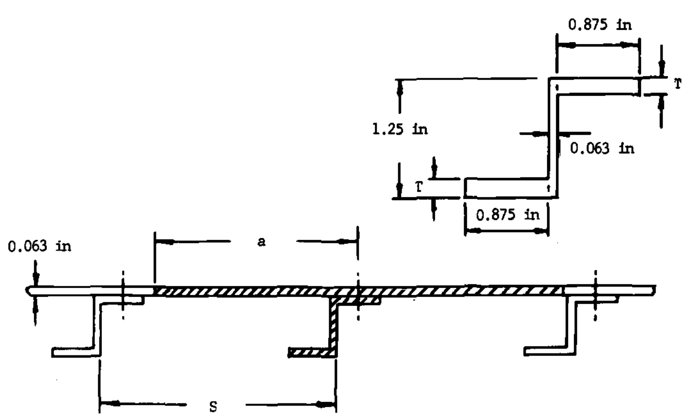

CASES CONSIDERED

STIFFENER SPACING S	STIFFENER FLANGE THICKNESS T	STIFFENER AREA
6.0 in	0.063 in	0.1890 sq.in
8.0 in	0.100 in	0.2538 sq.in
10.0 in	0.160 in	0 3788 sq in
12.0 in	0.190 in	0.4113 sq.in

FIG. 8—*Configurations considered in parametric study where 1 in. = 25.4 mm and 1 in.^{2} = 645.16 mm^2.*

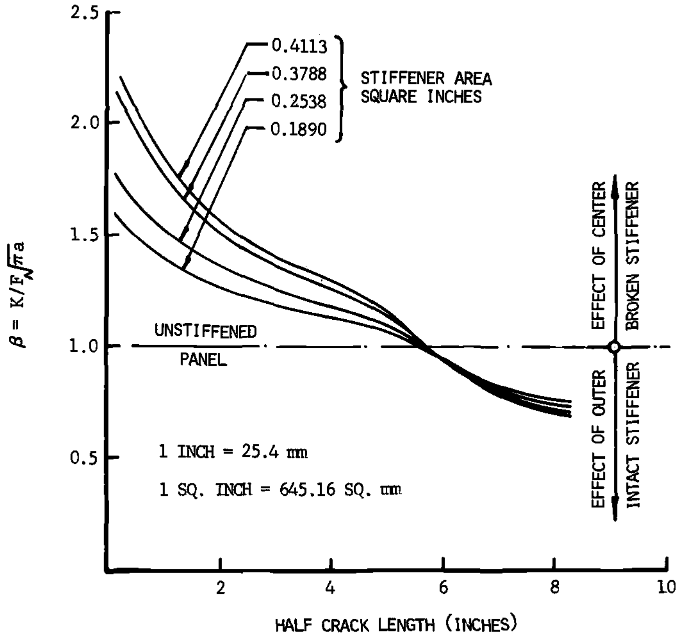

FIG. 9—*Effect of stiffening on crack-tip stress intensity factor stiffener spacing 152.40 mm (6 in.).*

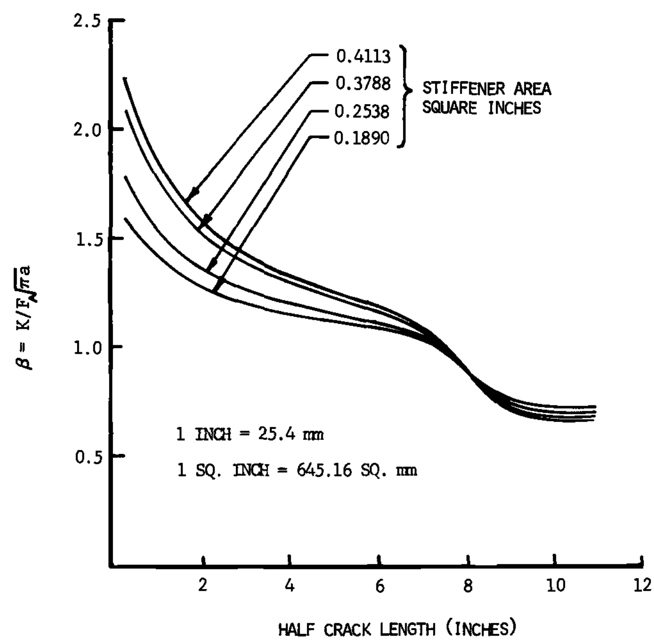

FIG. 10—*Effect of stiffening on crack-tip stress intensity factor stiffener spacing 203.20 mm (8 in.).*

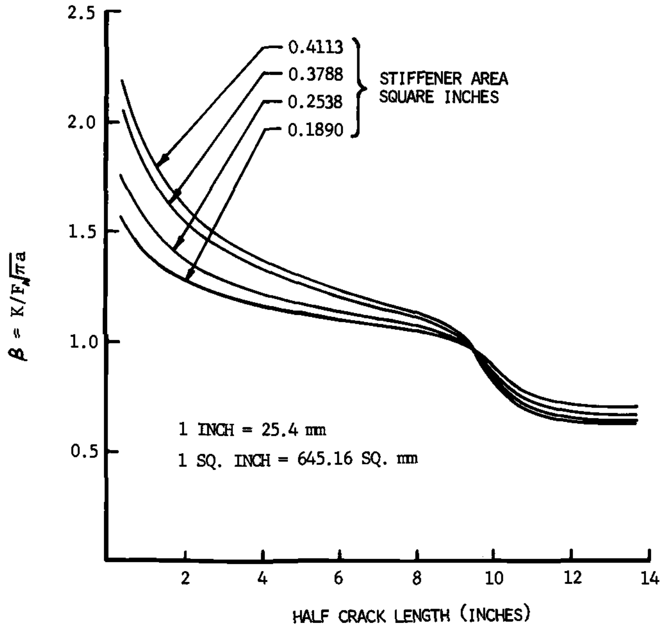

FIG. 11—*Effect of stiffening on crack-tip stress intensity factor stiffener spacing 254.00 mm (10 in.).*

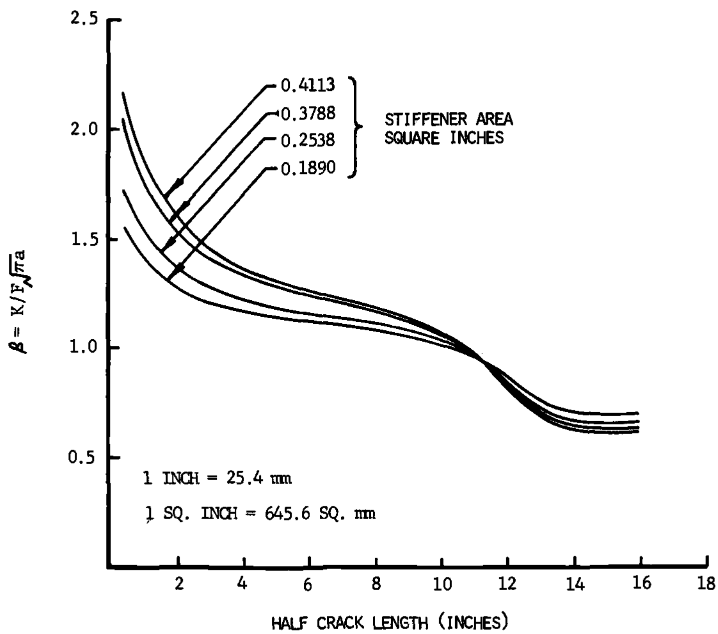

FIG. 12—*Effect of stiffening on crack-tip stress intensity factor stiffener spacing 304.80 mm (12 in.).*

through 12 would be those used in Eq 2 for the stress intensity factor range that is used in Equation 1 for crack propagation analysis. They would also be used in Eq 3 for residual strength calculation.

Outer Intact Stiffener Bending

Figure 13 illustrates the bending stress in the outer intact stiffener as a function of skin crack propagation. The case considered for illustration is a 203.2-mm (8.0-in.) stiffener spacing and a stiffener area of 265.35 mm^2 (0.4113 in.^{2}). The residual strength of the panel must take stiffener stresses into account, and it is important to consider the outer cap stress when considering stiffener strength. Figure 13 shows the outer intact stiffener stress in the most critical location in line with the skin crack. The importance of stiffener bending, often ignored in residual strength calculations, will be illustrated later with test results.

Residual Strength Diagram

A typical residual strength diagram is illustrated by Fig. 14 from the parametric study described. Stiffener spacing for the illustration is 203.2 mm (8.0 in.) and stiffener area 265.35 mm^2 (0.4113 in.^{2}). The diagram shows a skin fracture curve based on maximum outer fiber bending stress. For illustration purposes the skin

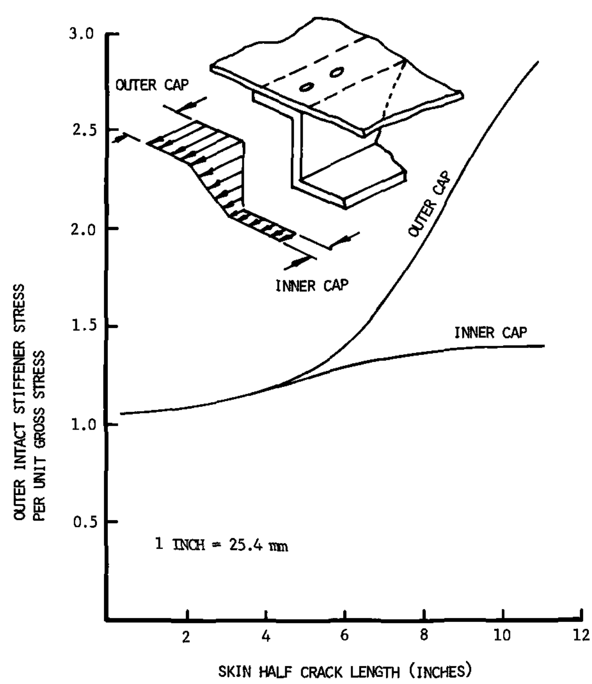

FIG. 13—*Outer intact stiffener stresses resulting from unit gross panel stress stiffener spacing 203.2 mm (8 in.) and stiffener area 265.35 mm^2 (0.4112 in.^{2}).*

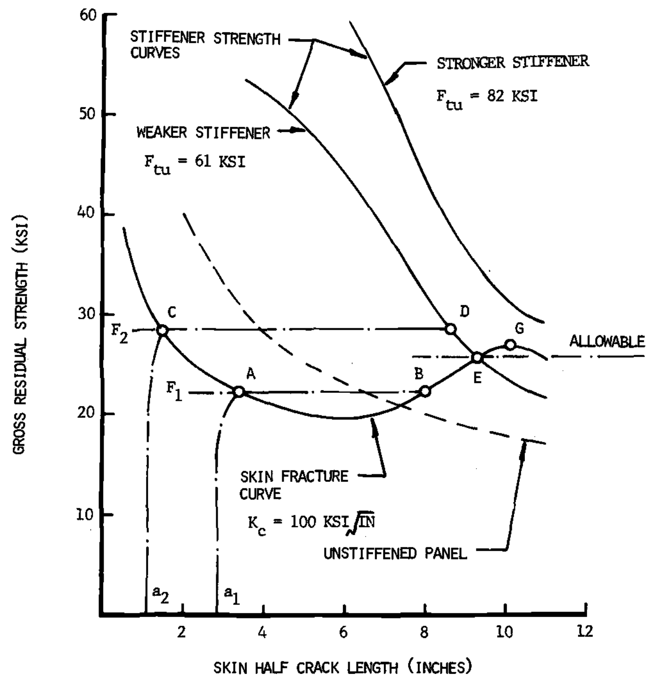

FIG. 14—*Stiffened panel residual strength curve stiffener spacing 203.2 mm (8 in.) and stiffener area 265.35 mm² (0.4113 in.²) where 1 ksi = 6.895 MPa and 1 ksi·in.$^{1/2}$ = 1.0989 MPa·M$^{1/2}$.*

fracture toughness has been assumed to be 109.89 MPa · m$^{1/2}$ (100 ksi · in$^{1/2}$). Two different stiffener materials have been assumed to illustrate the effect of varying stiffener material strength. These materials are 7075-T6 extrusion with ultimate strength 565.39 MPa (82 ksi) and 2024-T3 extrusion with ultimate strength 420.6 MPa (61 ksi). An unstiffened panel curve is also included to illustrate the effect of the broken central stiffener. For shorter crack lengths, the unstiffened panel residual strength is higher than for the stiffened panel. The diagram is explained as follows. If a crack of half length a_1 exists in the panel, and the gross stress on the panel is gradually increased, some slow stable tearing of the skin will usually take place, and fast fracture will occur at point A, when the gross stress is F_1. The skin crack will be arrested at point B. If on the other hand, a skin crack of half length a_2 exists, and gross stress is gradually applied, fast fracture will take place at a gross stress F_2, at point C, and failure of the panel will take place. If the stiffeners are made from the stronger material then failure would be precipitated by skin fracture criterion since the applied stress F_2 is higher than point G on the skin fracture curve. With the weaker stiffener, the panel allowable is point E, since any fast fracture below this point would be arrested, and any fast fracture above this point would cause failure of the panel where the failure is precipitated by outer stiffener failure. With the stronger stiffener the panel allowable would be point G.

Effect of Stiffener Area Variation

The effect on residual strength of varying the stiffener area is illustrated by Fig. 15. The stiffener spacing for this set of curves is held constant at 304.87 mm (12.0 in.). Skin fracture toughness is assumed to be 131.87 MPa · $m^{1/2}$ (120 ksi · $in.^{1/2}$) and stiffener ultimate strength is 564.39 MPa (82 ksi). The intersection of the stiffener strength curve with the corresponding skin fracture curve reflects the residual strength for the two bay crack condition since any fast fracture at a stress higher than this point would cause failure.

Effect of Stiffener Spacing Variation

The effect of varying the stiffener spacing on residual strength is illustrated by Fig. 16. The stiffener area for this set of curves is held constant at 265.35 $(mm)^{1/2}$ (0.4113 $in.^{1/2}$). In the case of stiffener spacing equal to 152.4 mm (6.0 in.) the point A, at the peak of the skin fracture curve, limits the residual strength since the stiffener strength curve does not intersect the skin fracture curve at or ahead of its peak. In all other cases, represented by points B, C, and D, the stiffener strength curve intersects the skin fracture curve, and these points represent the residual strength for the two bay crack condition.

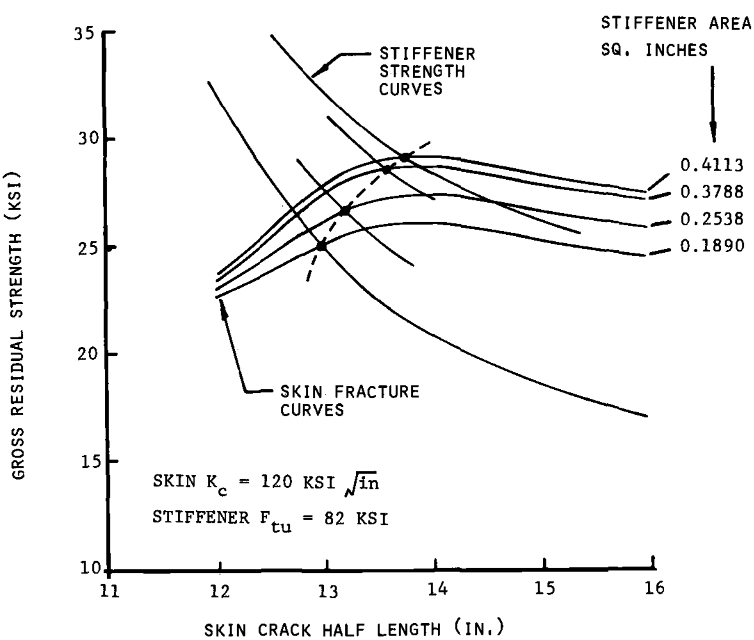

FIG. 15—*Effect of stiffener area on residual strength with stiffener spacing 304.8 mm (12.0 in.) where 1 ksi = 6.895 MPa, 1 in. = 25.4 mm, and 1 ksi·in.$^{1/2}$ = 1.0989 MPa·m$^{1/2}$*

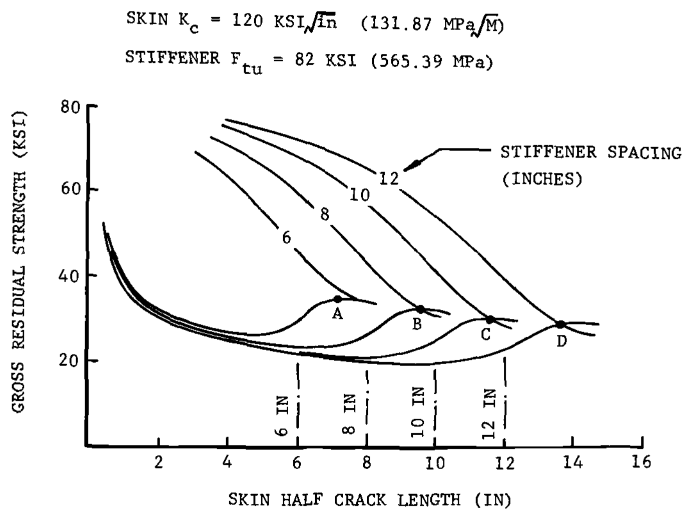

FIG. 16—*Effect of stiffener spacing on residual strength with stiffener area 265.35 mm² (0.4113 in.²).*

Results of Parametric Study

The results of varying stiffener area and spacing, skin fracture toughness, and stiffener material ultimate strength are illustrated by Figs. 17 through 22. These curves represent the residual strength for a two bay skin crack with a broken central stiffener for the geometry variation shown in Fig. 8. The residual strength increases with increasing stiffener area, skin fracture toughness, and stiffener material strength. It decreases with increased stiffener spacing.

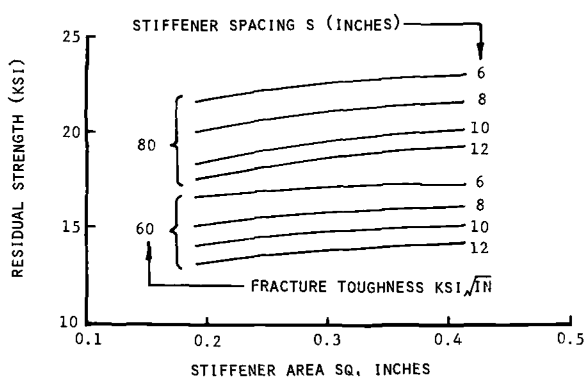

FIG. 17—*Effect of stiffener area and spacing on residual strength skin fracture toughness with 60 and 80 ksi·in.$^{1/2}$ stiffener* F_{tu} *61 ksi where 1 ksi = 6.895 MPa, 1 in.² = 654.16 mm², 1 in. = 25.4 mm, and 1 ksi·in$^{1/2}$ = 1.0989 MPa·m$^{1/2}$.*

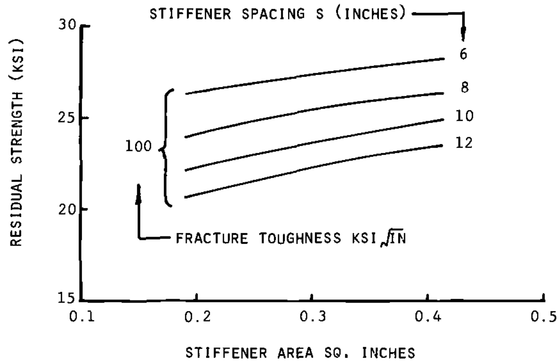

FIG. 18—*Effect of stiffener area and spacing on residual strength with skin fracture toughness 100 ksi·in.*$^{1/2}$ *and stiffener* F_{tu} *71 ksi where 1 ksi = 6.895 MPa, 1 in.*^{2} *= 645.16 mm*^{2}*, 1 in. = 25.4 mm, and 1 ksi·in.*$^{1/2}$ *= 1.0989 MPa·m*$^{1/2}$*.*

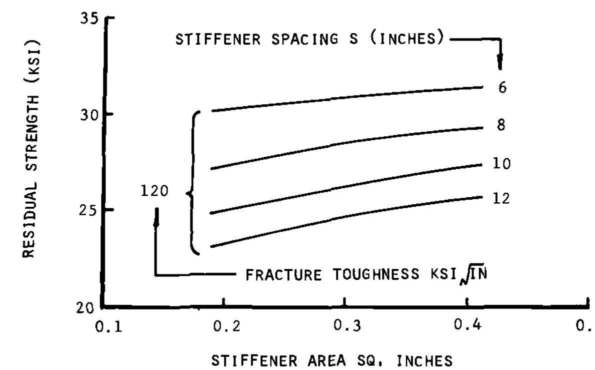

FIG. 19—*Effect of stiffener area and spacing on residual strength with skin fracture toughness 120 ksi·in.*$^{1/2}$ *and stiffener* F_{tu} *61 ksi where 1 ksi = 6.895 MPa, 1 in.*^{2} *= 645.16 mm*^{2}*, 1 in. 25.4 mm, and 1 ksi·in.*$^{1/2}$ *= 1.0989 MPa·m*$^{1/2}$*.*

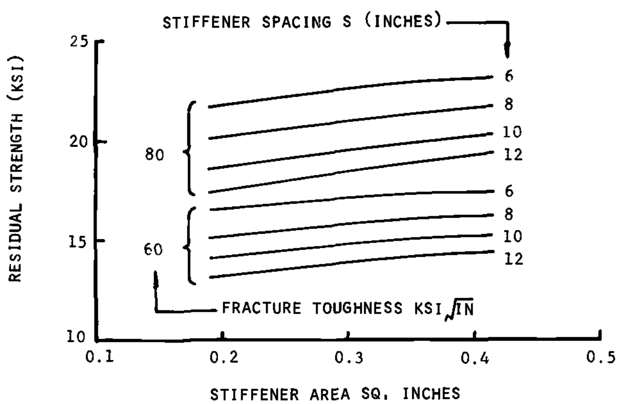

FIG. 20—*Effect of stiffener area and spacing on residual strength with skin fracture toughness 60 and 80 ksi·in.*$^{1/2}$ *and stiffener* F_{tu} *82 ksi where 1 ksi = 6.895 MPa, 1 in.*^{2} *= 645.16 mm*^{2}*, 1 in. = 25.4 mm, 1 ksi·in.*$^{1/2}$ *= 1.0989 MPa·m*$^{1/2}$*.*

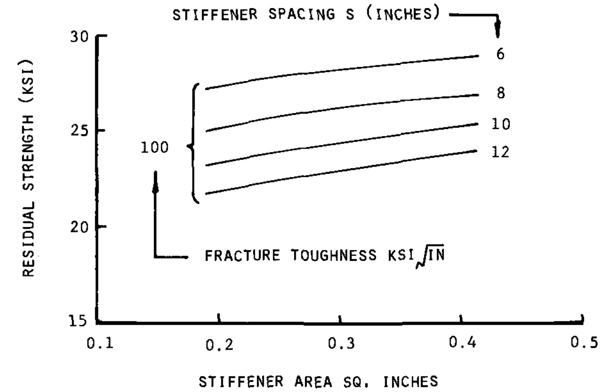

FIG. 21—*Effect of stiffener area and spacing on residual strength with skin fracture toughness 100 ksi·in.*$^{1/2}$ *and stiffener* F_{tu} *82 ksi where 1 ksi = 6.895 MPa, 1 in.*^{2} *= 645.16 mm*^{2}*, 1 in. = 25.4 mm, and 1 ksi·in.*$^{1/2}$ *= 1.0989 MPa·m*$^{1/2}$.

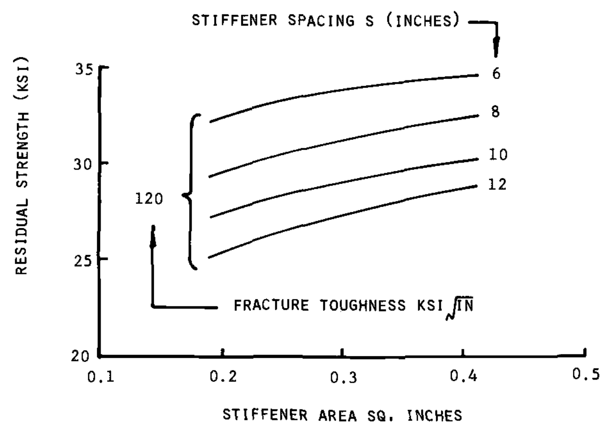

FIG. 22—*Effect of stiffener area and spacing on residual strength with skin fracture toughness 120 ksi·in.*$^{1/2}$ *and stiffener* F_{tu} *82 ksi where 1 ksi = 6.895, 1 in.*^{2} *= 645.16 mm*^{2}*, 1 in. = 25.4 mm, and 1 ksi·in.*$^{1/2}$ *= 1.0989 MPa·m*$^{1/2}$.

Stiffener Bending and Test Verification

When a crack propagates in a stiffened panel, as explained previously, load is transferred out of the cracked skin into the stiffening elements. Since transfer of this load takes place at the shear face of the attachment between the sheet and stiffener, which is usually some distance from the neutral axis of the stiffener, then stiffener bending takes place. The degree to which this stiffener bending effects overall residual strength is controversial within the fracture analysis community. It is my contention that stiffener bending should be accounted for, particularly for thinner skin gages and can easily be included as described in the section on displacement compatibility analysis development outlined in this paper. This contention results from experience gained during a considerable amount of testing of stiffened panels, the results of which, in many cases, are contained in the literature [*9, 10, 15, 16*].

Stiffener Bending in Curved Panel Testing

A fail-safe test was conducted on a large curved panel similar to the one illustrated by Figs. 32 and 33 of Ref *16*. A hat-section longeron was completely saw cut through and a circumferential crack made in the skin. During the course of propagating this skin crack, several applications of higher static loading were applied to simulate fail-safe conditions. Pressure loading, representative of cabin differential pressure, was applied and reached by hoop tension in the skin. Axial loads were applied, representative of the effects of pressure and fuselage inertia bending. The maximum axial P/A stress was 185.45 MPa (26.896 ksi), which because of Poisson's ratio effects, resulted in longeron axial stresses of 162.80 MPa (23.612 ksi) and skin axial stresses of 195.82 MPa (28.40 ksi). Finite-element analysis was conducted to determine longeron bending stresses as a function of skin crack size taking into account the difference between skin and longeron stresses resulting from Poisson's effect. The location of the longeron and skin saw cut was chosen at a point of inflexion in the longeron to avoid complication caused by longeron bending resulting from cabin pressure. Strain gages, located on inner and outer caps of one of the uncut crack arresting longerons, adjacent to the saw cut longeron, were monitored during the test. The results, plotted as a function of skin half crack length, are illustrated by Fig. 23. These results lead one to believe that stiffener bending needs to be accounted for in residual strength analysis.

Stiffener Bending in Flat Panel Testing

Fail-safe tests were conducted on large flat panels similar to that shown in Fig. 22 of Ref *9*. Skin cracks were propagated about a central intact frame after the center crack stopper had broken. Strain gage readings on the inner and outer caps of the center intact frame as a function of skin half crack length are shown in Fig. 24, correlated with finite-element analysis. Again, considerable bending in the frame, caused by transfer of load from the cracked skin, is illustrated. This result also leads one to the conclusion that stiffener bending should be accounted for in stiffened panel residual strength analysis.

Residual Strength Test Verification

Ample verification of analysis methods have been shown previously [*16*], but the need exists to re-emphasize the requirement to account for stiffener bending. Obviously this effect becomes more pronounced when the neutral axis of the stiffener material is farther away from the skin. This is illustrated by the case shown in Fig. 24, representing results for a fairly deep frame. In order to empha-

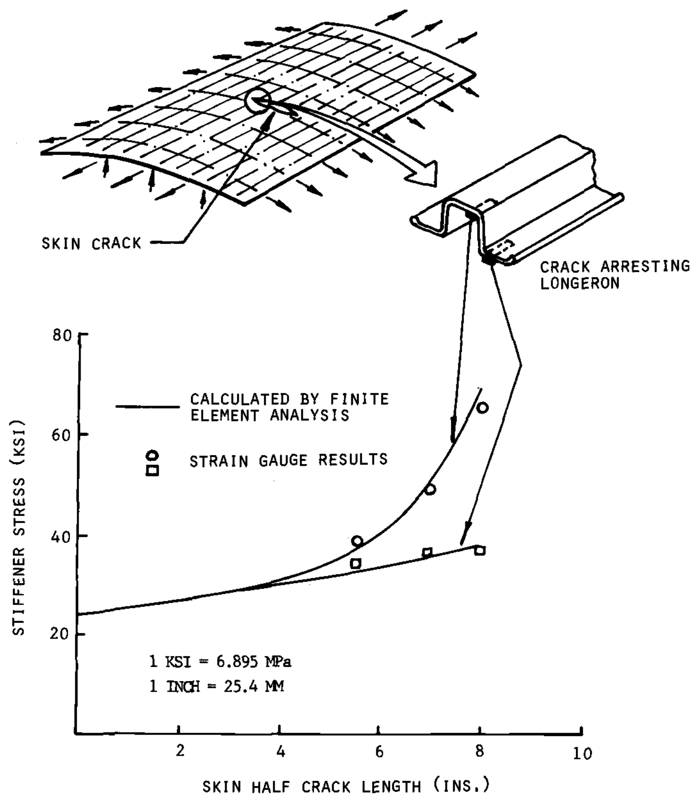

FIG. 23—*Uncut crack arresting longeron bending as a function of skin crack length.*

size the stiffener bending effect, two panel tests have been chosen where the stiffeners were comparatively shallow, that is, one with a 25.4-mm (1.0-in.) deep hat-section stiffener and one with a 23.88-mm (0.94-in.) tee-section stiffener. The stiffener section configurations are described as Configuration 6 and 9 in Fig. 11 of Ref *17*. It would be expected that these shallow sections would minimize the need to account for stiffener bending. Residual strength curves are shown for these two cases in Figs. 19 and 21, respectively, of Ref *16*. The analysis test correlation shown by these two figures, accounting for stiffener bending, is considered excellent. In order to emphasize the stiffener bending effect the displacement compatibility analysis for these two configurations has been repeated, but with stiffener bending effects removed. In other words, the computer runs were repeated with stiffener bending eliminated by inputting an extremely high value for stiffener inertia. The damage configurations are both three bay cracks with two broken stiffeners. The test panels were made from 2024-T3 skin 1.8-mm (0.071-in.) thick, and the stiffeners in both cases were 7075-T6 extrusions. The testing procedure was described in Ref *17*, and a photo-

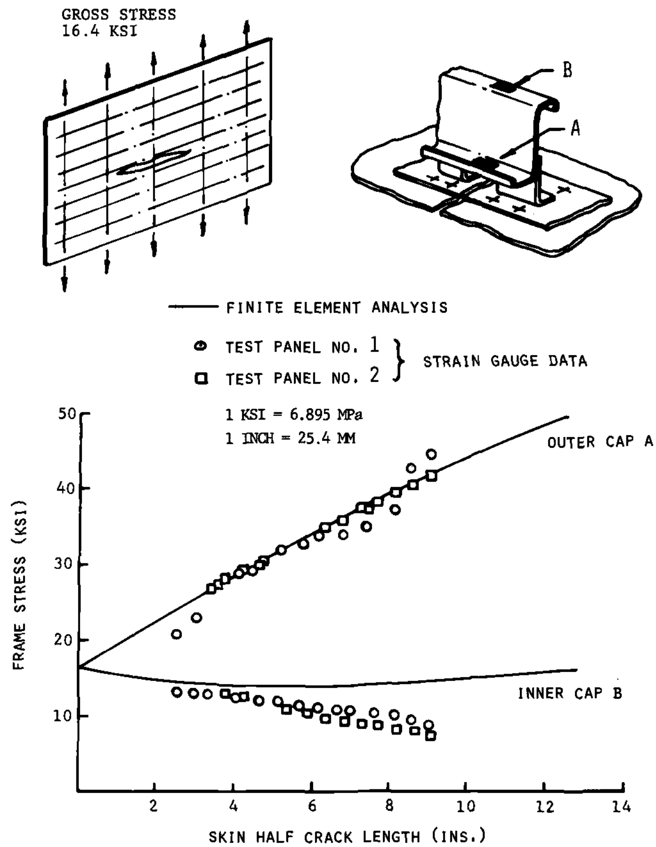

FIG. 24—*Center frame bending stresses as a function of skin half crack length.*

graph of the test setup is shown in Fig. 26 of this reference. A photograph of a failed panel, similar to the ones under discussion here, is shown in Fig. 22 of Ref *10*. After a certain amount of crack propagation testing, the skin cracks were extended to three bays, and two stiffeners were saw cut. Loading was increased in steps until failure took place. Figures 25 and 26 illustrate the difference in analysis predictions that would occur for the two assumptions where stiffener bending was accounted for or neglected. In the case of the hat-section stiffener, illustrated by Fig. 25, not accounting for stiffener bending would have liberally over predicted the failure gross stress by nearly 31%, where as accounting for stiffener bending underestimated the strength by only a little over 2%. In the case of the tee-section stiffener, accounting for stiffener bending correlates exactly with the test result. If stiffener bending were to be neglected the result would have been overestimated by 13%. The skin fracture toughness value used to correlate these test results was obtained from a fast fracture on a previous test on a panel with hat-section stiffeners. This configuration was a two bay crack with a single

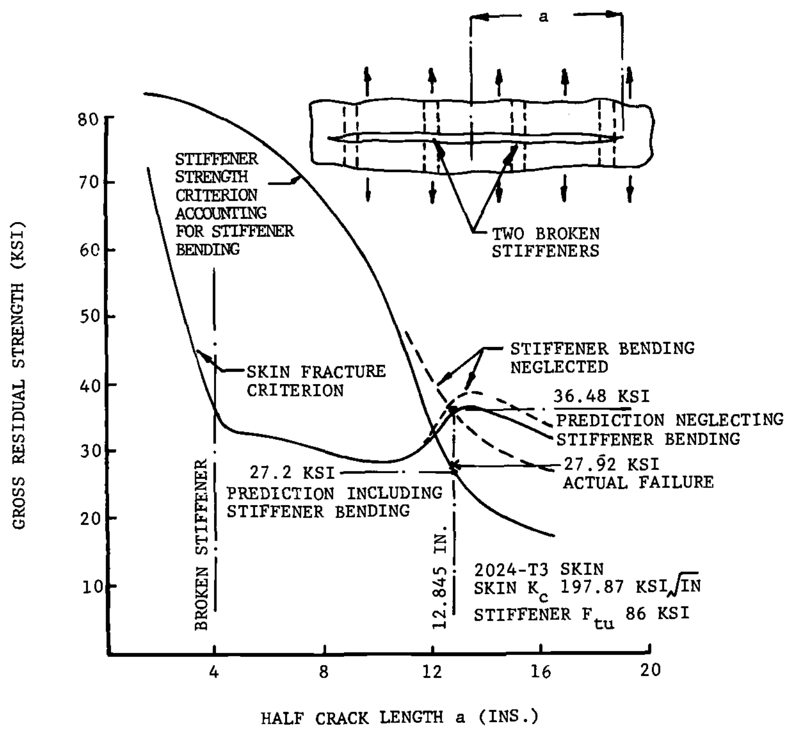

FIG. 25—*Analysis test correlation three bay crack with two saw cut stiffeners: small hat stiffeners—2024-T3 skin. 1 ksi = 6.895 MPa, 1 in. = 25.4 mm, and 1 ksi·in.$^{1/2}$ = 1.0989 MPa·m$^{1/2}$.*

failed central stiffener. Fast fracture had taken place at a gross stress of 271.0 MPa (39.304 ksi) with an average half crack length of 157.6 mm (6.205 in.). Displacement compatibility analysis for this configuration resulted in a value of β equal to 1.1. Using the secant panel width correction factor for a panel width of 1524 mm (60 in.) resulted in a skin plane stress fracture toughness of 217.44 MPa · m$^{1/2}$ (197.867 ksi · in.$^{1/2}$). This value was successfully used for several other analysis test correlation studies included in Ref *16*. The stiffener material strength values used in the two correlations illustrated by Figs. 25 and 26 were obtained from tensile coupons cut from the failed stiffeners subsequent to completion of all testing. The fact that neglecting stiffener bending would have been overestimated in one case by 31% and in a second case by 13% is sufficient evidence, in the opinion of this author, to account for these effects.

Rivet Strength Criteria

Failure criterion for the residual strength of cracked stiffened panels discussed so far in this paper has been limited to skin fracture and stiffener strength using linear theory. These failure criteria are illustrated by Fig. 14. Rivet failure in the

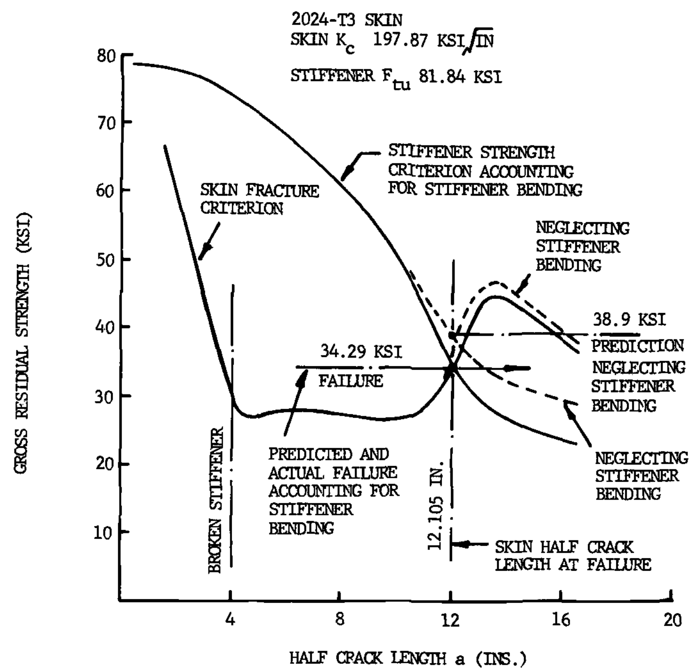

FIG. 26—*Analysis test correlation three bay crack with two saw cut stiffeners: large tee-stiffeners—2024-T3 skin. 1 ksi = 6.895 MPa, 1 in. = 25.4 mm, and 1 ksi·in.$^{1/2}$ = 1.0989 MPa·m$^{1/2}$.*

crack arresting stiffener has not been addressed. In all of the cracked stiffened panel residual strength correlations shown both in this paper and in Ref *16*, reasonable correlation has been possible without consideration being given to fastener failure. It has been suggested within the fracture analysis community that fastener failure such as unzipping cannot occur. This criterion will be addressed here.

Fastener Flexibility

The importance of accounting for the effects of fastener flexibility was addressed earlier during the analysis development. It is possible to illustrate the error in stress intensity factor that can be incurred when fastener flexibility is ignored. In order to illustrate this point an analysis, using the displacement compatibility approach, was conducted. The two bay crack with a broken central stiffener configuration was chosen. The analysis was conducted with and without fastener flexibility. The results are illustrated by Fig. 27. When the skin crack is short, the rigid fastener assumption causes the transfer of load into the cracked sheet to occur locally near the crack front causing a greater estimation of stress intensity factor than would otherwise be realized with a flexible fastener assumption. As the crack tip approaches the intact crack arresting stiffener the rigid fastener

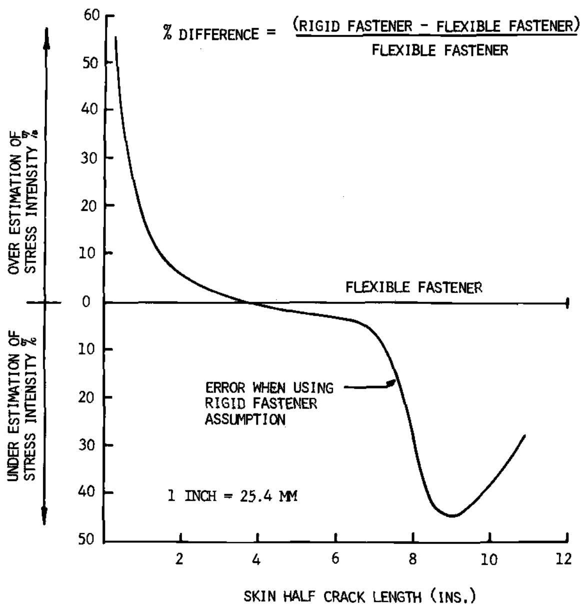

FIG. 27—*Error when skin to stiffener fasteners are assumed rigid.*

assumption causes a greater transfer of load to the stiffener, thus reducing the stress intensity factor more than would be experienced with the flexible fastener assumption. As indicated by Fig. 27, the error can be as high as 50%.

Fastener Shear Force

The most critical fastener in a cracked stiffened panel is usually the first fastener adjacent to the skin crack in the crack arresting stiffener. The load in this fastener is usually quite low until the skin crack crosses the intact stiffener, and then it increases rapidly. Figure 28 shows first fastener shear load per unit gross stress applied to the panel for a typical configuration. For this example the hat-section stiffener area was 205.29 mm^2 (0.3182 $in.^2$). The stiffener spacing was 203.2 mm (8.0 in.), and the skin thickness was 1.8 mm (0.071 in.). The center stiffener was assumed broken. When the skin crack is confined to two bays, the fasteners rarely create a problem. However, if the skin crack has a tendency to extend beyond the crack arresting stiffener, either during the arrest of a fast fracture or because of slow stable growth during load increase, then the first fastener failure criterion can become important.

Fastener Unzipping

Elastic displacement compatibility analysis predicts extremely high first fastener loads when the skin crack extends beyond the crack arresting member as

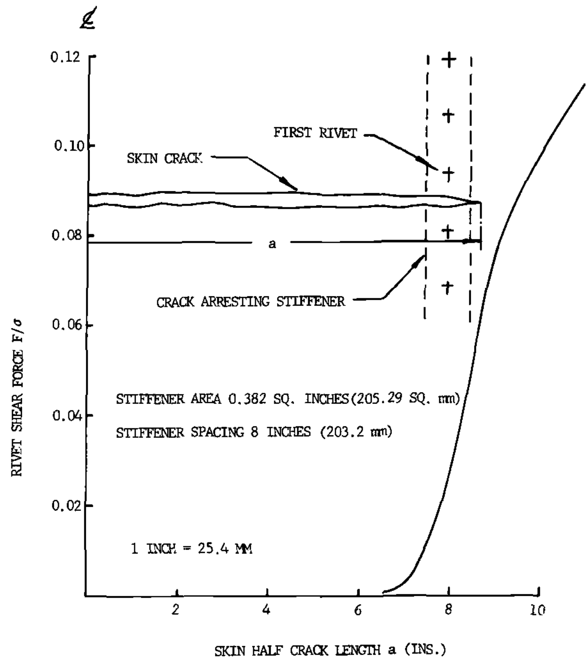

FIG. 28—*First rivet shear force.*

seen from Fig. 28. Yielding of this fastener will take place before its failure, thus allowing transfer of load to rivets farther away from the crack. Provided the crack extension beyond the crack arresting member is not excessive, and the gross panel stresses are not too high, small scale fastener yielding does not drastically effect the results, and elastic analysis may be acceptable. If, however, this is not the case then an elastic plastic analysis is usually required.

Probably the best way to illustrate fastener failure phenomenon is to review the results of a stiffened panel test where fastener failure (unzipping) in the crack arresting stiffeners actually precipitated panel failure. Figure 29 shows a stiffened panel containing a two bay skin crack extending beyond the intact crack arresting stiffener. The center stiffener had been initially saw cut. The panel was made from 2024-T3 skin, 1.8 mm (0.071 in.) thick, with 7075-T6 "hat-section" stiffeners, spaced 203.2 mm (8 in.) apart with a cross-sectional area of 352.97 mm^2 (0.5471 in.^{2}). The skin crack had been propagated beyond the intact crack arresting stiffener by cyclic loading. Static load was applied in increments and failure occurred at 274.0-MPa (39.74-ksi) gross area stress with a half crack length of 250.95 mm (9.88 in.). The rivets in both crack arresting members had sheared over the entire length of the panel (unzipping), indicating that failure was precipitated by fastener failure.

Elastic analysis, based on the displacement compatibility method described in this paper would not predict the failure stress correctly. A method was developed,

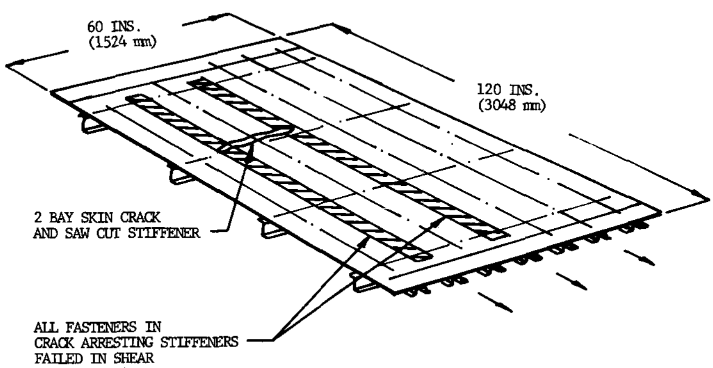

FIG. 29—*Fastener unzipping.*

based on displacement compatibility, which would make use of the previously developed elastic method but which would account for nonlinear shear displacement of the fastener.

Load displacement tests were conducted on simple lap splices placed back-to-back to cancel out bending. The stiffener crown thickness and material were simulated. The rivets were NAS 1097 DD 4.83 mm (0.19 in.) diameter. The resulting load displacement curve was simulated by a tri-elastic model as shown in Fig. 30.

The computer program, developed for the elastic analysis, was extensively modified to enable a fastener flexibility matrix, compatible with Fig. 30, to be generated. An elastic solution is generated initially based on the initial slope of the fastener displacement curve. This elastic slope can be determined using Eq 32. Each resulting fastener load is compared to the tri-elastic model shown in Fig. 30. The fastener flexibility matrix is then regenerated based on the appropriate slope of this model. A new solution is obtained based on the new fastener flexibility matrix. The crack-tip stress intensity factor obtained from the first solution is compared to that obtained from the second solution, and if the difference is greater than a set number, which can be adjusted, then the procedure is automatically repeated. A new fastener flexibility matrix is developed on each iteration. The iterative process continues automatically until the stress intensity factor between iterations drops below the specified value, and at this time a final solution at the input gross stress is output. The program is set to increase the applied gross stress by a certain amount, which can be varied, and a new set of solutions is obtained at the next stress level automatically.

The computer program was also modified to allow the rivets to be disconnected to simulate failure. A set of solutions is obtained with all rivets intact, and then with first and subsequent rivets failed. When all rivets are intact, the first rivet displacements are printed out. When the first rivet has been disconnected, the

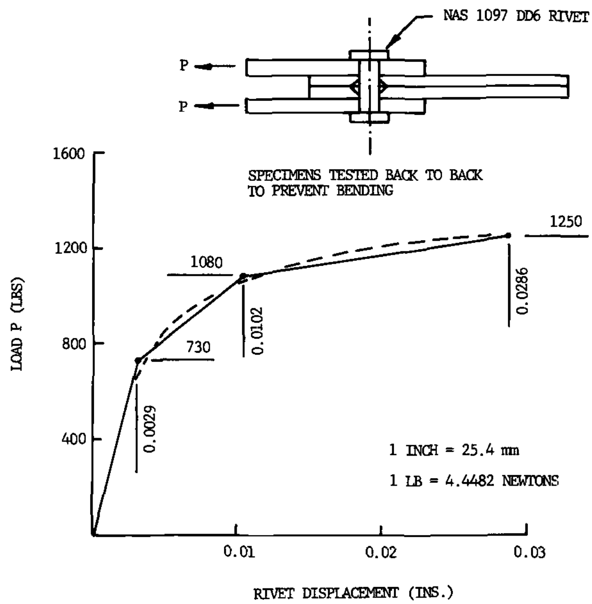

FIG. 30—*Tri-elastic model simulating rivet displacement.*

output includes the displacement of the second rivet. This process is continued until enough rivets have been disconnected. For the test panel described, the rivet displacements are shown in Fig. 31. This figure illustrates fastener displacement as a function of gross applied panel stress when the skin half crack length is 250.95 mm (9.88 in.). Four curves are shown, each with a different number of rivets failed. The curve representing zero fasteners failed indicates the displacement of Fastener 1. The curve representing one fastener failed indicates the displacement of Fastener 2. The vertical line AB on Fig. 31 represents the rivet failure displacement obtained from the simple splice tests illustrated by Fig. 30. The points at which this line crosses the curves, represented by dots on Fig. 31, can be cross plotted to provide a curve of gross panel stress versus number of rivets failed when the skin half crack length is 250.95 mm (9.88 in.). This curve is shown on Fig. 32. Point A represents the gross panel stress at which the first rivet will fail based on the analysis. Point B represents the gross stress at which the second rivet will fail and so on. This curve represents data when the skin half crack length is 250.95 mm (9.88 in.). The reason for the increase in allowable stress for rivet failure is that the second and third rivets are farther away from the skin crack and therefore less severely loaded even though a transfer of load occurs into these rivets.

As rivet failure occurs, the stiffener becomes less effective in reducing the crack-tip stress intensity factor. Figure 33 shows crack-tip stress intensity factor versus gross panel stress. The upper curve represents the case when all rivets are intact. The next curve lower, represents the case when the first fastener has failed

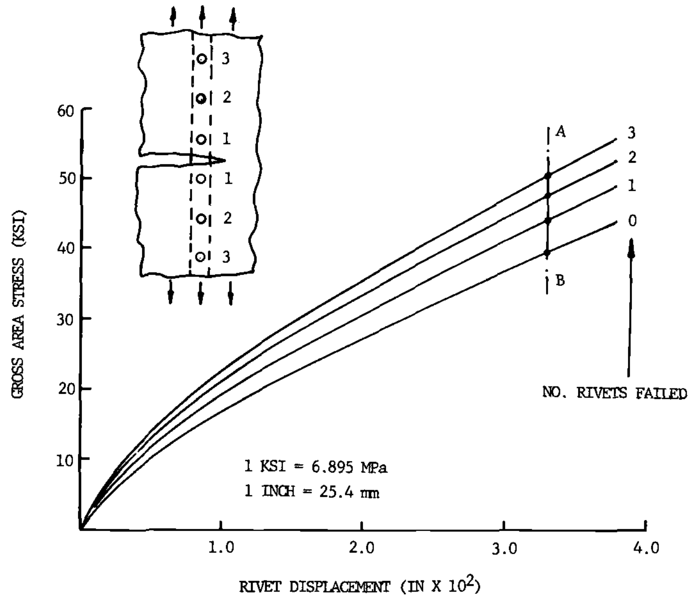

FIG. 31—*Rivet displacement with skin half crack length 250.95 mm (9.88 in.) and varying numbers of rivets failed.*

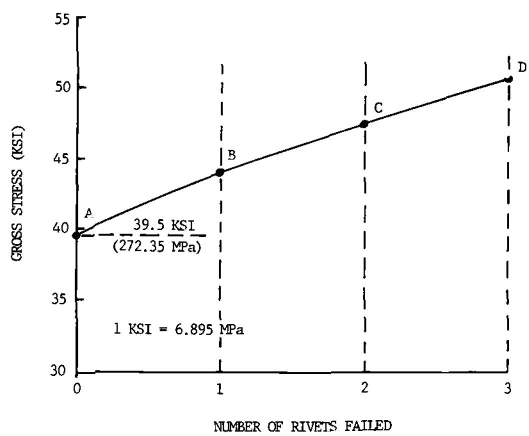

FIG. 32—*Gross stress at which rivet failure displacement occurs half crack length 250.95 mm (9.88 in.).*

and so on. The vertical line AB, drawn through the curves represents the critical stress intensity, which for the 2024-T3 material with grain normal to the crack direction is 217.44 MPa $\cdot$ $m^{1/2}$ (197.87 ksi $\cdot$ $in^{1/2}$), based on the fast fracture previously discussed. The points at which the vertical line crosses the curves can be cross plotted to form a curve of allowable gross stress from a skin fracture viewpoint as a function of number of rivets failed when the skin half crack length

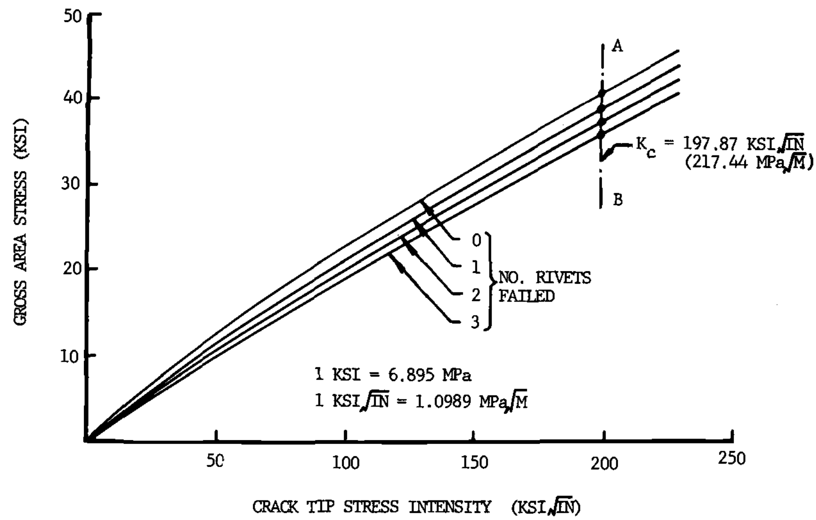

FIG. 33—*Crack-tip stress intensity factor with skin half crack length 250.95 mm (9.88 in.).*

is 250.95 mm (9.88 in.). This curve is illustrated by Fig. 34. Point A on this curve represents the gross panel stress at which skin fast fracture will occur with all rivets intact. After failure of the first rivet, the stiffener becomes less effective, and the skin crack-tip stress intensity factor increases, reducing that allowable from a skin fracture viewpoint to Point B and so on. Figures 32 and 34 can be combined to form a residual strength curve as shown in Fig. 35. This diagram represents the following scenario. Gross stress on the panel is increased, and at

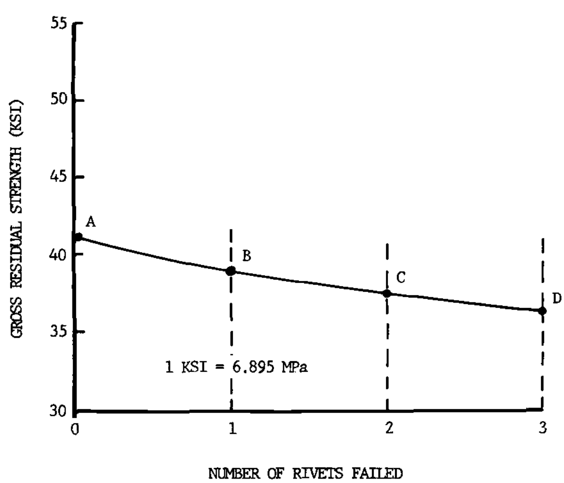

FIG. 34—*Gross stress at which skin fast fracture will occur as a function of number of failed rivets where half crack length is 250.95 mm (9.88 in.).*

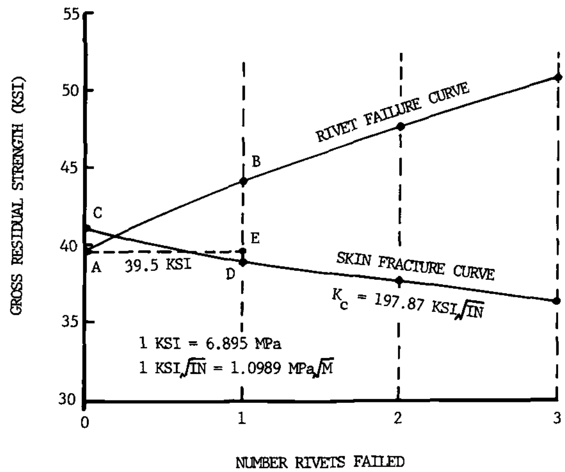

FIG. 35—*Residual strength diagram with half crack length 250.95 mm (9.88 in.).*

272.35 MPa (39.5 ksi) the first rivet fails at Point A. Immediately, the panel allowable based on rivet criteria increases to Point B because the second rivet is farther away from the crack. However, because the first rivet has failed, the stiffener is less effective and the allowable, based on skin fracture criterion, has reduced to Point D. This is below the stress level applied to the panel, thus the skin crack suddenly extends, that is, fast fractures. However, Fig. 35 does not illustrate the unzipping phenomenon that occurred on the test because this figure is based only on a skin half crack length of 250.95 mm (9.88 in.). When fast fracture occurs, the crack suddenly extends and the rivet strength criteria immediately reduces as illustrated by Fig. 36. In fact, by the time the skin crack reaches a half crack length of 304.8 mm (12.0 in.), several rivets have failed since the stress level is above Points A, B, C, and D, which represent panel allowable from a rivet strength standpoint at a skin half crack length of 304.8 mm (12.0 in.).

As the skin crack rapidly extends the rivets fail in sequence. By plotting rivet displacement against crack length for each rivet failed condition, it is possible to obtain a cross plot of crack length versus number of rivets failed. This is illustrated by Fig. 37. A vertical line AB, at the rivet failure displacement, is drawn to intersect each curve at the points shown. These points are then plotted to produce a curve of the number of rivets failed versus half crack length as shown on Fig. 38. Figure 31 through 38 illustrate the rivet unzipping phenomenon that actually occurred on the test panel described.

The analysis described here predicted failure at a gross stress of 272.35 MPa (39.5 ksi) as indicated on Fig. 35. The actual failure stress was 273.73 MPa (39.7 ksi).

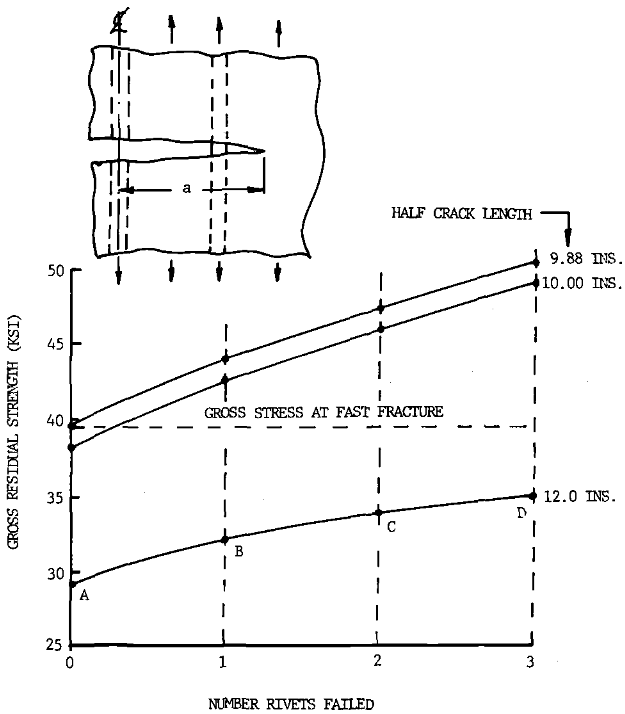

FIG. 36—*Rivet failure criterion as effected by crack extension where 1 ksi = 6.895 MPa and 1 in. = 25.4 mm.*

Conclusions

An analysis method to determine crack-tip stress intensity factors, stiffener stress concentration factors, and residual strength is presented based on the displacement compatibility method. The damage condition considered is a two bay skin crack with a broken central stiffener. It is recommended that all basic aircraft structure be designed for this capability at limit load. The method is ideally suitable for parametric studies during the early design phase of an aircraft structural development because of comparatively low computer costs. A sample parametric study is included to illustrate the method. The following conclusions, resulting from the parametric study, can be stated.

- The stress intensity factor is higher than for an unstiffened panel until the crack tip approaches the intact crack arresting stiffener.
- Considerable bending occurs in the outer crack arresting stiffener as the skin crack length increases.
- Residual strength for the two bay crack configuration is a function of both skin fracture and stiffener strength criteria.
- The residual strength for the configuration considered reduces with reducing stiffener area and increases with reduction in stiffener spacing.

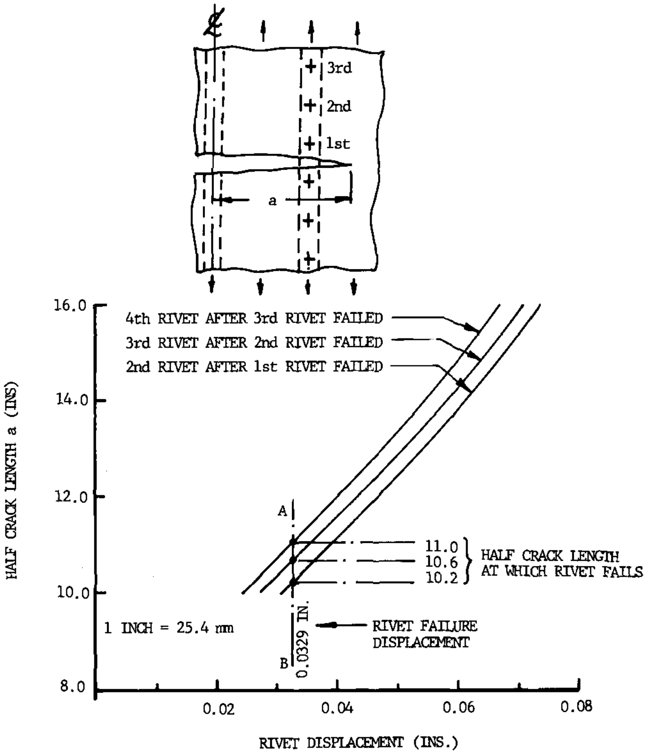

FIG. 37—*Rivet displacement versus half crack length for various failed fasteners where gross stress is 275.8 MPa (40 ksi).*

- The residual strength increases with increasing skin fracture toughness.
- The residual strength increases with stiffener material strength if the stiffener strength curve intersects the skin fracture curve.

It is shown that consideration must be given to stiffener bending when calculating residual strength. Test data are included, which show that lack of consideration for stiffener bending can result in over estimation of strength by as much as 30%.

Test data included indicate the displacement compatability approach provides accurate results.

It is shown that lack of consideration of rivet flexibility can result in overestimation of the stress intensity factor when skin cracks are small and an underestimation when the skin crack approaches the crack arresting stiffener.

When skin cracks pass over the crack arresting stiffener, the rivet shear forces become excessively high. Provided the skin crack does not extend beyond the stiffener and stress levels are not high, elastic analysis gives good correlation.

When skin cracks extend beyond the crack arresting member and stresses are high, elastic analysis will not provide good correlation. A method of analysis is

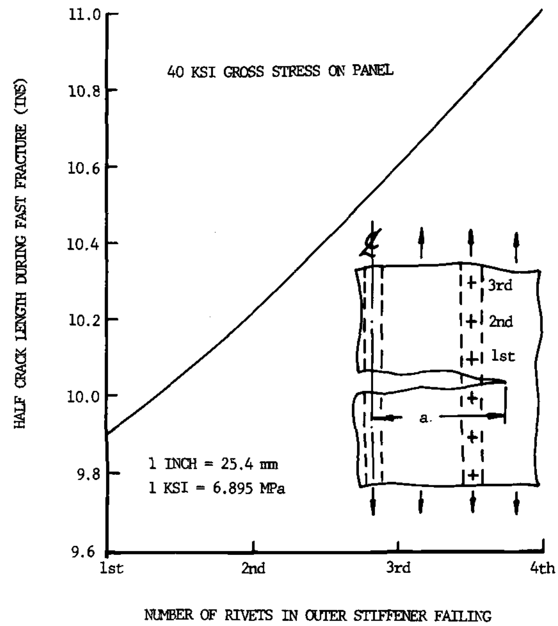

FIG. 38—*Number of rivets failing as a function of crack length during the fast fracture process (unzipping).*

described based on nonlinear fastener displacement, which can provide good correlation for this condition.

A test is described in which rivet unzipping precipitated panel failure. Elastic-plastic analysis described herein was able to predict the mode of failure and failure gross stress.

References

[1] Romualdi, J. P., Frasier, J. T., and Irwin G. R., "Crack-Extension-Force Near a Riveted Stiffener," NRL Report 4956, U.S. Navy, Washington, DC, Oct. 1957.
[2] Sanders, J. L., Jr., "Effect of a Stringer on the Stress Concentration Due to a Crack in a Thin Sheet," NASA TR R-13, 1959, National Aeronautics and Space Association, Washington, DC, (supersedes NACA TN 4207).
[3] Romualdi, J. P. and Sanders, P. H., "Fracture Arrest by Riveted Stiffeners," AFOSR-TR-60-174, U.S. Air Force, Dayton, OH, Oct. 1960.
[4] Poe, C. C., Jr., "The Effect of Riveted and Uniformly Spaced Stringers on the Stress Intensity Factor of a Cracked Sheet," *Proceedings of the Air Force Conference on Fatigue and Fracture of Aircraft Structures and Materials,* AFFDL-TR-70-144, U.S. Air Force, Dayton, OH, Dec. 1969, pp. 207–214.
[5] Vlieger, H., "Residual Strength of Cracked Stiffened Panels," NLR Report 71004U, Jan. 1971.
[6] Poe, C. C., Jr., "Stress-Intensity Factor for a Cracked Sheet with Riveted and Uniformly Spaced Stringers," NASA TR R-358, National Aerospace Laboratory, Amsterdam, Netherlands, May 1971.
[7] Poe, C. C., Jr., "The Effect of Broken Stringers on the Stress Intensity Factor for a Uniformly Stiffened Sheet Containing a Crack," NASA TM X-71947, NASA Langley Research Center, Hampton, VA, 1973.

[8] Swift, T., "The Effects of Fastener Flexibility and Stiffener Geometry on the Stress Intensity in Stiffened Cracked Sheet," *Prospects of Fracture Mechanics,* Noordhoff International Publishing, Leydon, Netherlands, 1974, pp. 419–436.
[9] Swift, T., "The Application of Fracture Mechanics in the Development of the DC-10 Fuselage," *Fracture Mechanics of Aircraft Structures,* AGARD-AG-176, North Atlantic Treaty Organization, London, England, 1974.
[10] Swift, T., "Development of the Fail-Safe Design Features of the DC-10," *Damage Tolerance in Aircraft Structures, ASTM STP 486, American Society for Testing and Materials,* Philadelphia, 1970, pp. 164–214.
[11] Westergaard, H. M., "Bearing Pressures and Cracks," *Journal of Applied Mechanics,* Vol. 6, No. 1, June 1939, p. A49.
[12] Love, A. E. H., *A Treatise on the Mathematical Theory of Elasticity,* Fourth Ed., Dover Publications, 1944, p. 209.
[13] Irwin, G. R., "Analysis of Stresses and Stains Near the End of a Crack Traversing a Plate," *Journal of Applied Mechanics, Transactions of the American Society for Mechanical Engineers,* Vol. 24, Sept. 1957, pp. 361–364.
[14] Paris, P. C., *Application of Muskhelishvili's Method to the Analysis of Crack Tip Stress Intensity Factors for Plane Problems, Part III,* Lehigh University, Bethlehem, PA, 1960.
[15] Swift, T., "Damage Tolerance Analysis of Redundant Structures," *Fracture Mechanics Design Methodology,* AGARD-LS-97, North Atlantic Treaty Organization, London, England, Jan. 1979, pp. 5–1.
[16] Swift, T., "Design of Redundant Structures," *Fracture Mechanics Design Methodology,* AGARD-LS-97, North Atlantic Treaty Organization, London, England, Jan. 1979, pp. 9–1.
[17] Swift, T. and Wang, D. Y., "Damage Tolerant Design-Analysis Methods and Test Verification of Fuselage Structure," Air Force Conference on Fatigue and Fracture of Aircraft Structures and Materials, AFFDL-TR-70-144, U.S. Air Force, Dayton, OH, 1969.

Royce G. Forman[1] and Tianlai Hu[2]

Application of Fracture Mechanics on the Space Shuttle

REFERENCE: Forman, R. G. and Hu, T., "**Application of Fracture Mechanics on the Space Shuttle,**" *Damage Tolerance of Metallic Structures: Analysis Methods and Applications, ASTM STP 842,* J. B. Chang and J. L. Rudd, Eds., American Society for Testing and Materials, 1984, pp. 108–133.

ABSTRACT: During the design stages of the shuttle orbiter, fracture-mechanics concepts were applied extensively to the highly stressed areas of the structure. This was the first space program to require a comprehensive fracture mechanics approach to prevent structural failures from crack or crack-like defects. As anticipated, some difficult problems were encountered. This paper briefly describes some of them together with the procedure used for fracture control on the orbiter. It is believed that the principles and methods as presented herein can serve as an example of fracture control for aerospace and other industries.

KEYWORDS: flaw detection, shot peening, crack propagation, space shuttle, fracture mechanics, nondestructive evaluation, radiographic inspection, Collipriest equation, Paris and Forman equations, crack opening displacement

Nomenclature

a, a_i	Crack depth, initial crack depth
C	Crack-growth rate coefficient
c	Half-crack length
C_1	Front surface correction
da/dN	Crack-growth rate per cycle
E	Young's modulus
K_c	Critical stress intensity for crack growth
K_{th}	Sustained load stress intensity factor threshold
ΔK_0	Threshold stress intensity range
ΔK	Applied stress intensity range

[1]Aerospace engineer, Lyndon B. Johnson Space Center, Code ES5, Houston, TX 77058.
[2]Member of technical staff, Space Transportation and System Group, Rockwell International, 12214 Lakewood Boulevard, Downey, CA 90241.

M_2	Back-surface correction
n, p, q	Crack-growth rate exponents
R	Stress ratio (minimum stress/maximum stress)
δ	Crack opening displacement
γ	Poisson's ratio
σ	Stress
Φ	Complete elliptical integral of the second kind

Introduction

The space shuttle is the first space program to incorporate a comprehensive fracture-mechanics approach to prevent structural failures resulting from crack or crack-like defects. The initial efforts in developing a fracture control program for the shuttle began with several government/industry working group meetings in 1971 and 1972. The program's detailed requirements were developed over a subsequent two-year period by National Aeronautics and Space Administration (NASA) and the shuttle's prime contractor, Rockwell International. This effort resulted in the document, *Space Shuttle Orbiter Fracture Control Plan* [*1*], which specified the criteria and approach for preventing catastrophic structural failures caused by the growth of crack-like defects during the 100-mission orbiter life.

This paper presents the main points of the space shuttle fracture-control program and, in particular, application of fracture mechanics in this effort. The fracture-control program was unique. There was no precedent for such usage on a space system, and there was the requirement of safe-life verification for a winged vehicle designed for only 100 launches and landings. Another consideration was the planned production of five flight vehicles. Orbiter test verification for safe life would have been relatively costly (in terms of total program costs) compared to similar verification tests on military or commercial production programs.

Discussion of the application of fracture mechanics on the shuttle will be separated into five topics: (1) selection of fracture-critical parts, (2) flaw-detection capability, (3) flaw-growth computer analysis, (4) special test programs, and (5) proposed development tasks for payload fracture-control analysis. The topics will be of interest to both experienced fracture-control analysts and to inexperienced analysts interested in examples of fracture-control problems.

Selection of Fracture-Critical Parts

The main criterion for selection of fracture-critical parts is whether the failure of a part by growth of a crack-like defect will be fail-safe or cause loss of the vehicle. If the possibility of loss of vehicle exists, a safe-life fracture-mechanics analysis is required. The selection logic and fracture control procedures contained in the shuttle orbiter fracture control plan are summarized in Fig. 1. The solid rocket booster (SRB), main engine, and external tank have similar but individual plans.

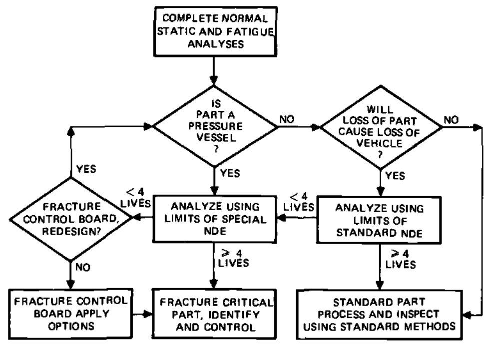

FIG. 1—*Selection logic for fracture-critical parts on the space shuttle orbiter.*

The selection logic procedures in Fig. 1 must be applied to the primary airframe structure and other critical structural parts. Since the shuttle orbiter primary structure is typical of conventional aircraft design, selection of critical parts is similar to aircraft-type damage tolerance assessments. The parts chosen for the fracture analysis include many nonairframe structural parts. Examples of these are turbine wheels, landing gears, actuators, pressure vessels, and hydraulic and flight control systems.

Pressure vessels were a major part of the fracture-control effort because they were automatically designated as fracture critical. More than 50 permanently installed pressure vessels are on each vehicle (Fig. 2) along with a number of carry-on-type bottles. Fracture control of pressure vessels was also complicated by the need to prevent leakage as well as burst failures. Examples of critical

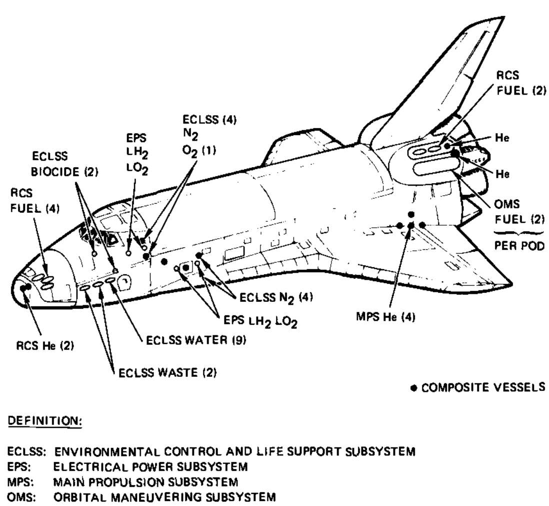

FIG. 2—*General locations of pressure vessels for space shuttle orbiter systems.*

leakage-type failures are those from a monomethylhydrazine fuel tank or from a nitrogen tetraoxide tank, which furnishes propellants for the orbital manuevering system.

Following the logic diagram of Fig. 1, the safe crack-growth life is computed, and for any candidate fracture-critical part that has less than four lives (for example, 4 × 100 missions) various options can be applied. The options, in their approximate order of relevance for disposition of a part, are the following.

1. Conduct more precise load, stress, and spectrum analyses.
2. Monitor structural or system testing to obtain refined loads.
3. Verify safe-life with fracture-mechanics-oriented component tests.
4. Apply specially designed inspection procedures to disclose smaller flaws.
5. Apply periodic reinspection or replacement.
6. Apply stress-intensity factor reduction methods such as shot peening.
7. Wave requirements, where specifically justified, such as improbability of certain flaw orientations based on a review of manufacturing processes.
8. Redesign part according to fracture-mechanics recommendations.

Nondestructive Evaluation Capabilities

In the Apollo program, fracture-mechanics analyses were largely restricted to the safe-life verification of pressure vessels. Proof-test logic was used to determine the criticality of defects that may have been present at the start of service. The approach was effective for prevention of catastrophic rupture in relatively brittle pressure-vessel materials and for single-mission operation where a proof to operating stress ratio of 1.2 was sufficient. On the shuttle, however, except for the SRB, proof-test logic was not used for flaw screening on any component, including pressure vessels, because of the requirements for longer safe-life and leakage prevention. In particular, the use of proof testing for leakage prevention was not applicable because short or circular shaped flaws in the thin-gage type pressure vessels were not fracture critical at proof stress levels.

After it was recognized that proof-test logic could not meet the orbiter flaw detection requirements, a number of NASA, Rockwell, and other contractor test programs were initiated to develop quantitative nondestructive evaluation (NDE) procedures. The programs used mostly flat panels of aluminum with small surface-type fatigue grown cracks where the starter flaws were removed. Integrally stiffened panels were included in one contractor program, and one NASA program included welded titanium panels.

More than 10 000 data points were obtained from these test efforts, and statistical methods were used to analyze the flaw-detection results. A comprehensive assessment of the data, including a significant amount of Air Force generated data, is reported in Yee et al [2].

A further evaluation of the data from the shuttle-related programs revealed that some inspectors consistently detected smaller defects than other inspectors. Also, specific methods or equipment improved the sensitivity of the NDE. Thus, two categories of NDE capability were established, standard NDE and special NDE. Both were statistically defined for a 90% probability of detection with 95% confidence.

Inspectors certified to Level II of Military-Standard (MIL-STD)-410, working to normal aerospace and military specifications, have been determined to be capable of detecting the standard NDE size flaws given in Table 1. The increased requirements for special NDE involve certification of individual inspectors by demonstrating the 90/95 statistics on a set of test panels and the use of part-specific inspection procedures. A detailed review of the development of the two categories of NDE for radiographic inspection is given by Sugg [*3*].

The flaw sizes in Table 1 also apply to holes in rod ends and clevis-type fittings where the holes are inspected with the pins removed. Fastener-type holes are often not inspected for flaws, particularly in panels fabricated by machines that drill holes and install fasteners in a single production sequence. In general, the Air Force recommended initial flaw sizes for fastener holes are assumed. These initial flaw sizes are 0.254- and 0.127-cm (0.10- and 0.05-in.) radial corner cracks for drilled and reamed holes, respectively. For material thicknesses less than or equal to these values, a through crack of the same length is used. Holes with driven rivets are assumed to have initial 0.0127-cm (0.005-in.) radius corner flaws. Pins and mechanical fasteners are assumed to be free of flaws.

Safe-Life Analysis

The fatigue flaw-growth analyses on the shuttle orbiter by Rockwell and its subcontractors were conducted with the FLAGRO computer program. The program was first developed by G. A. Vroman for analysis of the B-1 aircraft. Its original advantage, which has been retained, was the efficient numerical integration technique of specifying the crack-growth increment size and thereby varying the fatigue cycle increment size.

The current version of the computer program, FLAGRO 4, has been significantly modified from the original version. Some of the particular features added to the program for shuttle analysis are

TABLE 1—*NDE capabilities.*[a]

Inspection Method	Flaw Type	Standard NDE	Special NDE[b]
Penetrant or magnetic particle	surface flaw (depth × length)	0.075 × 0.150 in. or equivalent area	0.025 × 0.050 in. or equivalent area
Ultrasonic	embedded flaw (diameter)	0.100 in.	0.047 in.
Radiographic	surface or embedded (depth × length)	70% thickness × 140% thickness (minimum length = 0.150 in.)	60% thickness × 120% thickness (minimum length = 0.050 in.)

[a]1 in. = 2.54 cm.

[b]Must be demonstrated with 90/95 statistics.

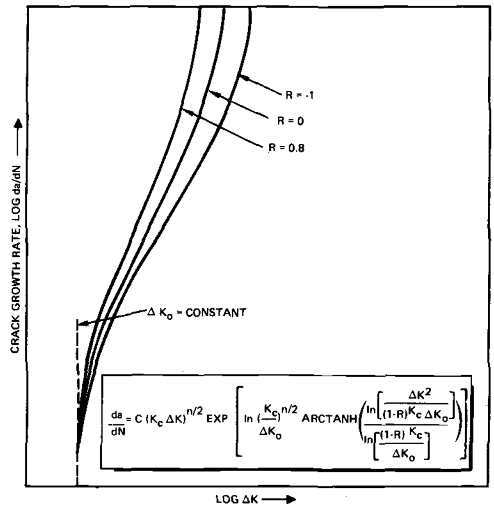

FIG. 3—*Collipriest crack-growth rate model.*

(1) use of the Collipriest [*4*] or inverse hyperbolic tangent fatigue crack-growth rate equation, which accounts for crack-growth threshold behavior,

(2) two-dimensional crack-growth model [*5*] that predicts flaw growth independently at the major and minor axis of elliptically shaped cracks,

(3) check for failure of a part-through crack in the mode of a through crack when net ligament yielding occurs as proposed by Orange et al [*6*],

(4) the automatic transfer of a part-through crack to a through crack when breakthrough occurs, and

(5) numerous cases of through and part-through crack solutions, including both open and pin-loaded holes.

The Collipriest equation was selected for shuttle orbiter analysis because it was considered to be the most accurate at the time. The form of the equation and the shape of the growth-rate curve is shown in Fig. 3. The improved accuracy of the inverse hyperbolic tangent equation compared with the Paris and Forman equations for fitting a wide range of aluminum and titanium data is reported by Davis and Fedderson [*7*].

The empirical parameters n, C, K_c, and ΔK_0 in Collipriest's equation were mostly obtained from compact tension specimen tests of different materials conducted by Rockwell. The test data generally covered the range of 2.5×10^{-8} to 2.5×10^{-4} m/cycle (10^{-6} to 10^{-2} in./cycle) and for an R value of 0.1. The crack lengths were determined by compliance methods. The test procedures generally agreed with current ASTM recommendations for fatigue crack-growth testing, particularly with regard to the maximum net section stresses.

For most of the material-environment combinations requiring crack-growth analysis, the fitted parameters were programmed into FLAGRO for easy input.

These materials, including the fitted parameters, are listed in Appendix A.

All fatigue stresses on the shuttle are variable amplitude, most of which occur from random-type loading. Since ΔK_0 is significantly increased for this type of fatigue spectrum, and since according to shuttle policy, no retardation calculations are allowed, results of the safe-life analysis are considered to be generally conservative.

The safety factor of four required for the safe-life analysis was selected to account for typical scatter in fatigue-crack-growth-rate data. The factor was determined after a statistical study on several different materials. A single variable analysis of the growth-rate constant C indicated that C multiplied by four was approximately equal to a 2σ variation and adequately bounded the growth-rate data. Also, comparisons of life predictions with numerous cycles to failure tests have always shown that the factor of four was conservative.

The fracture-mechanics analysis of the shuttle main engine was conducted with a different computer program than FLAGRO because different assumptions were required. The primary complication in the engine analysis was that safe life had to be determined for material fatigue loaded in high-pressure gaseous hydrogen environments. All high-strength metals, particularly heat-resistant alloys, are susceptible to environmentally accelerated crack-growth in this environment. The fatigue-crack-growth rate for this condition could not be modeled with the Collipriest equation, or any other equation, for a single fit over a wide range of data. A special computer program was developed by G. A. Vroman where spline fits to the Paris equation were used. The crack-growth-rate data were obtained from compact tension specimens loaded with a simulated 8.73-min engine operation cycle. The description of the cycle is shown in Fig. 4. Typical growth-rate results are shown in Figs. 5 and 6.

Special Test Programs

As mentioned, most of the crack-growth data were obtained by Rockwell for the orbiter and main engines. Some data for 2219-T87 aluminum weld and parent metal were obtained by the external tank contractor. The Johnson Space Center

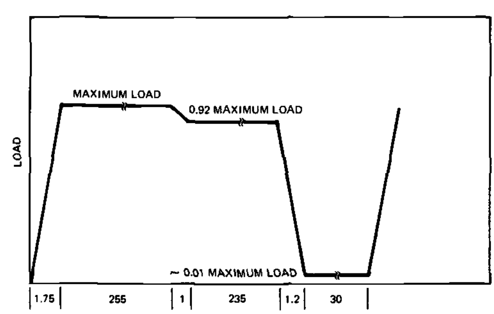

FIG. 4—*Simulated space shuttle main engine load-time cycle for crack-growth rate tests.*

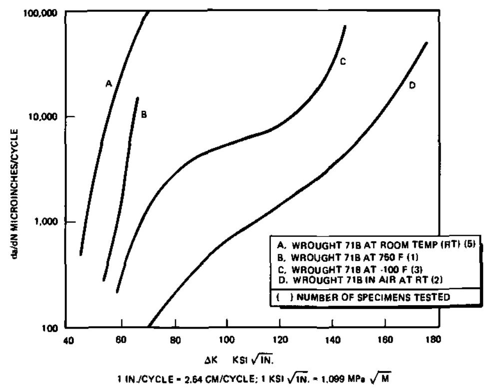

FIG. 5—*Crack-growth rate or Inconel 718 in 34474-kPa (5000-psi) hydrogen at various temperatures.*

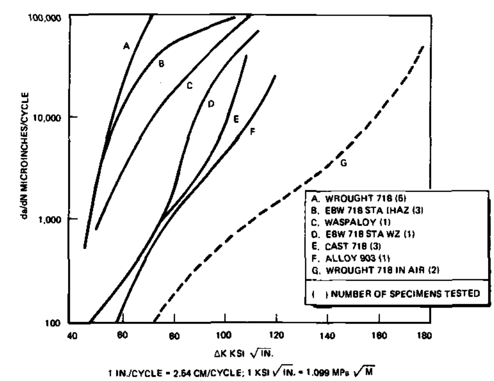

FIG. 6—*Crack-growth rate for main engine materials in 34474-kPa (5000-psi) hydrogen at room temperature.*

also conducted numerous fracture-mechanics test programs, both to obtain crack-growth data and to study special options for increasing the safe life of fracture-critical parts.

This section will describe several of the more unusual fracture-mechanics test programs conducted at the Johnson Space Center. These programs were unusual because of special test requirements, such as specimen design, environment, or because of the approach used in solving a fracture-control problem.

Probably the most difficult tests conducted were those on superalloys tested in high-temperature air or decomposed hydrazine. In another test, an unusual specimen design was used for the cycles to leak tests of thin aluminum liner material of a composite overwrapped pressure vessel. One of the most developmental efforts was correlation of radiographic flaw detection in overwrapped pressure vessels with flaw opening displacement. All of these test programs will be discussed in detail in the subsequent sections.

Enhancement of Radiographic Flaw Detection

Radiographic inspection is required for detecting flaws in the girth welds of Kevlar overwrapped pressure vessels. Figure 7, a drawing of a typical overwrapped pressure vessel, shows the required double-wall radiographic technique. The membrane areas of the metal liners are dye-penetrant inspected but not radiographic inspected before welding.

After welding and overwrapping are completed, the vessels are pressurized to give an approximately 3% permanent strain in the metal liners. This causes residual stresses that are slightly compressive in the girth welds and highly compressive in the membrane areas.

Testing and analysis have shown that for all overwrapped titanium vessels a special NDE size flaw in the liner membrane will withstand the 400-mission life before breakthrough, even including the sizing cycle. However, an assumed flaw 70% through the thickness of the girth weld did not have sufficient safe life, and improved inspection methods were required to alleviate the high expense of periodically removing the vessels for reinspection.

The first attempt to improve flaw detectability was to determine the capability of the sizing operation to screen weld flaws. Cross-weld specimen coupons were machined from the qualification weld ring of a Ti-6A1-4V titanium liner, fatigue-precracked, and pulled to failure. These tests indicated that a semicircular surface flaw of less than 70% through the thickness would not be screened. The approach, therefore, was not an improvement over radiographic inspection.

An alternate approach that was studied did show useful results. The approach was to radiographically inspect welded specimens when they were stressed in tension to open up the flaws. An earlier published work [8] showed that opening up cracks in specimens by applying bending loads significantly improved flaw detection by ultrasonic methods. The same concept was felt to be applicable to an improvement in radiographic inspection.

To correlate detectable flaw-size with crack opening displacement, an equation was needed to calculate the opening displacement of a deep surface flaw in a plate

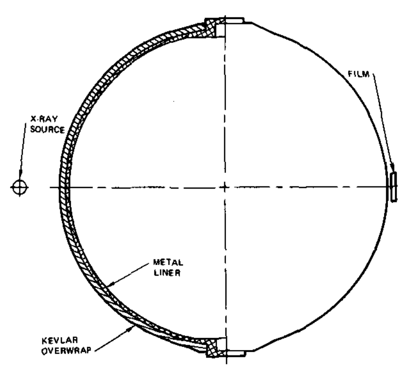

FIG. 7—*Configuration for double-wall radiographic technique for overwrapped pressure vessels.*

loaded in tension. No precise solution for this problem was known, so an approximate solution was determined. The form of the approximate solution was assumed to be

$$\delta = \{[4(1 - \gamma^2)/E](\sigma a/\Phi)\}\, C_1\, M_2 \qquad (1)$$

where the terms in braces are the Green and Snedded [*9*] embedded flaw solution, C_1 is the free-surface correction factor for an edge crack [*10*], which is equal to 1.458, and M_2 is the Shah-Kobayashi [*11*] finite thickness correction factor.

Experimental crack opening studies were conducted to determine the accuracy of Eq 1. Results are shown in Fig. 8. The experimental procedure was to make plastic replicas of the plate surface in the cracked region at different load levels and to measure the crack opening on the replicas with a metallograph at X800 magnification. The replication procedure and plastic material were similar to those used for transmission electron microscopy.

The radiographic tests were conducted on 7.62-cm (3-in.) wide cross-welded plates of titanium, which were initially either 0.318 or 0.635 cm (0.125 or 0.250 in.) thick. Fatigue cracks were grown from shallow machine notches randomly located in either the weld bead or heat-affected zones. The plates were then machined flat on one side for a distance from the welds to remove the machine notches. The test procedure consisted of making radiograph exposures at different load levels and then having two inspectors read the radiographic film. The specimens were then sent to Rockwell for a repetition of the inspection.

Since the actual radiographic inspection of overwrapped vessels involved double-wall techniques for two thicknesses of liner and Kevlar overwrap, plus the pressurizing media, the equivalence of absorption was simulated by different thickness layers of metal plates and Kevlar taped to the specimens. The pressurizing gas was assumed to be helium because a more dense gas, such as nitrogen, increased the absorption to an unacceptable value.

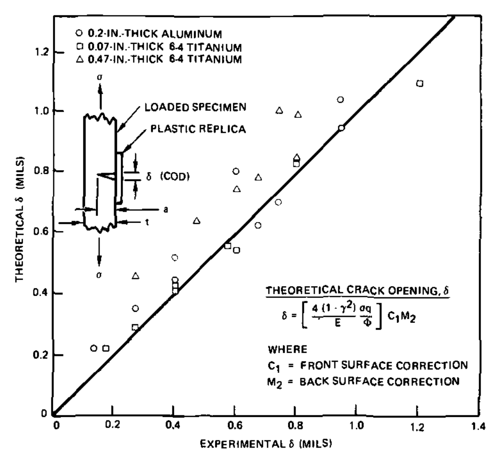

FIG. 8—*Comparison of surface crack opening theoretical results with experimental results.*

Figure 9 shows the radiographic inspection results for one set of specimens and the improvement of detectability with crack opening. Insufficient data were available to apply the 90/95 statistics, and a boundary curve was used where every data point above the curve was a detected point. Extrapolation of this line agrees with previous results for the detectability limit of a 70% deep flaw in an unstressed double-wall exposure. Results also show that a 40% deep flaw, which is the maximum initial size for a 400-mission safe-life of one vessel, can be detected with a crack opening displacement (COD) enhancement approach.

From these results, a number of the overwrapped pressure vessels were required to be radiographically inspected while pressurized with helium. None of the pressure vessels that passed the inspection required removal for additional inspections at less than the design life.

Cycles to Leak

Several test programs were conducted to determine experimentally the cycles to leak of metal liners in composite overwrapped pressure vessels. The purpose of the tests was to determine the applicability of conventional fatigue flaw-growth analysis for this type of problem. The most questionable analysis was on the portable oxygen system bottle, which had a 0.137-cm (0.054-in.) thick 6061-T6 aluminum liner. The cyclic stress range for the liner was from almost compressive yield stress at zero pressure to about one-half tension yield stress at maximum fill pressure. The safe-life requirement was 1200 repressurizations without leakage with an initial 60% through-the-thickness flaw.

Since the cycles to leak specimens were very thin to simulate the aluminum liner thickness, a special specimen configuration and stiffener arrangement was designed to prevent buckling. An assembly drawing of the specimen and stiffener plates is shown in Fig. 10. The plates were Teflon®-coated and greased to reduce

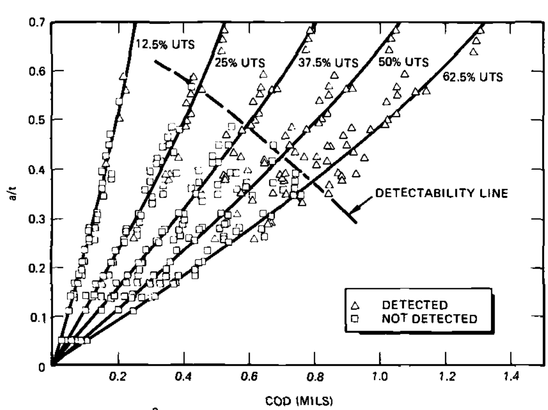

FIG. 9—*Radiographic NDE results for 0.216-cm (0.085-in.) thick welded titanium panels at different load levels.*

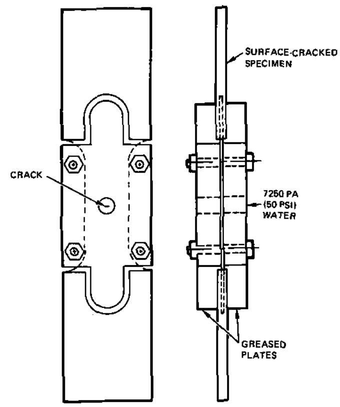

FIG. 10—*Specimen and stiffener plates for tensile compressive cycles to leak tests.*

friction loads on the specimen. The lack of friction was verified on an uncracked specimen that showed completely linear strain gage readings over the full cyclic load range. Not shown in the assembly drawing is the tapped hole and O-ring seal design in the back plate, which allowed pressurized water to flow through the crack when breakthrough occurred.

Results of the aluminum specimen tests are shown in Fig. 11 for two cyclic ranges. One range has compressive stress included, and the other range has it omitted. A linear least squares fit through the data shows that an order-of-magnitude decrease in cycles to leak occurs when the compressive portion of the stress cycle is included. Also shown in the figure is a comparison of test results with computer results calculated using the 6061-T6 aluminum crack-growth parameters in FLAGRO. The computer results are conservative except for the smallest flaw sizes with the tensile-tensile fatigue loading. The nonconservative computer results are caused primarily by the high ΔK_0 value for 6061-T6 aluminum used in FLAGRO. The computer results also show the important effect of

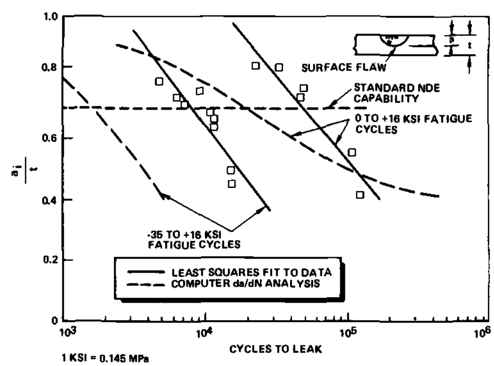

FIG. 11—*Cycles to leak results for 0.137-cm (0.054-in.) thick 6061-T6 aluminum specimens.*

the compressive part of the stress cycle and indicate the need to include all parts of the stress cycle even for R values equal to -2.

A second cycles-to-leak program was also conducted to investigate two different overwrapped pressure vessels with titanium liners. The concern for these pressure vessels was the accuracy of the cycles-to-leak analysis for flaws in the girth welds. Since the girth weld region of these liners did not have significant residual stresses after sizing, the tests were conducted with only tensile-tensile type fatigue loading. The cross-weld specimens used in the tests were machined from a qualification weld ring for each vessel. The weld beads were machined off the specimens to allow for more consistent and accurate stress cycling of the weld material.

The predicted fatigue stress spectra for each vessel consisted of several different stress ranges and R values, and were accounted for in the test verification. For each stress range, cycles-to-leak data were obtained for a wide range of flaw sizes by heat tinting at different flaw depths. The data points for each stress range were then fit with empirical equations by the least-squares technique. A linear damage-type analysis was then used to calculate the cycles to leak for the specific spectrum of each liner. These results were compared with FLAGRO results for typical fusion-butt-welded 6A1-4V titanium. The comparisons are shown in Table 2. Unlike the results for the thin aluminum liner, the thicker titanium liner results show good agreement between the empirical data and the FLAGRO computer results.

TABLE 2—*Calculated values of missions to leak for weld flaws in titanium liners of overwrapped tanks.*

	Analysis of Missions to Leak			
	OMS Helium Tank[a]		MPS Tank[b]	
a_i/t[c]	Linear Damage	da/dN	Linear Damage	da/dN
0.35	891	783	1818	1929
0.40	680	621	1463	1577
0.45	518	490	1177	1283
0.50	395	383	947	1048
0.55	301	300	767	845
0.60	230	225	613	670
0.65	175	170	493	525
0.70	133	120	397	398
0.75	102	81	319	289
0.80	77	50	257	198

[a]OMS is orbiter maneuvering system.
[b]MPS is main propulsion system.
[c]Assumed thicknesses are 0.424 cm (0.167 in.) for the OMS helium tank and 0.274 cm (0.108 in.) for the MPS tank.

Landing Gear Fracture Control

The initial flaw-growth analysis of the shuttle landing gears indicated that two parts had insufficient safe-life, the nose gear axle and the rod end of the main gear lower drag brace. Solution of these problems involved a material change for the axle, and a test program and revised analysis of the drag link rod end.

The nose gear axle showed insufficient theoretical safe-life because of the rolling axle design. The axle must sustain complete reversal high-cycle bending stresses ($R = -1$), and the parameter that limited the safe life was the material ΔK_0 threshold value. The problem was solved by changing the axle material from 300M steel to Inconel® 718, which has a much higher ΔK_0 value (15.0 versus 4.0).

The drag-link solution was more difficult. The problem was found to have been caused by approximate analyses, both for the load spectrum and the stress-intensity factor expression used for corner cracks at holes. The initial analysis indicated that a 0.005-cm (0.002-in.) corner crack at the hole edge would grow to failure during the first landing. A drawing of the main gear assembly and the critical crack location in the drag-link rod end is presented in Fig. 12.

A first check of the FLAGRO results for the drag-link analysis indicated that the stress-intensity factor expression used in the program did not approach zero as the flaw size approached zero. The proper limiting solution for a corner flaw much smaller than the hole radius should be approximately equal to a corner flaw in a plate with applied stresses equal to the hole boundary stresses. This discrep-

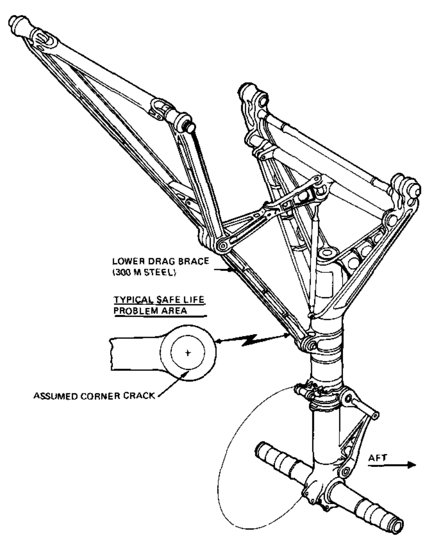

FIG. 12—*Main landing gear assembly showing location of the most critical safe-life analysis problem.*

ancy is shown in Fig. 13 by the difference in the FLAGRO curve compared with the curve for an edge crack in a plate. Also shown in the figure are failure test results for approximate quarter circular corner flaws in 0.55 subscale 300M steel specimens having the same hole-to-width ratio as the drag link. Both the limiting-case analysis and the test results show that the FLAGRO results are too conservative for very small flaws at the edge of large holes, particularly for predicting fracture stresses in practical structural applications.

In addition to the failure tests, both spectrum and uniform amplitude fatigue-crack-growth tests were conducted on similar drag-link subscale specimens. The uniform amplitude test results are shown in Fig. 14 for a special NDE initial flaw size. Comparisons are also shown for FLAGRO results in which both actual specimen material growth-rate parameters and the growth-rate parameters for shuttle analysis are used.

The spectrum fatigue test results are shown in Fig. 15 for the initially supplied spectrum and an updated spectrum where the maximum loads were decreased by 60%. The updated spectrum was based on later available data and anticipated usage that included landing impact, drag oscillation, landing drift, rollout, and braking loads. Since the 300M steel parts of the gear assemblies require shot-peening to produce compressive residual surface stresses, the spectrum fatigue load tests were conducted on both shot-peened specimens and specimens that were not shot-peened. As shown in Fig. 15, a significant improvement and sufficient safe life is obtained by shot-peening for small initial flaw sizes typical of those assumed for special NDE.

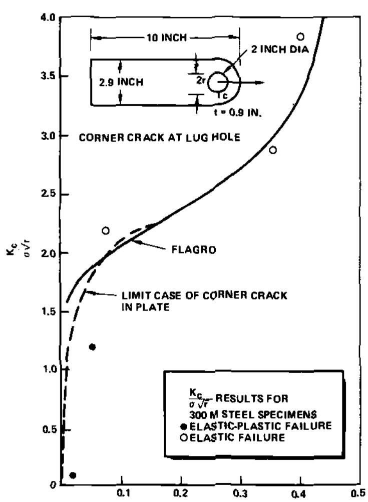

FIG. 13—*Comparison of corner crack from hole stress-intensity factor solutions.*

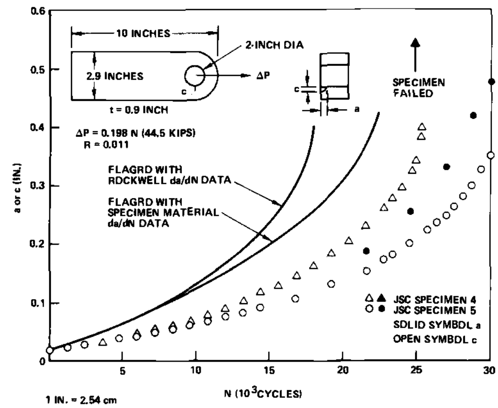

FIG. 14—*Constant amplitude fatigue test results for drag-link crack from hole specimens.*

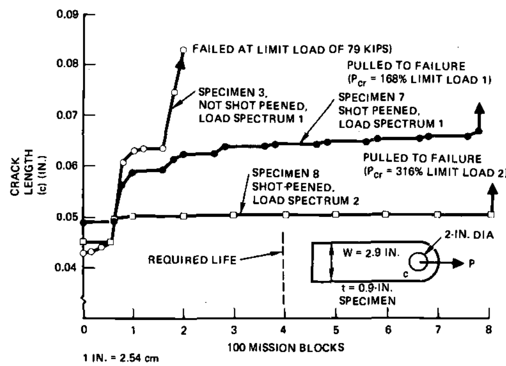

FIG. 15—*Spectrum load fatigue test results for drag-link crack from hole specimens.*

Elevated Temperature Tests of Superalloys

The most important fracture-control problems involving high-temperature crack-growth (excluding the shuttle main engines) were on the hydrazine-powered auxiliary power unit (APU), the cargo bay door hinges, and support fittings of the wing leading edge. All these problems involved fatigue loading of superalloy materials in different media and at temperatures exceeding 922 K (1200°F). The high-temperature media for the APU was decomposed hydrazine. The media for the hinges and leading-edge fittings was high-temperature air.

The initial concern for the APU was the possibility of sustained stress environmental crack-growth in the turbine wheel. The decomposition products of hydrazine are hydrogen, nitrogen, and ammonia, and no crack-growth data were available for any of these possible aggressive environments. Since the concern existed before selection of the turbine wheel material, a test program was first conducted to investigate several wheel materials. Tests at NASA were conducted on Astroloy®, Waspaloy®, Udimet® 700, and Inconel 718. An additional contracted study was sponsored on Astroloy and Rene'® 41, and these results were reported by Curbishley[*12*].

The decomposed hydrazine tests were conducted on surface flaw specimens in a 922 K (1200°F) ammonia environment. Ammonia was used because it was less hazardous and decomposes at elevated temperature into hydrogen and nitrogen. Only sustained load tests were conducted in the initial program to determine the possible existence of environmental incompatibility.

No incompatibility or sustained load crack growth occurred for any of the materials tested in ammonia at applied stress levels almost equal to the short-time creep strength levels. However, additional tests conducted at elevated temperature in air uncovered a severe environmental crack-growth problem for Inconel 718. None of the other materials showed incompatibility with the air environment at the 922 K (1200°F) test temperature.

The final design for the APU turbine wheel was a disk forged from Rene' 41 and with integrally machined blades. A ring was designed to contain fragments in case of wheel failure. A spin test of a preflawed wheel, however, showed that the containment ring would not prevent a catastrophic APU condition in case of a burst disk. Since the wheel blades were very small, the containment ring was assumed to be capable of containing a blade failure. Also, development testing of the APU showed that if fatigue cracks developed at the blade roots, the cracks would not propagate radially into the disk. These assumptions reduced the fracture-control problem to the analysis of only the turbine wheel disk, where the peak stress distribution was almost constant over most of the disk radius.

In order to obtain fatigue crack-growth data for the Rene' 41 turbine wheel material, compact tension specimens were machined from development test wheels as shown in Fig. 16. The tests were conducted in air because the test results mentioned previously indicated that decomposed hydrazine was not a more severe environment than high-temperature air. Results of the 866 K (1100°F) tests shown in Fig. 17 were used for the safe-life analysis because this temperature occurred in the highest stressed area. Analysis results showed that the wheel life was adequate with an ultrasonic special NDE initial flaw size.

The crack-growth data for the analysis of the leading-edge support fittings and cargo bay door hinges were also obtained from forging material used for the actual parts. The hinges were made from Inconel 718 and Inconel 706, and the support fittings were made from Inconel 718. Some of the leading edge support structure was also made from A286 steel, but testing of this material was conducted with rolled bar material.

Since the temperatures varied during reentry in the hinges and leading edge supports, the crack-growth data were obtained for different temperatures. Most tests were conducted on compact tension specimens with a thickness B of 1.27 cm (0.5 in.) and a depth W of 4.06 cm (1.6 in.). The results for the

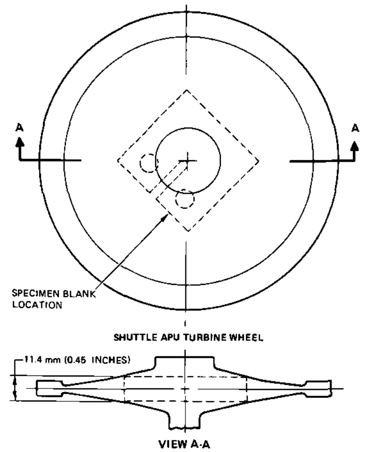

FIG. 16—*Location of specimen blank machined from turbine wheel.*

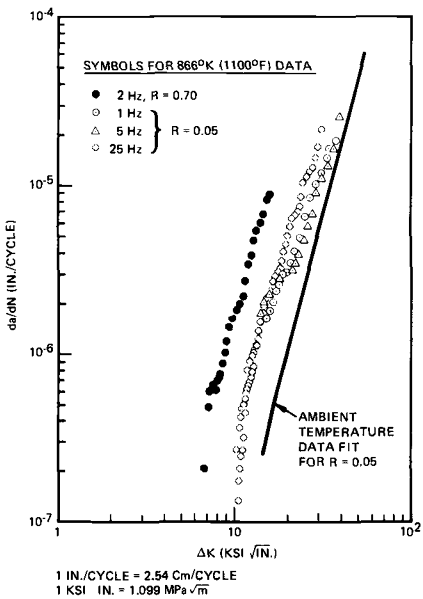

FIG. 17—*Crack growth of Rene' 41 turbine wheel material.*

Inconel 718, Inconel 706, and A286 sustained load tests are listed in Table 3. The elevated-temperature fatigue-crack-growth data and curve fit for Inconel 718 leading-edge fitting material are shown in Fig. 18.

The complexity of a typical crack-growth analysis problem, such as the leading-edge support structure, can be seen in Figs. 19 and 20. Figure 19 shows the structural design. Figure 20 shows the stress and temperature spectrums for

TABLE 3—K_{th} *results for superalloy materials.*

Material	Environment	Type Specimen[a]	Temperature °F[b]	K_{th}, ksi$\sqrt{\text{in.}}$[c]	K_c, ksi$\sqrt{\text{in.}}$[d]
Inconel 718	air	PTC	850	48	>53
Inconel 718	air	PTC	1000	14	>53
Inconel 718	air	PTC	1250	9	>41
Inconel 718	air	CT	1250	13	...
Inconel 718	air	CT	1450	13	...
Inconel 718	ammonia	PTC	1250	>19	>41
Inconel 706	air	CT	1200	16	132
A 286	air	CT	1000	55	112
Rene' 41	air	CT	1100	60	63

[a]Thickness of specimens were 0.30 cm (0.12 in.) for PTC and 1.27 cm (0.50 in.) for CT.
[b]$T_k = (5/9)(T_F + 459.67)$.
[c]1 ksi$\sqrt{\text{in.}}$ = 1.099 MPa$\sqrt{\text{m}}$.
[d]Failure occurred above yield strength for PTC specimens.

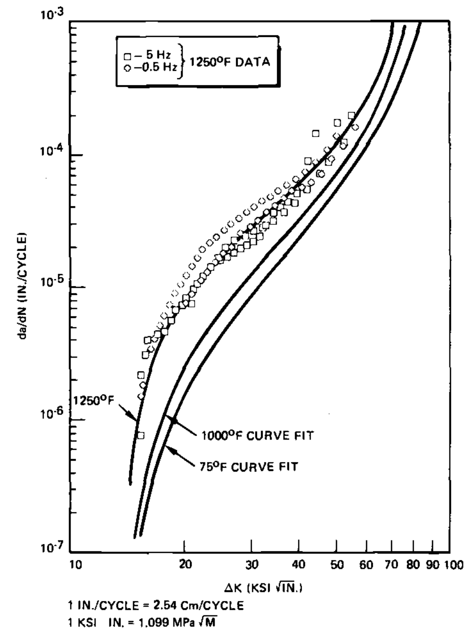

FIG. 18—*Crack-growth rate of Inconel 718 forgings for wing-leading edge support fittings.*

a single component of the structure. The varying crack-growth parameters in a fatigue spectrum are incorporated in FLAGRO, including the maximum stress-intensity factor cutoff value, which can be specified as K_{th}. Fortunately for the leading-edge fittings and payload bay door hinges, the maximum stresses did not occur at the same time as the maximum temperature, and none of these parts were found to have insufficient safe life or to exceed K_{th}.

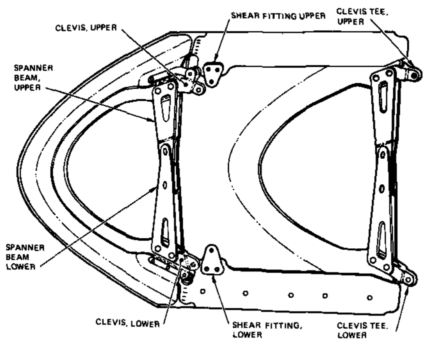

FIG. 19—*Geometry of wing-leading edge fittings.*

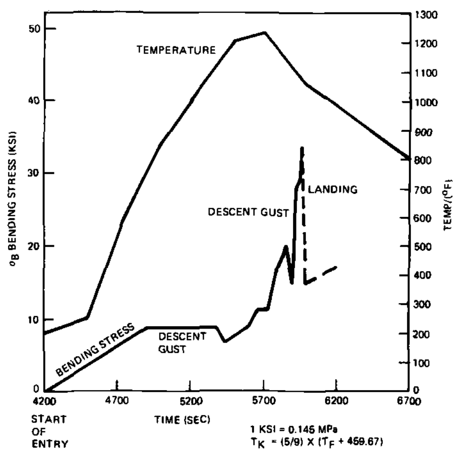

FIG. 20—*Stress and temperature profiles for wing-leading edge lower T-clevis.*

Finally, in regard to the overall test results of the superalloys in high-temperature air, only the Inconel 718, Inconel 706, and A286 steel showed a low value of K_{th}. The probable reason for this was that these three alloys are composed of large percentages of iron (for example, 18.5, 36.6, and 54.0%, respectively). The other superalloys all had less than 2% iron in their composition.

Proposed Development Tasks

The basic features of the FLAGRO [*13*] computer program have not been changed for approximately eight years. Even though numerous advancements have been made in fatigue crack-growth analysis during this period, there were advantages in having a consistent safe-life analysis during the shuttle development stage, particularly when the results were considered to be conservative. Now that actual flight loads and environmental data are available, an improved version of FLAGRO would be beneficial. Probably the greatest use of an improved computer program would be for fracture mechanics analysis on payloads for which the criteria are unchanged for fracture critical parts.

The first planned improvements in FLAGRO are the changing of several stress-intensity factor solutions and addition of numerous other needed solutions. The three-dimensional finite-element solutions of Newman and Raju [*14*], particularly for surface cracks, are being incorporated, and more will be added as they are obtained. The highest priority for accurate three-dimensional solutions, which should be included in the next version of FLAGRO, is the case of a cylinder loaded in tension and bending with a circumferential surface crack. Also, many crack-from-hole solutions will be added, both for corner cracks and through cracks. Numerous different through-crack-from-hole solutions have been obtained with the use of Green's function approach [*15*], and similar solutions are now being obtained for unequal-length cracks extending from a hole.

The second priority in improving FLAGRO is to incorporate a more accurate fatigue-crack-growth-rate model. As stated earlier, crack-growth data used in FLAGRO were obtained basically from compact tension specimens and fitted into the Collipriest growth equation. The lowest crack-growth rate value obtained for most materials was approximately 2.5×10^{-8} m/cycle (10^{-6} in./cycle), and some extrapolation was required to estimate the ΔK_0 threshold. The extrapolated values have been found to be as much as 50% higher in most cases compared to more recent data at several orders of magnitude slower growth rate. Also, in regard to crack-growth threshold, the use of the Collipriest equation with constant values assumed for C and n requires a constant value of ΔK_0. This also does not agree with published data, which show that ΔK_0 decreases with an increase in the stress ratio R.

A modified Forman equation (previously unpublished) shown in Fig. 21, gives a significant improvement for describing wide-range crack-growth rate behavior, especially in accounting for the unsymmetric shape of growth rate curves. Before the crack-growth rate model is changed, work must be conducted to more completely understand the variation of ΔK_0 with both the load ratio R and the overload ratio in spectrum-type fatigue loading. Computer techniques similar to those in Saxena et al [*16*] are being developed at the Johnson Space Center to automate the fatigue crack-growth testing and aid in developing a more accurate crack-growth rate model for spectrum loading.

Finally, with the use of computer-controlled fatigue machines, progress should be made in developing crack-growth rate models that directly incorporate random fatigue spectrums. Much test and flight data on the shuttle presently exist that could be used to study and further develop already published methods for analyzing random fatigue crack-growth for practical applications.

Acknowledgments

The task of fracture control on the space shuttle was a combined effort by many groups and individuals working for NASA, Rockwell International, and the many

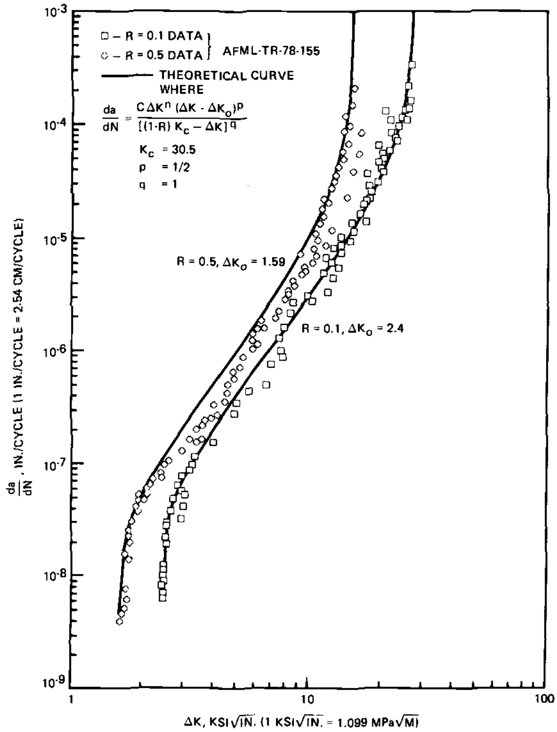

FIG. 21 — *Curve fit of modified Forman equation to crack-growth rate data for 2124-T851 aluminum.*

shuttle subcontractors. The many groups involved, both at NASA and contractor organizations, were in the areas of materials, quality control, testing, structural analysis, and manufacturing. The listing of all individuals who significantly contributed to the fracture-control program would be too extensive to attempt, but acknowledgment will be given to a few individuals of Rockwell who helped guide the fracture-mechanics applications on the program. At the Space Transportation and Systems Group, J. E. Collipriest led the projects in fracture mechanics testing, A. F. Liu guided the development of the FLAGRO computer program, and J. C. Joanides headed the application analysis team. At the Rocketdyne Division, W. T. Chandler conducted the crack-growth test efforts, and G. A. Vroman guided the safe-life computer analysis work. The authors would like to express appreciation to these individuals and to the many others not mentioned for their work who contributed to the writing of this paper.

APPENDIX A

TABLE A1 — *Table for material crack growth parameters to obtain* da/dN *in microinch per cycle.*

Material	N	C^a	$\Delta K_0{}^b$	$K_c{}^b$
		ALUMINUM		
2024-T851 plate, room temperature (RT)	4.211	0.000258	2.0	28.0[c]
2124-T851 plate, LT orientation, RT	3.44	0.0016	4.0	31.0[c]
2124-T851 plate, TL orientation, RT	4.0	0.000333	3.5	31.0[c]
2219-T87 plate, RT	3.3	0.00219	3.5	40.0[c]
2219-T62 plate, RT	2.79	0.008	3.5	35.0
7075-T73 extrusion, RT	2.67	0.01065	3.5	40.0
7075-T76 plate, RT	3.0	0.0063	3.0	30.0
6061-T6 plate, RT	2.64	0.0194	3.5	40.0
7075-T6 sheet, RT	2.528	0.0436	3.0	33.0
A356-T60 sand casting, 75 to 200°F, air, MMH, N_2O_4	3.14	0.0023	2.5	18.0
2024-T851 plate 300°F	4.211	0.000258	1.5	37.0[c]
2024-T851 plate, −150°F	7.38	2.16×10^{-8}	7.0	25.0[c]
2024-T861 plate, TL orientation, RT	3.36	0.00283	3.5	35.0[c]
2124-T851 plate, LT orientation, 350°F	3.126	0.00379	4.0	61.0[c]
2124-T851 plate, LT orientation, −150°F	4.354	4.11×10^{-5}	6.0	39.0[c]
2124-T851 plate, TL orientation, 350°F	3.62	0.00119	4.0	39.0[c]
2124-T851 plate, TL orientation, −150°F	4.915	6.88×10^{-6}	6.0	29.0[c]
C355-T61 cast, 300°F	3.14	0.0023	2.5	18.0
		TITANIUM		
3AL-2.5V tubing, annealed and relieved, RT	3.3	0.001	3.5	50.0
6AL-4V annealed, RT	3.184	0.000567	6.0	80.0[c]
6AL-4V STA, RT, air, N_2O_4, or MMH	3.3	0.00068	7.0	50.0[c]
5AL-2.5sn sheet, 75 to 300°F	2.47	0.00424	5.0	50.0
3AL-2.5V tubing, 75 to 150°F in MMH N_2O_4	3.3	0.001	3.5	50.0
5AL-2.5sn 125 to −425°F in argon or vacuum	3.13	0.000246	7.0	100.0
6AL-4V annealed, 75 to 150°F in MMH,	3.3	0.00068	6.0	45.0
6AL-4V annealed, 75 to 150°F in N_2O_4	3.3	0.00068	7.0	50.0
6AL-4V STA, 150°F in N_2H_4, MMH	3.3	0.00068	7.0	50.0
		STEEL AND CRS		
300 M, RT	2.184	0.004195	4.0	61.0[c]
4340 steel, RT	2.737	0.000745	6.0	90.0
9310 steel, RT	1.63	0.00836	3.5	200.0
9Ni-4CO-0.2C steel, RT	1.975	0.01207	5.0	150.0
PH 13-8 Mo stainless steel	1.98	0.0125	10.0	95.0
AISI 302, 304, 316, 321, 347, 348, RT	2.891	0.0004127	15.0	100.0
15-5 steel	1.98	0.01248	10.0	95.0
17-4 PH 75 to 150°F	1.9	0.00986	7.0	150.0
Maraging steel, 18-Ni, 250 grade, RT	2.107	0.00526	10.0	75.0
D6AC steel plate, RT	2.737	0.0007454	6.0	80.0
21-6-9 stainless steel tubing 75 to 150°F, air, MMH, N_2O_4	2.9	0.0005	10.0	100.0
304L stainless steel, 75 to 320°F in MMH	2.89	0.000413	10.0	100.0
AM 355 steel	1.98	0.0125	10.0	95.0
Ph 13-8 Mo, stainless steel, H 1000, RT	1.98	0.02	7.0	95.0

TABLE A1 *(Continued)*

Material	N	C^a	$\Delta K_0{}^b$	$K_c{}^b$
HEAT-RESISTANT ALLOY				
A-286 STA, LT orientation, RT	3.09	5.2×10^{-5}	15.0	100.0
A-286 STA, TL orientation, RT	3.97	2.67×10^{-6}	15.0	150.0
Inconel 718 STA, RT	2.7	0.0004	15.0	115.0
Inconel 718 STA, −200°F	3.74	5.05×10^{-6}	15.0	120.0
OTHER NONFERROUS				
Beryllium	3.086	0.000422	5.0	18.0
Columbium FS85/512E, silicide coated, 1400 to 2000°F	3.3	0.00068	5.0	50.0
Columbium C6-103, RT	1.97	0.016	12.0	80.0
Invar 35	2.7	0.0004	10.0	60.0
EF nickel plate, −100° to +320°F in air or 320° in MMH	2.9	0.0004	8.0	80.0
WELD JOINT				
2219 aluminum, FB weld, RT	3.75	0.00193	3.5	45.0
6061-T6 aluminum	3.75	0.002	3.0	40.0
3Al-2.5V titanium tube, 75° to 150°F, air MMH, N_2O_4	3.3	0.001	3.0	40.0
6Al-4V titanium annealed, GTA weld, 75 to 150°F, air, N_2O_4	2.95	0.00113	7.0	50.0
6Al-4V titanium annealed, GTA weld, 75 to 150°F, NMH	2.95	0.00113	6.0	45.0
6Al-4V Ti STA, 150°F in N_2O_4, MMH, N_2N_4	2.95	0.00113	7.0	50.0
21-6-9 stainless steel, GTA weld, 75 to 150°F, air, MMH, N_2O_4	2.9	0.0006	8.0	80.0
304L stainless steel, EB weld, 75 to 800°F in air, or, 75 to 320°F in MMH, N_2O_4	2.89	0.00082	8.0	80.0
EF nickel/304L interface, transverse to interface	2.9	0.0004	8.0	60.0
EF nickel/304L interface, parallel to interface	2.9	0.0004	8.0	80.0
Inconel 718 EB weld, STA, RT	3.46	0.000359	10.0	75.0
Inconel 718 EB weld, STA −200°F	3.52	0.000159	10.0	55.0
Inconel 718 FB weld, STA, RT	3.46	0.000163	10.0	120.0
Inconel 718 FB weld, STA, −200°F	3.52	7.25×10^{-5}	10.0	75.0
Columbium FU 85/512E, GTA weld, 1400 to 2000°F	1.97	0.016	12.0	80.0

[a]Unit in microinch/cycle/(ksi in.)^n where 1 in./cycle = 2.54 cm/cycle, 1 ksi in. = 1.099 MPA$\sqrt{m}$.
[b]Unit in ksi $\sqrt{in.}$
[c]K_c varies with specimen thickness as shown in Figs. A1 through A7.

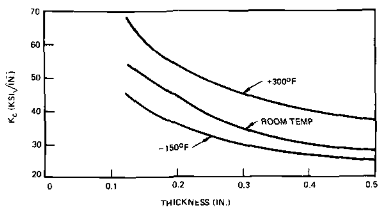

FIG. A1—*Variation of* K_c *with thickness for 2024-T851 aluminum plate.*

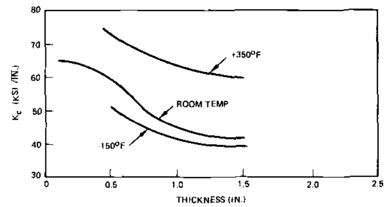

FIG. A2—*Variation of* K_c *with thickness for 2124-T851 aluminum plate, LT orientation.*

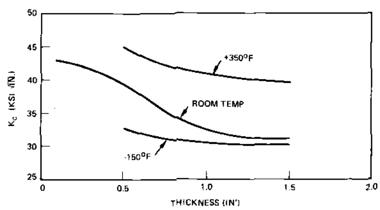

FIG. A3—*Variation of* K_c *with thickness for 2124-T851 aluminum plate, TL orientation.*

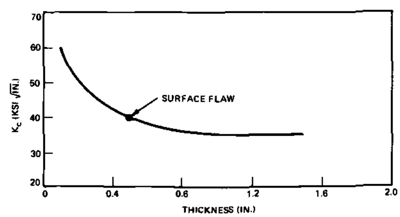

FIG. A4—*Variation of* K_c *with thickness for 2219-T87 aluminum plate, room temperature.*

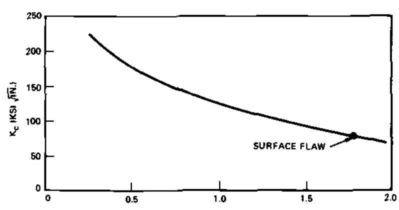

FIG. A5—*Variation of* K_c *with thickness for 6Al-4V titanium, annealed, room temperature.*

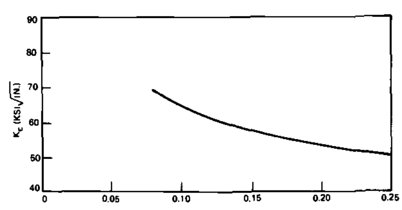

FIG. A6—*Variation of* K_c *with thickness for 6Al-4V-STA, room temperature.*

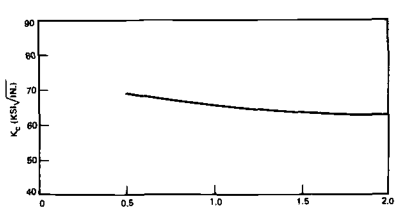

FIG. A7—*Variation of* K_c *with thickness for 300M steel, room temperature.*

References

[1] *Space Shuttle Orbiter Fracture Control Plan,* SD 73-SH-0082A, STS Group, Rockwell International, Downey, CA, Sept. 1974.

[2] Yee, B. G. W., Chang, F. H., Couchman, J. C., Lemon, G. H., and Packman, P. F., "Assessment of NDE Reliability Data," NASA CR-134991, General Dynamics Corp., Fort Worth, TX, Oct. 1976.

[3] Sugg, F. E., *Materials Evaluation,* Vol. 35, No. 8, Aug. 1977, pp. 39–54.

[4] Collipriest, J. E., in *The Surface Crack: Physical Problems and Computational Solutions,* J. L. Swedlow, Ed., American Society of Mechanical Engineers, New York, 1972, pp. 43–62.

[5] Forman, R. G., Kavanaugh, H. C., and Stuckey, B., "Computer Analysis of Two-Dimensional Fatigue Flaw-Growth Problems," NASA TM X-53036, NASA Manned Spacecraft Center, Houston, TX, Feb. 1972.

[6] Orange, T. W., Sullivan, T. L., and Calfo, F. D., "Fracture of Thin Sections Containing Through and Part-through Cracks," in *Fracture Toughness Testing at Cryogenic Temperatures, STP 496,* American Society for Testing and Materials, Philadelphia, 1970, pp. 61–81.

[7] Davies, K. B. and Fedderson, C. E. "Development and Application of a Fatigue-Crack-Propagation Model Based on the Inversion Hyperbolic Tangent Function," AIAA Paper No. 74-368, American Institute of Aeronautics and Astronautics, New York, 1974.

[8] Lake, W. W., Thorp, J., Barton, J. R., and Perry, W. D., in *Proceedings of the Symposium of Nondestructive Evaluation, 10th,* Southwest Research Institute, San Antonio, TX, 1975, pp. 131–173.

[9] Green, A. E. and Sneddon, *Proceedings,* Cambridge Philosophical Society, Vol. 46, Jan. 1950, pp. 159–163.

[10] Tada, H., Paris, P. C., and Irwin, G. R., *The Stress Analysis of Cracks Handbook,* Del Research Corporation, Hellerton, PA, 1973.

[11] Shah, R. C. and Kobayashi, A. S., in *The Surface Crack: Physical Problems and Computational Solutions,* J. L. Swedlow, Ed., American Society of Mechanical Engineers, New York, 1972, pp. 79–124.

[12] Curbishley, G. "Development of Fracture Mechanics Data for Two Hydrazine APU Turbine Wheel Materials," NASA CR 141696, Ai Research Manufacturing Co., Torrance, CA, Feb. 1975.

[13] Hu, T., *Advanced Crack Propagation Predictive Analysis Computer Program FLAGRO 4,* Rockwell International SOD 79-0280, Downey, CA, Sept. 1979; and NASA Tech Briefs MSC-18718, MSC-18721, Langley Research Center, Hampton, VA, Summer 1980.

[14] Newman, J. C. and Raju, I. S., "Stress-Intensity Factor Equations for Cracks in Three-Dimensional Finite Bodies," NASA Technical Memorandum 83200, Langley Research Center, Hampton, VA, Aug. 1981.

[15] Shivakumar, V. and Forman, R. G., *International Journal of Fracture,* Vol. 16, No. 14, Aug. 1980, pp. 305–316.

[16] Saxena, A., Hudak, S. J. Jr., Donald, J. K., and Schmidt, D. W., *Journal of Testing and Evaluation,* "Computer-Controlled Decreasing Stress Intensity Technique for Low Rate Fatigue Crack Growth Testing," Vol. 6, No. 3, May 1978, pp. 167–174.

James L. Rudd [1]

Air Force Damage Tolerance Design Philosophy

REFERENCE: Rudd, J. L., "**Air Force Damage Tolerance Design Philosophy,**" *Damage Tolerance of Metallic Structures: Analysis Methods and Applications, ASTM STP 842*, J. B. Chang and J. L. Rudd, Eds., American Society for Testing and Materials, 1984, pp. 134–141.

ABSTRACT: This paper summarizes the U.S. Air Force damage tolerance design requirements for metallic airframes. The requirements are a function of the design concept and degree of inspectability of the airframe. Both analytical and experimental requirements are presented. The requirements include the initial damage size, shape, and location, which must be assumed in design. Also presented are the subsequent crack growth and residual strength requirements, which must be satisfied because of the presence of this initial damage.

KEY WORDS: fatigue (materials), Air Force research, crack propagation, damage tolerance, fracture mechanics, fatigue crack growth, residual strength, design requirements, initial damage, aircraft structure

A number of U.S. Air Force aircraft structural failures occurred in the late 1960s and early 1970s. These failures occurred during testing as well as in service. The failures were often caused by imperfections, flaws, defects, or discrepancies, which were either inherent in the material or introduced during manufacturing and assembly of the structure. Recognizing the causes of these failures and the importance of eliminating them, the Air Force adopted a new design philosophy. The new design philosophy includes the assumption of the existence of such flaws during the initial design of the structure. It is required that the structure be designed to be tolerant of such damage with regards to safety.

This paper summarizes the Air Force damage tolerance design requirements for metallic airframes [*1–3*]. Both analytical and experimental requirements are presented. The requirements are a function of the design concept and degree of inspectability of the structure. Details of the initial damage that must be assumed in design are presented. Also presented are the subsequent crack growth and

[1]Aerospace engineer, Air Force Wright Aeronautical Laboratories, Wright-Patterson Air Force Base, OH 45433.

residual strength requirements that must be satisfied because of the presence of this initial damage.

The Air Force philosophy requires that safety of flight structure must be designed under one of two design concepts: (1) slow crack growth or (2) fail-safe. Slow crack-growth structure is designed such that assumed initial damage will not reach a critical size within a specified period of time. Fail-safe structure can be classified as either multiple-load-path or crack-arrest structure. Multiple-load-path structure consists of multiple elements. It is designed such that when one of these elements fails, the remaining structure will not fail within a specified period of time. The intact and remaining structure are defined as that structure before and subsequent to load-path failure, respectively. Crack-arrest structure is designed such that when unstable rapid crack propagation is stopped within a continuous area of the structure before complete failure, the remaining structure will not fail within a specified period of time. The intact and remaining structure are defined as that structure before and subsequent to unstable growth and arrest, respectively.

There are different degrees of inspectability for each of these two design concepts. Slow crack-growth structure can be classified as either (1) noninspectable or (2) depot or base level inspectable. The intact structure for the fail-safe design concept also can be classified as either (1) noninspectable or (2) depot or base level inspectable. The degrees of inspectability of the remaining structure for the fail-safe design concept are (1) depot or base level, (2) special visual, (3) walk-around visual, (4) ground evident, and (5) in-flight evident.

Damage cannot readily be detected for noninspectable structure. For depot or base level inspectable structure, damage can be detected using standard non-destructive inspection (NDI) techniques (for example, penetrant, X-ray, ultrasonics, and so forth). Special visual inspections involve the use of simple visual aids such as mirrors and magnifying glasses. Walk-around visual inspections are performed by personnel at the ground level without the use of special inspection aids. Ground evident inspectable structure is structure in which damage will be obvious to ground personnel without specifically inspecting the structure. Structure is in-flight evident inspectable if damage that occurs in flight results in characteristics that make the flight crew aware that the damage has occurred.

Analytical Requirements

The Air Force analytical damage tolerance design requirements [2] include the assumption of the existence of initial primary damage in each structural element of safety of flight aircraft structure. This initial primary damage is assumed at the most unfavorable locations and orientations with respect to applied stress and material properties. The size of the assumed initial primary damage is a function of the design concept and degree of inspectability of the structure. In addition to the existence of initial primary damage at the most critical locations, initial continuing damage of a specified size is assumed to exist at certain adjacent locations. The airframe must be designed to meet certain crack growth and residual strength requirements with this initial damage present such that catastrophic failure of the aircraft does not occur within specified time intervals. These design requirements are presented for each design concept in the following paragraphs.

Slow Crack-Growth Structure

For noninspectable as well as depot or base level inspectable structure in which the component and fasteners are removed from the aircraft for inspection, the initial primary damage sizes and shapes assumed in design are presented in Fig. 1. For depot or base level inspectable structure in which the component and fasteners are not removed from the aircraft for inspection, larger initial primary damage sizes are assumed as illustrated in Fig. 2. For fastener hole locations, the crack lengths in Fig. 1 are measured from the bore of the hole while those in Fig. 2 are measured from the fastener head or nut.

Smaller initial primary damage sizes than those specified in Figs. 1 and 2 may be assumed if a successful NDI demonstration program is conducted. The NDI program must demonstrate that the smaller initial primary damage size assumed can be detected with a 90% probability of detection and a 95% confidence level. Smaller initial primary damage sizes may also be assumed if proof tests are conducted in which the calculated critical crack size at the proof test stress level is smaller than those specified in Figs. 1 and 2.

The initial primary damage sizes just discussed are based upon NDI capability. Initial continuing damage must also be assumed at other less critical locations

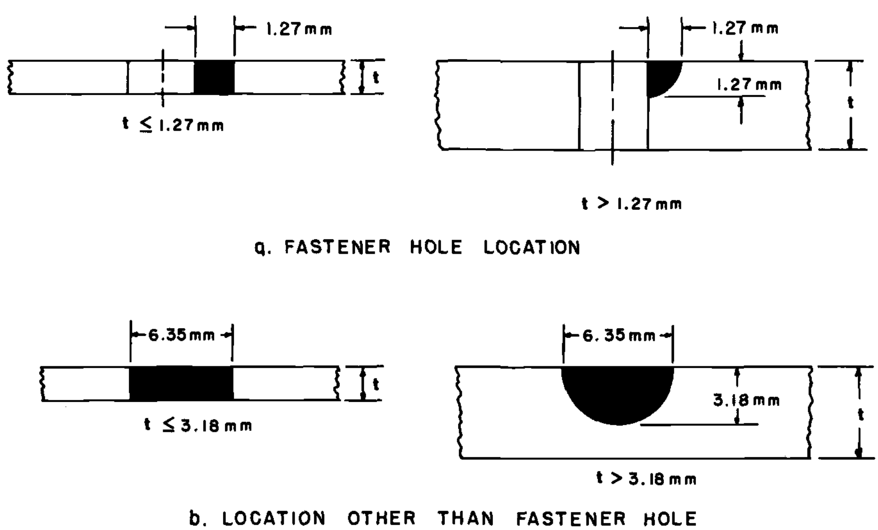

FIG. 1—*Initial primary damage for noninspectable and depot or base level inspectable structure with component removal (slow-crack-growth structure).*

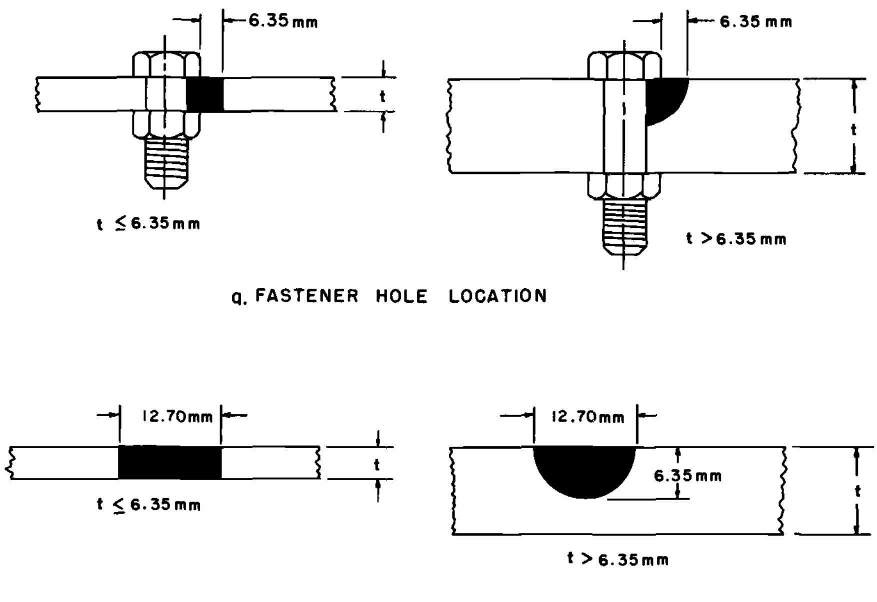

FIG. 2—*Initial primary damage for depot or base level inspectable structure without component removal.*

which represent the overall fatigue quality of the structure. The initial continuing damage sizes and shapes assumed are presented in Fig. 3. If initial quality data (for example, fractographic studies for determining equivalent initial flaw sizes) have been developed, these data may be used for justifying sizes other than those specified in Fig. 3.

In order to prevent catastrophic failure of the aircraft, the appropriate initial damage presented in Figs. 1 through 3 must not reach a critical size during a specified time interval. Hence, certain crack growth and residual strength requirements must be met. These requirements are presented in Table 1. The initial damage specified in Figs. 1 through 3 is a function of the degree of inspectability

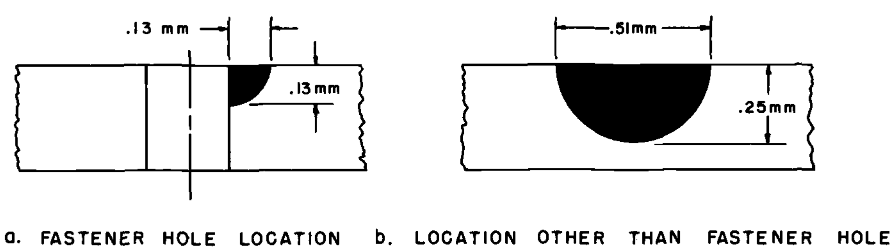

FIG. 3—*Initial continuing damage.*

of the structure. This damage must not reach a critical size during the safe crack growth interval specified in Table 1. Also during this interval, the aircraft must be able to sustain the specified minimum required residual strength (that is, minimum required internal member load) P_{xx} with the damage present. The residual strength P_{xx} must be equal to or greater than the design limit load. However, P_{xx} need not be greater than 1.2 times the maximum load expected in one lifetime.

For example, the initial primary and continuing damage for noninspectable structure is presented in Figs. 1 and 3, respectively. This damage must not reach a critical size within two design service lifetimes (Table 1). During this time, the aircraft must be able to sustain the maximum load expected in 20 lifetimes, providing this load is equal to or greater than the design limit load and less than 1.2 times the maximum load expected in one lifetime.

Fail-Safe Structure

Fail-safe structure can be classified as either multiple-load-path or crack-arrest structure. The Air Force damage tolerance design requirements are very similar for each of these structural classifications. Two sets of crack growth and residual strength requirements exist for each classification. The first set applies to intact structure while the second set applies to the remaining structure.

The initial primary damage sizes and shapes for intact fail-safe structure are presented in Fig. 4. The types of structure for which these damage assumptions are valid include depot or base level inspectable structure in which the component and fasteners are removed before inspection. For depot or base level inspectable structure in which the component and fasteners are not removed before inspection, the initial primary damage sizes and shapes are those presented in Fig. 2. The initial continuing damage assumptions for intact structure are those specified in Fig. 3.

The crack growth and residual strength requirements for the intact structure are presented in Table 2. The residual strength for the intact structure must be equal to or greater than the design limit load but need not be greater than 1.2 times the maximum load expected in one lifetime.

In addition to the residual strength requirement P_{xx} of the intact structure before load path failure or crack arrest, there is a requirement to sustain a minimum load P_{yy} at the instant of load-path failure or crack arrest. The residual strength P_{yy} must be equal to the design limit load or 1.15 times P_{xx}, whichever is greater. The factor 1.15 is a dynamic factor.

TABLE 1—*Crack growth and residual strength requirements for slow crack-growth structure.*

Inspectability	Safe Crack Growth Interval, lifetimes	Residual Strength P_{xx}
Depot or base level	½	maximum load in 5 lifetimes
Noninspectable	2	maximum load in 20 lifetimes

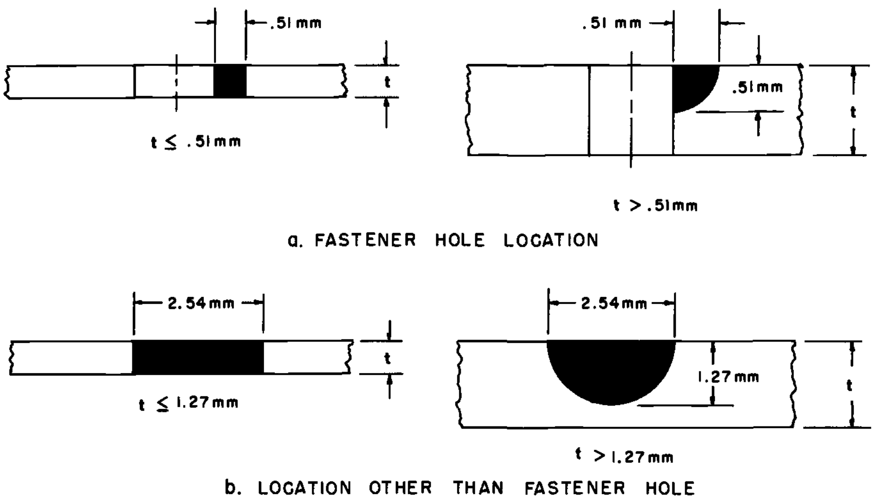

FIG. 4—*Initial primary damage for intact structure that is either noninspectable or depot or base level inspectable with component removal (fail-safe structure).*

TABLE 2—*Crack growth and residual strength requirements for intact structure (fail-safe design concept).*

Inspectability	Safe Crack Growth Interval, lifetimes	Residual Strength P_{xx}
Depot or base level	¼	maximum load in 5 lifetimes
Noninspectable	1	maximum load in 20 lifetimes

Following load-path failure or crack arrest, crack-growth and residual strength requirements must also be met for the remaining structure. These requirements are presented in Table 3. Let us now discuss the damage used in the crack growth and residual strength predictions for the remaining structure.

For multiple-load-path structure, the initial damage used in the crack growth and residual strength predictions for the remaining structure is the failed load path plus the damage assumed in the adjacent load-path structure. For dependent structure, the damage assumed in the adjacent load-path structure is that shown in Fig. 4 plus the amount of growth that occurs before load-path failure. For independent structure, the damage assumed in the adjacent load-path structure is that shown in Fig. 3 plus the amount of growth that occurs before load-path failure. Dependent structure is structure in which a common source of cracking exists in adjacent load paths at one location caused by the nature of the assembly or manufacturing procedures (for example, members spliced together using common drilling and assembly operations). Independent structure is structure in which it is unlikely that a common source of cracking exists in adjacent load paths at one location because of the nature of the assembly or manufacturing procedures.

TABLE 3—*Crack growth and residual strength requirements for remaining structure (fail-safe design concept).*

Inspectability	Safe Crack Growth Interval	Residual Strength P_{xx}
In-flight evident	return to base	maximum load in 100 flights
Ground evident	one flight	maximum load in 100 flights
Walk-around visual	50 flights	maximum load in 1000 flights
Special visual	2 years	maximum load in 50 years
Depot or base level	½ lifetime	maximum load in 5 lifetimes

For crack-arrest structure, the initial damage used in the crack growth and residual strength predictions for the remaining structure is the primary damage following arrest plus the damage assumed in the structure adjacent to the primary damage. For conventional skin-stringer structure, the primary damage following arrest is assumed to be two panels of cracked skin plus the broken central stringer. If tear straps are provided between stringers, the primary damage is assumed to be the cracked skin between tear straps plus the broken central stringer. The damage assumed to exist in the structure adjacent to the primary damage is that shown in Fig. 3 plus the amount of growth that occurs before crack arrest.

Let us consider an example of fail-safe multiple-load-path dependent structure. Assume that both the intact and remaining structure is depot or base level inspectable in which the component and fasteners are removed for inspection. The continuing damage and initial primary assumptions used in the design of the intact structure are presented in Figs. 3 and 4, respectively. This initial damage must not result in failure of the intact structure within one fourth of the design service life (Table 2). During this time, the intact structure must be able to sustain the maximum load expected in five lifetimes, providing this load is equal to or greater than the design limit load and less than 1.2 times the maximum load expected in one lifetime. At the instant of load-path failure, the aircraft must be able to sustain a minimum load of 1.15 times the maximum load expected in five lifetimes. This residual strength at the instant of load-path failure must have a minimum value of 1.15 times the design limit load but need not exceed 1.38 times the maximum load expected in one lifetime. The initial damage assumed in the remaining structure is the failed load path plus the damage assumed in the adjacent load path structure (Fig. 4) in addition to the amount of growth that occurs before load-path failure. This initial damage must not result in failure of the remaining structure within one half of the design service life (Table 3). During this time, the remaining structure must be able to sustain the maximum load expected in five lifetimes, providing this load equals or exceeds the design limit load but is less than 1.2 times the maximum load expected in one lifetime.

Experimental Requirements

In addition to the analytical requirements [2] previously discussed, experimental requirements [3] also exist to ensure that Air Force aircraft are designed to be damage tolerant. First, design development tests are required to provide an early evaluation of the damage tolerance of the structure as well as the accuracy of the crack growth and residual strength analysis used in design. A wide range of geometric and loading complexities may be selected for these tests. The types of specimens selected may vary from simple coupons and elements to complex splices, joints, fittings, wing-carry-through structures, and so forth.

Additional damage tolerance tests must be conducted as needed. These tests must be consistent with the analytical requirements [2] previously discussed. Hence, the type, number, and duration of these tests are a function of the design concept and degree of inspectability of the structure. These tests will furnish data not available from the design development tests. Existing hardware will be used for these tests when possible. These existing hardware may range from components and assemblies from the design development tests to full-scale static and durability test articles. Additional test specimens, ranging in size and complexity, will be fabricated and tested as needed.

Inspections are required during the damage tolerance testing. The type of inspections performed is a function of the degree of inspectability of the structure. A destructive tear-down inspection is also required after completion of the damage tolerance testing, which includes disassembly and laboratory-type inspection of the fracture critical areas. Fractographic examinations will be performed to obtain crack growth and initial quality data. Optional inspection proof tests may be performed on components, assemblies, or complete airframes. These optional tests must be approved by the Air Force. The purpose of these tests is to establish initial flaw sizes other than those specified in the Air Force damage tolerance design requirements [2] when the use of conventional NDI is impractical or cost ineffective.

Conclusions

In order to protect aircraft from catastrophic failure, the U.S. Air Force has adopted a damage tolerance design philosophy. This philosophy accounts for the fact that flaws exist in aircraft structure because of various material and structural manufacturing and processing operations. The aircraft is designed to meet certain crack growth and residual strength requirements with these flaws present. The crack growth and residual strength requirements are a function of the design concept and degree of inspectability of the aircraft. The damage tolerance of the structure and the accuracy of the analysis methods used are experimentally verified.

References

[1] "Aircraft Structural Integrity Program, Airplane Requirements," MIL-STD-1530A, Air Force Aeronautical Systems Division, Wright-Patterson Air Force Base, OH, Dec. 1975.

[2] "Airplane Damage Tolerance Requirements," MIL-A-83444, Air Force Aeronautical Systems Division, Wright-Patterson Air Force Base, OH, July 1974.

[3] Anon., "Airplane Strength and Rigidity, Ground Tests," MIL-A-8867B, Air Force Aeronautical Systems Division, Wright-Patterson Air Force Base, OH, Aug. 1975.

Summary

The papers collected in this symposium volume present in detail the state-of-the-art damage tolerance methodologies and their applications to the primary structures made of conventional metallic materials.

An overview of basic concepts of damage tolerance analysis methodology was provided in the paper by Grandt. In this paper, the linear elastic fracture mechanics (LEFM) approach which employs the stress intensity factor, K, as the parameter to characterize the growth and fracture behavior of a crack contained in a structure was described. Procedures for using K to determine the fatigue crack growth life and the residual strength of an initially cracked structure were outlined. Limitations of LEFM were also discussed in Grandt's paper in order to define problems which can be confidently analyzed by the LEFM method and to identify areas which require more sophisticated approaches.

The paper by Engle examined the commonly used techniques for performing damage accumulations in a crack growth analysis. These techniques range from the simple closed form solution to sophisticated numerical integration methods. Equivalent damage techniques based on statistical representations of complicated random spectra were also included in the paper. Engle also presented recommendations for applications to various types of service loading spectra. From which, the reader will have a general feeling as to what technique ought to be selected in order to perform a reliable, cost-effective damage tolerance analysis.

Various load interactions take place in variable amplitude loadings. Most of the service load histories for aircraft and spacecraft structures are variable amplitude in nature. In predicting cyclic growth behavior of cracks or crack-like flaws contained in such structures, one must then consider the effects of the load interactions. Retardation and acceleration are the two major load interactions which affect the crack growth rates. Numerous models have been proposed in the last fifteen years or so to account for retardation and acceleration effects. Saff's paper reviewed some of the models in great detail. Capabilities and limitations of various models were also discussed in his paper.

Chang summarized the results of five sets of round-robin fatigue crack-life predictions conducted by ASTM Task Group E24.06.01 on Application of Fracture Data to Life Predictions. Important conclusions drawn by Chang were as follows: (1) The fatigue crack lives of part-though-crack specimens under constant amplitude loadings can be predicted with sufficient accuracies using the constant amplitude load *da/dN* data obtained from compact-tension specimens;

(2) reasonable accurate predictions can be achieved for center-crack-tension specimens subjected to random spectrum loadings using constant amplitude da/dN data and the state-of-the-art crack growth retardation/acceleration models; (3) for variable amplitude loadings containing single or multiple overload/underload cycles, most of the state-of-the-art growth models are not able to provide accurate predictions.

Stiffened structures are very common structural configurations applied to aircraft structural designs. The need to have a reliable approach for the damage tolerance analysis of cracked stiffened structures is obvious. The paper by Swift presented an analytical method that provides a reliable yet economical means for the determination of crack-tip stress intensity factors and stiffener stress concentration factors for cracked stiffened structures. These data can be used in parametric crack growth and residual strength studies during the initial design phase of an aircraft. A sample parametric study was included in his paper to illustrate the method.

With the increasing activities in the space industry, the paper by Forman and Hu on the application of fracture mechanics on space shuttle is very beneficial. Space shuttle was the first space project to require a comprehensive fracture control program. This paper provided five topics in the discussion of the application of fracture mechanics in the fracture control of the shuttle. They were (1) selection of fracture critical parts, (2) flaw detection capabilities, (3) flaw growth analysis, (4) special test programs, and (5) proposed development tasks. The fatigue crack growth rate equation (Collipriest equation) parameters used for performing safe-life analyses on various shuttle structures were also included in this paper. These parameters were programmed into a computer code, FLAGRO 4, for easy input. These fitted parameters are, however, not recommended to be used on other space programs without further verification.

The paper by Rudd presented a comprehensive summary of Military Specification, Airplane Damage Tolerance Requirements (Mil-A-83444). The U.S. Air Force adopted the damage tolerance design approach to replace the conventional fatigue design approach since the mid 1970s. Yet, this is one of a few papers describing in great detail the requirements stated in that military specification. The requirements include the initial damage size, shapes, locations, and so forth that must be assumed in the initial design, as well as the crack growth and residual strength limits that must be met by the aircraft structure with initial damage present. Rudd's paper provided a clear picture as to what extent the aircraft should be designed in order to ensure its damage tolerance capability.

It is hoped that information provided in this publication will be useful to designers, analysts, and other technologists who are directly or indirectly involved in damage tolerance design and analysis. There is no doubt that further analytical efforts are needed to advance the damage tolerance analysis methodology. This is particularly true for analyzing adhesive bonded structures or laminated composite structures. Joint efforts among membership in ASTM Committee E-9 on Fatigue, E-24 on Fracture Testing, and D-30 on High Modular Fibers and Their Composites is urged to achieve this goal.

James B. Chang
The Aerospace Corporation,
Los Angeles, CA 90009,
coeditor

James L. Rudd
Air Force Wright Aeronautical Laboratories,
Wright-Patterson Air Force Base, OH 45433,
coeditor

Index